May 2016

Integrated Rapid Prototyping: Efficient Development of Custom Orthotics

Eric Scott Zandrow
Worcester Polytechnic Institute

Francois-Xavier Alain Stricker-Krongrad
Worcester Polytechnic Institute

James Patrick Nolan
Worcester Polytechnic Institute

Nicholas Armand Picard
Worcester Polytechnic Institute

Project Number: CF – RP16

INTEGRATED RAPID PROTOTYPING:

EFFICIENT DEVELOPMENT OF CUSTOM ORTHOTIC DEVICES

A Major Qualifying Project Report

Submitted to the Faculty

of the

WORCESTER POLYTECHNIC INSTITUTE

In partial fulfillment of the requirements for the

Degree of Bachelor of Science in Mechanical Engineering

By

James Nolan

Nick Picard

Nicholas Picard

Francois-Xavier Stricker-Krongrad

Eric Zandrow

Eric Zandrow

Date: 28 April, 2016

Keywords:

1. Rapid Prototyping
2. Custom Orthotics
3. Process Validation

Professor Cosme Furlong

Abstract

Companies strive to quickly create customized products, meeting the desires and needs of a consumer. Integrated Rapid Prototyping (IRP) is a systematic approach of optimizing the product development cycle from conception to realization, a process which we defined by the combination of Full Field 3D digitization, Computer Aided Design, Finite Element Analysis, additive manufacturing, and non-destructive testing. IRP has applications in numerous fields, from consumer accessibility to industry level manufacturing. As a case study, IRP was applied to the medical field through the creation of a custom orthotic device. A process done by using leg scans taken by a portable scanner, designing an orthotic model based on the scans, detailed construction and analysis of the CAD model, fabrication through additive manufacturing, and product testing via Digital Image Correlation. Through this application, the team analyzed the development process by considering material characteristics, surface metrology, full field optical techniques, and subprocesses validation.

Acknowledgements

We would like to thank Orthocare Innovations, specifically Lucas Lincoln and Aizen Ulric for assisting and supporting us with the technological and financial resources required to complete this project.

The team would also like to extend our gratitude to all of the graduate students from the Center for Holographic Studies and Laser mirco-mechaTronics (CHSLT) at Worcester Polytechnic Institute, specifically Koohyar Pooladvand and Payam Razavi.

Most of all, we would like to thank Professor Cosme Furlong for advising this project and providing us with guidance and expertise throughout the entirety of this project and for providing access to the facilities of the CHSLT. The use of the high-speed National Science Foundation – MRI supported Digital Image Correlation System is also appreciated.

Lastly, we would like to thank the Mechanical Engineering Department of Worcester Polytechnic Institute for making this project a possibility and giving us the privilege to take part of a challenging experience.

Authorship Page

All authors contributed equally to all aspects of this work.

Table of Contents

Table of Figures

List of Tables

Executive Summary

Integrated Rapid Prototyping (IRP) is a systematic approach of optimizing the product development cycle of custom parts from conception to realization, a process which we defined by the combination of Full Field 3D digitization, Computer Aided Design (CAD), Finite Element Methods (FEM), additive manufacturing, and non-destructive testing. In order to properly examine the process, it was applied to the creation of a custom Ankle Foot Orthotic (AFO), a supportive foot brace that helps correct abnormal gait caused by drop foot, or the slapping or dragging of the foot. In order to properly implement the IRP process, each individual subprocess was researched, validated, and analyzed to determine the overall effectiveness.

The application for custom AFO creation implements each of the previously defined steps. The first steps involved converting the patient's leg into the modeling program to use as a base. This is done by scanning the leg, importing the data into a CAD program, and converting the obtained data into a solid. Following this, the outline of the AFO is created, and used to extrude the surfaces of the leg model, thus creating a form fitting AFO. Non-destructive testing was conducted to test the device's performance compared to that of a standard AFO. This was done by first testing a standard AFO that was purchased off the shelf for deformations and buckling. Once the results from FEM for the custom AFO standard AFO matched, the model was considered acceptable and manufactured in a polypropylene like material.

Each subprocess was individually validated for accuracy. In order to validate the scanning device, both a NIST traceable gauge and a simplified AFO model were scanned

and compared to models with exact dimensions. Using these data, a confidence interval was generated to determine a possible error range. Part of the modeling process, the conversion of point cloud data to solid model via ScanTo3D, was validated by comparing an original point cloud to a solid model created by ScanTo3D. A confidence interval was again constructed to find the range that this error should fall in. For validation of the boundary conditions, the simplified AFO was used as the foundation of an analytical model. This analytical model was compared to an FEM model in which the boundary conditions and loads were similar. As a final comparison, the FEM results were compared to the results gathered from non-destructive testing done through digital image correlation.

In terms of errors, the scanning device used for this project produce an error between ± 1306 μm and ± 1262 μm, and the ScanTo3D produce an error between ± 109 μm to ± 37 μm. The analytical model the FEM had an error within 2.5%, and the DIC and FEM results had an error up to 20%.

The process used here resulted in a patient specific AFO that performed as expected. Recommendations for future work were made reflecting the results obtained from the process. For this application, surface and topology optimization are major aspects needing to be addressed. Process automation would be vital in terms of time reduction and public accessibility. This process is not only restricted to this application but capable of being used in other areas such as replication of designs for reverse engineering, remote inspection, historical preservation, medical imaging, and customization.

1.0 Introduction

With the development of Stereolithography for additive manufacturing, rapid prototyping became prominent for the efficient development of components in industry. Regarded as the first commercial rapid prototyping technology, additive manufacturing has risen to be one of the most promising innovations on the market as a design-driven manufacturing process with its capabilities to generate custom material definitions based on complex geometries [1]. The use of additive manufacturing for rapid prototyping has given companies the ability to quickly create prototype models for testing before the final commercialization of the product. However, rapid prototyping as we know it only covers certain aspects of a process which has the potential to redefine the custom manufacturing industry.

Rapid prototyping currently takes three-dimensional data from computer aided drafting (CAD) software to promptly fabricate a physical model of a desired part. Rapid prototyping processes often do not use automated data acquisition techniques such as 3D digitization. With the popular emergence of low cost portable 3D scanners, companies are now able to accomplish data acquisition prior to modeling manipulation thus implementing a new step in the rapid prototyping process. The extensions and applications of integrated rapid prototyping can highlight its use on the market with benefits ranging from medical applications to defense capabilities, thus rendering the possibilities of this process to be considered limitless in terms of customization.

As the demand for on-site specific production increases, more companies are turning to new ideas to solve critical problems during their product development.

Mastering the art of rapidly prototyping parts is vital for any corporation in the race to launch new products especially in terms of reverse engineering [2]. While used in isolation, rapid prototyping provides moderate amounts of reductions in time, labor, and materials in the product development process. Essentially, an integrated approach for rapid prototyping is desired to achieve an effective method that will enhance the efficient use of pre-existing additive manufacturing technologies. The approach, defined as Integrated Rapid Prototyping (IRP), involves the combination of 3D digitization (digital shape acquisition), computer-aided design (CAD), computational and analytical modeling, additive manufacturing, and non-destructive testing of fabricated components to functional prototypes. The goal of this project was to develop a process from conception to realization to effectively develop a product and demonstrate its application through custom orthotic devices.

An effective IRP process means functional prototypes with better time efficiency in the product development cycle. Understanding where areas within the rapid prototyping process can be improved requires an understanding of the technological specifics involved in each part of the process on a mathematical basis. For our IRP process, this involved an in-depth validation and analysis into each associated sub process, to verify accuracy and precision, and the possible implementation towards public accessibility. Every issue that arose during the process needed to be analyzed to determine areas for future optimization. For our IRP process, this involved an in-depth validation and analysis into each associated sub process, to verify accuracy and precision, and the implementation of this process at a consumer and industrial level. One industry that can benefit immensely from customized products is the medical field. Specifically for this project, a case study involving the development of custom orthotic devices was addressed. By scanning a patient's leg, it is possible to create products, like the ankle foot orthotic (AFO), based around their unique features. Through this application, the IRP process can be examined and recommendations can be provided to the project sponsor, Orthocare Innovations, Mountlake Terrace, WA.

2.0 Background

2.1 Integrated Rapid Prototyping

The Integrated Rapid Prototyping (IRP) process is created by combining 3D Digitization, 3D CAD modeling, computational and analytical modeling through Finite Element Methods (FEM), Additive Manufacturing (AM), and non-destructive testing (NDT). Each step contains multiple technologies and processes, each of which must be examined in order to develop an efficient IRP process. The following Sections go through each of the steps and identify key technologies within each step and identify their application to IRP.

2.1.1 3D Digitization

Digitization refers to the representation of an object or analog signal through a series of discrete sets of points, thus creating a digital representation of an object. In terms of three-dimensional (3D) digitization for an object, the primary component in its success requires acquiring its precise dimensions through the use of a scanning device. The scanner analyses either an object or environment and creates a point cloud from the geometric samples on the surface of the object as a form of data acquisition. Points located on the surface can be used to extrapolate its shape depending on the type of scanning used. Classification for 3D digitization exists in two major forms, contact and noncontact. Contact data acquisition extrapolates data through means of contact measuring where physical contact is made with the surface of the object. Non-contact data acquisition uses a form of energy source, such as light or sound, to obtain the 3D data without touching the surface of the object in the measurement [3]. Non-contact is further subdivided into two categories, passive and active, based on their differing acquisition methods, as shown in Figure 1.

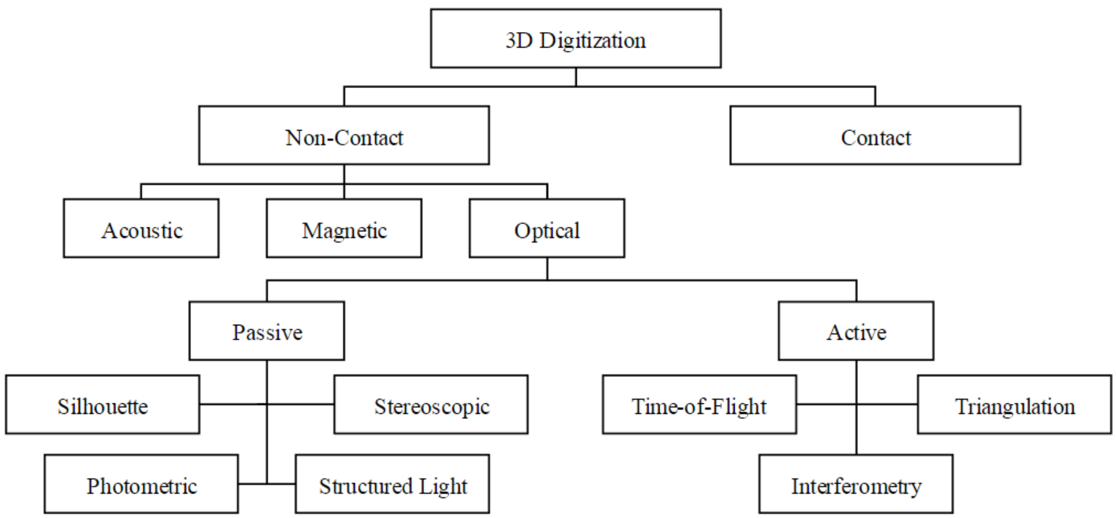

Figure 1. Contact and Non-Contact Classification of 3D Digitization Methods [3-7].

Passive systems utilize the detection of reflected light found within ambient radiation but do not emit radiation themselves. Use of visible light is the preferred type of radiation due to its availability, usually involving stereoscopic, photometric (photogrammetric), and silhouette types of digitization. Stereoscopic systems make use of two cameras, angled towards one another, to determine point distances from subtle differences in image captures via triangulation [4]. Systems employing photometric, or photogrammetric, methods involve single camera usage to capture multiple two-dimensional (2D) images, with minimal illumination, for obtaining pixel surface orientations in shape reconstruction (shape-from-motion). Lastly, silhouette systems capture a sequence of images of an object's outline, done through a complete rotation about the object and a high contrast background. The silhouettes formed are extruded and intersected to generate an object's approximate virtual representation [5].

Active systems project a directed form of energy on an object and either uses position detection for measurement or capture controlled changes from sensor parameters. Active is further subdivided into physically distinct categories: time-of-flight, triangulation, and interferometry. Time-of-flight, often referred to as laser pulse scanning, is a method which directly measures the time between transmission and reception of light being reflected from an object's surface, or the round-trip time from a pulse of light which is used to calculate the distance from the object [6]. Due to its moderate resolution, time-of-flight is mainly suitable for long range applications. Triangulation techniques incorporate the use of laser light projected on an object to determine its surface location. The camera system views the projected laser at varying angles depending on their relative distance as it deforms about the object [4]. A basic triangular arrangement of known dimensions exists between the camera system, projected laser, and object, capable of reconstructing the object's initial shape. Interferometry methods use evenly paired distributed patterns, or gratings, to generate unwrapped phase maps. The projected light is reflected off of an object's surface where the interference is determined from the phase shift between reference and reflection points [6].

Structured light style systems project simultaneous mathematically patterned light, such as stripes, onto an object and acquire the geometric deformations produced by the object's surface [4]. Different techniques within structured light exist depending on the type of pattern in use, which can be generalized under either laser interference or projection. Such methods for projection include the use of arbitrary fringes for continuous data gathering, as seen in sinusoidal fringe projection, and digital light processing [6].

Hand held laser scanners in particular allow the user to generate an image through triangulation, where a sensor picks up the distance to the surface of the object. The data collected are stored within an internal coordinate system and recorded as data points in a three-dimensional space or point cloud. Through data processing, a triangulated mesh can be generated in correlation with the set of recorded data points thus creating a computer-aided design (CAD) model. The final result is an editable software file in a data transmission format, such as an STL (STereoLithography), with the 3D representation of the object able to be manipulated using CAD software.

Full-field optical data acquisition techniques have a wide range of applications mainly involving surface topography and topology. Manufacturing and process control can see benefits from the use of these techniques as methods to provide accurate measurements depending on the resolution from the scanning device. Other aspects include the replication of designs for reverse engineering, remote inspection, historical preservation, medical imaging, and customization [8]. For a table of comparisons between of available scanning devices refer to Appendix A.

2.1.2 3D CAD Modeling

3D Computer Aided Design (CAD) software allows the user to create and modify the 3D representations of parts or components by adjusting dimensions and geometrical features, called 3D Solid Modeling [9]. Examples of software likes this include

SolidWorks, Inventor, and Creo [8], [10], [11]. Both standalone and additional add-on software for pre-existing software packages allow users to import and work with 3D mesh and point cloud files in the CAD environment. An example of an add-on software package is ScanTo3D for SolidWorks. AutoDesk AutoCAD come with a similar feature already built into the software [12]. Finally, an example of a standalone software package designed for just this purpose is Geomagic Design X [13]. This style of software allow users to access basic tools for editing point cloud files by removing noise, or excess data. Users are then able to fit geometric shapes or free form surfaces to the sections of the data, thus creating a solid model.

2.1.3 Additive Manufacturing

Additive manufacturing is a fabrication technique that has the ability to drastically change how products are manufactured. It differs from most machining operations which work under the principle of subtractive manufacturing. An additive manufacturing machine creates a part in layers, stacking one on top of the other to create the full product. It has grown from a tool used by designers to quickly make prototypes, to manufacturers using it to create final products, to a tool used by consumers to produce goods of their own [14]. Additive manufacturing has the ability to quickly fabricate parts that would otherwise take a significant amount of time using traditional fabrication methods.

A wide variety of additive manufacturing processes exist today. Stereolithography, one of the very first additive manufacturing processes, uses this technology to create products by hardening a photosensitive resin layer by layer. Selective Laser Sintering (SLS) unlike Stereolithography, uses a laser to fuse a powder substance in the appropriate location [15]. Fused Deposition Modeling (FDM) uses a heated extruder to melt a plastic filament and place the melted material. This is one of the most cost effective technologies because of the cheaper materials, lack of post processing, and cheaper machines. However, the tradeoff for the use of FDM is the low resolution of the final product and long process time for larger more complex parts, when compared to other additive manufacturing processes. Similar to Stereolithography, PolyJet uses a photosensitive material but instead of the part being submerged in the photosensitive resin, an inkjet head moves around the layer being created and deposits the material, in a similar fashion to FDM. This allows for parts to have slightly higher resolution then FDM, but produces parts that are weaker than parts produced by Stereolithography and SLS [15].

Due to the nature of additive manufacturing, it is often difficult to predict how a product will perform. As explained above, additive manufacturing is a layer by layer process that joins the newly placed material to the rest of the product. This is normally done through application of heat, sometimes done by lasers or electron beams. This changes the material properties from what is chosen by directly affecting the microstructure of the material. In addition to this, plastic parts have residual stresses from the printing process, which affect their geometrical accuracies and performance [16].

3D printing has applications in a wide variety of settings, from medical to factories. Creating processes for mass customization, creation of individualized goods for the consumer, has the benefits of addressing current problems in manufacturing such as changing consumer desires or even improving the quality of life [17]. In terms of medicine, 3D printing already has a foothold. Currently, there are practitioners producing customized dental implants and prosthetics using 3D printing during fabrication [18]. Additive manufacturing in the industry has the potential to add new functionality, such as dental devices, due to the essentially limitless complexity of parts that can be fabricated including customization of prosthetics. Currently, there exists a software package to create models for dental surgical drill guides that can then be sent to an additive manufacturing machine [19]. Technology like this allows for the more complex process of creating these drill guides to become much simpler.

2.1.4 Finite Element Methods

Researchers have used Finite Element Methods (FEM) modeling to simulate conditions within certain situations and optimize designs [20]. FEM discretizes a model into smaller uniformly shaped components known as elements [21]. These components and their connections to each other are known as nodes. The combination of elements and its nodes create a mesh to cover the model. Setup parameters of the simulation are then applied to the mesh, such as material properties, loads, boundary conditions and other design performance conditions. FEM solves a series of equations representing physical phenomena using matrices [22]. The stresses, strains, and deformations results at each node and element are represented as distributed fields and can be used to determine where the maximum stress and strain, and deformations concentrations occur on the orthotic and based upon these concentrations, dimensions can be adjusted to match the stresses and deformations for commercial orthotics.

FEM is a complimentary technology to physical testing for many reasons, including cost. The setup for FEM is done by creating or transferring a design model from a CAD software and applying material properties, loads, boundary conditions and other design performance conditions which allows for improved testing of design parameters (thickness, height, and width). The investigations are used to improve AFO performance and reduce manufacturing costs [20]. FEM also has advantage of the ability to display physical responses of the model such as stresses, strains, and deformations over the entire body rather than just looking at sections.

There are many FEM simulation software available today. Some of the most widely used commercial FEM software are Abaqus, Comsol, and ANSYS. Abaqus' simulation package includes CAE, Structural, CFD, and Multiphysics [23]. COMSOL's simulation package includes Electrical, Mechanical, Fluid, and Chemical [24]. ANSYS' simulation package includes Electronics, Fluids, Structures, and Multiphysics [22].

2.1.5 Digital Image Correlation

Digital Image Correlation (DIC), a noncontact optical method for pixel image tracking and registration, is used to measure 3D displacements within specimens for experimental mechanics. It is primarily used to quantify mechanical material properties and behaviors undergoing varying loading conditions in full-field. In general, DIC uses a single camera setup to capture 2D fields but this limits the capture to in-plane deformation measurement of nominal planar objects which are susceptible to out-of-plane displacements in post load testing [25]. Using a synchronized stereo system allows for full-field 3D capturing capable of simultaneously measuring shape and all displacement elements for planar and nonplanar specimens [26]. Two charge-coupled device (CCD) cameras track simultaneous changes in subsets, gray value patterns in adjoining pixels, during deformation capturing. Each subsets' unique gray level light intensity does not change throughout the duration of deformation, allowing for its tracking. The tracking of the speckle subsets allows for the measurement of surface displacements in the evaluation of specimen behavior when the specimen is subjected to various loads [27]. A reference image, taken prior to a load application, is cross-correlated with the subsets of an image taken during the time of deformation, as shown in Figure 2. A correlation function uses the average squared difference sums of each subset value to determine changes between the two images [28]. Tracking is performed via shifting of the subsets until a match is found between the pattern of both the reference and deformed image [29].

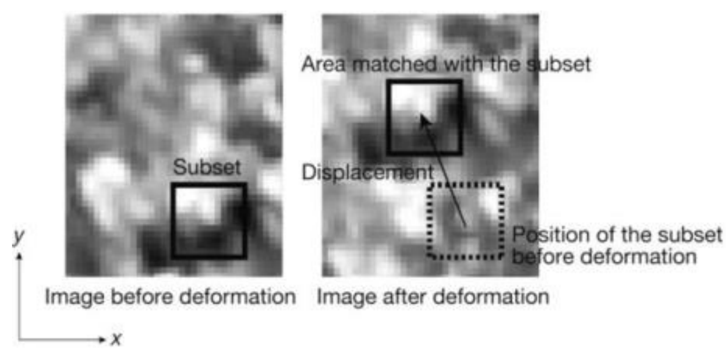

Figure 2. Digital Image Correlation Subset Matching for Determining Deformations [30].

In order for appropriate pixel subset identification, all specimens must be prepared through the application of a speckle pattern, a randomized dot pattern, located on the surface of the specimen. Speckle patterns must be isotropic, non-repetitive, and high in contrast to obtain accurate results. With the use of computer software, pattern differences or deformations can be virtually mapped by relating the images derived from the correlation comparisons. After calibration parameters, including position and orientation of the cameras, have been determined the specimen can be reconstructed using stereo-triangulation from camera data.

2.2 Application of IRP Process to Custom Orthotics

The IRP process was applied to the creation of a customized ankle foot orthotic (AFO). This was chosen as the application due to the need of customized AFOs with increased comfort and performance for the user and the desire to reduce the production time of the current custom AFO production process. The ankle-foot orthotic device helps patients who suffer from a variety of foot problems, which include foot drop. An AFO will help patients with foot drop by supporting the foot in a proper position during gait instead of dropping or dragging on the ground.

2.2.1 Anatomical Terminology of Human Lower Extremities

A primary focus is placed on ankle and foot movements as our case study deals with orthotic devices limiting dorsiflexion and plantarflexion during abnormal gait cycles. Dorsiflexion, a flexor response, is defined as ankle and foot movement towards the anterior tibia, a rotation of the foot with the toes upward. Plantarflexion, an extensor response, corresponds to the foot movement away from the tibia, with the toes pointed downwards [31].

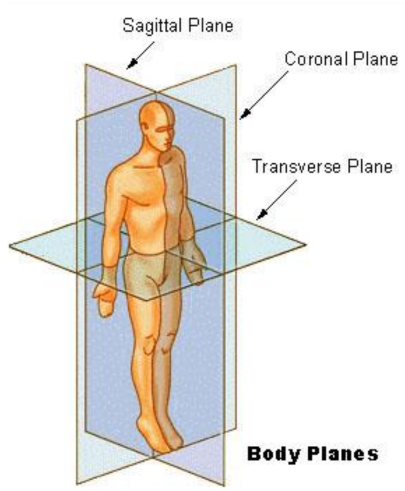

Figure 3. Human Anatomical Planes [32].

Both dorsiflexion and plantarflexion are observed in the sagittal plane, as shown in Figure 3, to provide accurate muscle and locomotion activity for human subjects. Equal restriction of inversion and eversion of the foot in the frontal plane, as shown in Figure 4, and adduction and abduction in the transverse plane is needed to maintain a normal gait pattern [34]. Each planar movement is essential in the prevention of foot slapping or dragging during walking, an effect often encountered in abnormal gait patterns.

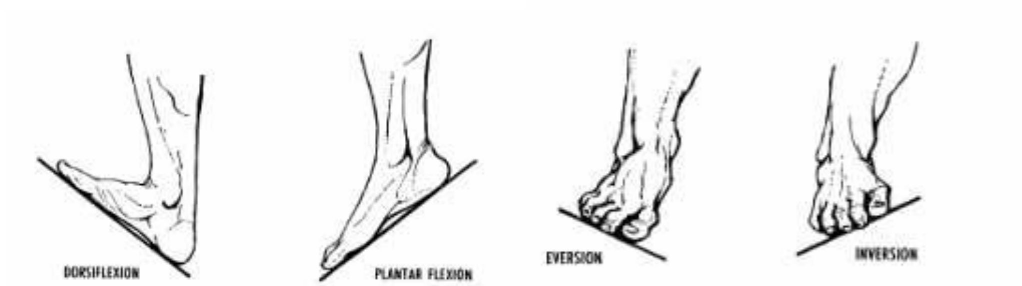

Figure 4. Foot Movements Observed in the Sagittal Plane and Coronal Plane [33].

2.2.2 Normal Gait Cycle

Normal gait, composed of two phases, stance and swing, represents a clear cycle of locomotion without impairment to varying parts of the body measured from heel strike to heel strike within the same foot. Each division, approximately 60% stance phase and 40% swing phase, make up for the entirety of the gait cycle, Figure 5, with distinct differences between the two. Stance, beginning with initial contact, or heel strike, and ending with toe push-off, is the period in which the foot remains in contact with the ground while accepting weight [34]. As opposed to swing refers to the forward motion of the foot normal to the plane of motion without coming into contact with the ground [35]. Stance phase is equally the weight-bearing phase requiring the greatest stress, where a force is applied in contrast to the ground.

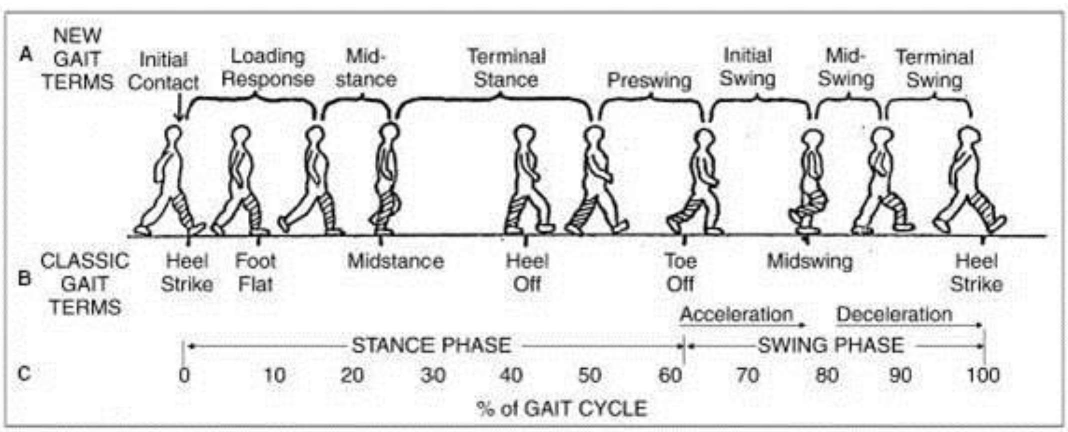

Figure 5. Complete Normal Gait Cycle [36].

The stance phase is further subdivided into multiple separate phases of motion: heel strike, foot flat, mid-stance, heel-off, and toe push-off or toe off. During the heel strike sub-phase the ankle joint in the foot experiences neutral dorsiflexion (extension) and plantarflexion (flexion) in which the foot is raised, marking the beginning of the stance phase and initial weight acceptance.

The next sub phase in the stance phase is flat foot, or loading response, which occurs when the entirety of the foot comes within full contact of the ground. Full body weight is then mitigated along the bottom surface of the foot throughout the remaining sub-phases: mid-stance and toe-off [37].

After the foot flat sub phase the mid-stance sub phase begins as the leg approaches a near vertical position. This phase is defined as the instance the body becomes aligned with the supporting limb as the opposite limb is swinging which is classified as single limb support [38]. A change from plantarflexion to dorsiflexion can be observed as plantar flexors contract for limb control over the foot [39]. Maximum weight acceptance and stability take place as the total weight-bearing surface of the foot remains stable and in full contact with the ground [39], [40]. Body weight is eventually transferred to the forefoot as the body advances causing the heel of the foot to rise.

After the mid-stance subphase comes the heel off subphase, also referred to as terminal stance. During this subphase the forefoot now serves as the primary weight bearer during the rising of the heel, signaling the start of the heel off phase [41]. As the opposite limb makes its way past the stable foot towards the walking surface, plantar flexors, muscle with plantar flexor control, in the ankle activate in preparation for toe push off [39]. The forefoot, composed of the ball of the foot and toes, remains flat on the ground as the heel rises [42].

The final subphase of the stance is the toe push-off, or toe off phase, directly following the heel-off phase position. Often called pre-swing, toe-off is characterized as the period in between which both the toes of the support foot are in contact with the walking surface and when the toes have left the surface [39]. Toe-off signifies the start of the swing phase and the end of the stance phase [39], [40], [42].

Swing phase begins at the end of the toe-off sub-phase from the grounded foot and ends at the opposite foot heel strike contact. Swing phase is broken up into three major sub-phases: initial swing, mid-swing, and terminal swing [43]. Initial swing refers to the swinging acceleration of the lifted foot as it moves to become adjacent to the opposite foot underneath the body. The next sub-phase is mid-swing where limb advancement continues, marking the point where the lower swinging extremity is directly beneath the body transitioning from acceleration to deceleration. Terminal swing signals the end of the swing phase as the limb decelerates and prepares for heel strike restarting the gait cycle. A 90˚ angle between the bottom surface of the foot and posterior of the leg is maintained by the ankle in continuation of the gait cycle.

2.2.3 Foot Drop

Foot drop, sometimes called drop foot, is an abnormal condition in which muscular weakness or paralysis of the foot and ankle causes a loss of dorsiflexion during locomotion as exemplified in Figure 6. People experiencing foot drop have difficulty lifting their forefoot during the stance and swing phases of the gait cycle. Weak muscular response in the heel strike phase and toe push-off phases can cause someone to inadvertently slap and drag their foot onto the ground [44]. During heel strike, the forefoot will make initial contact, rather than the heel, by slapping onto the walking surface. Without proper dorsiflexion, dragging of the foot, specifically toes, will occur in the toe push-off phase.

The insufficient muscle response does not allow for the necessary ground clearance needed during the swing phase of gait for limb advancement.

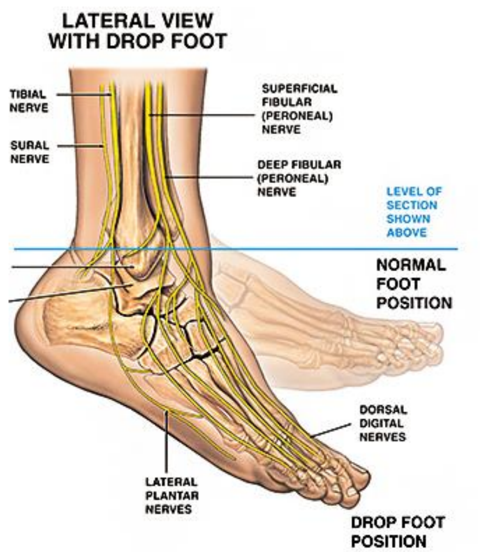

Figure 6. Foot Drop Position Compared to Normal Foot Position [45].

The loss of ankle joint control often requires individuals to lift their foot at higher levels to compensate for the dragging [46]. The disturbance caused by the lifting is referred to as steppage gait and can be accompanied by an exaggerated swinging motion of the hip. A motion used to propel the forefoot forward and avoid the toes from sticking on the ground [47]. These effects are experienced as symptoms for a complexity of medical problems whether they be neurological, muscular, or anatomical in origin. Causes of foot drop can emerge from nerve injury, muscle disorders, and brain or spinal cord disorders affecting the primary ankle dorsiflexor and toe extensor muscles. These muscles are comprised of the tibialis anterior, extensor digitorum longus, extensor hallucis longus, and common fibular nerve [48]. Compression or damage of the common fibular nerve, winding around the neck of the fibula, will result in a loss of dorsiflexion and eversion. Muscular issues like stroke, multiple sclerosis, cerebral palsy, and Charcot-Marie-Tooth disease caused by neurodegenerative brain disorders will include foot drop. In terms of muscle disorders, muscular dystrophy, polio, and Lou Gehrig's disease have been equally associated with foot drop [48]. In order to treat its effects, individuals are commonly given light-weight below the knee braces and shoe inserts, known as ankle-foot orthotics (AFO), to support the foot throughout the gait cycle [46]. The brace provides for a normal range of motion to the ankle and foot by counteracting the loss of dorsiflexion thus alleviating the issues of foot drop. Many studies on AFOs show a significant difference in the kinematics of the ankle that improves walking velocity, stride length, and cadence [49].

2.2.4 Ankle-Foot Orthotic Origins

Since humans could walk, diseases and injuries have caused impairment in movement. Over the last five hundred years, the development of short leg braces to treat these issues became documented. The first braces were made out of iron and leather from a local blacksmith, usually as an attachment to a shoe [50]. Ambroise Pare, a famous surgeon in the 16th century, was assisted by armorers in the crafting of artificial limbs and iron braces including a clubfoot boot [51]. At the beginning of the 20th century, the short leg braces began being made out of different metals such as Stainless Steel and Aluminum. The braces were now named Below Knee Orthotic (BKO), referring to a double upright brace. The 1970's brought a revolution to the braces. Plastics became strong and durable enough to be used for the braces. This brace lead to the creation of a new orthotic called the ankle-foot orthotic (AFO) [50]. AFOs can come in different shapes and sizes, as well as custom or standardized. A standardized AFO is shown in Figure 7.

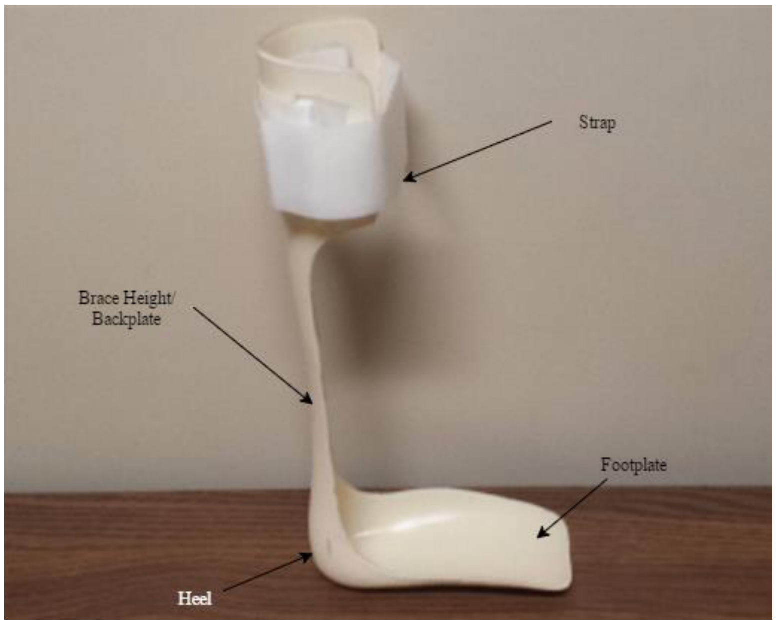

Figure 7. Standard AFO with Different Sections Labeled.

2.2.5 Benefits of Ankle-Foot Orthotics

Orthotic Devices help heal or prevent injuries resulting from pressure distributions, as well as improve balance and comfort while walking. An AFO can help a patient by redistributing the plantar pressure load on the foot to the arch of the foot rather than the heel of the foot [21]. This redistribution of pressure reduces pain by having the pressure normally distributed instead of concentrated in one area. AFO's are used to help correct a person's gait to reduce the risk of falling or tripping by improving their balance.

2.2.6 Conventional Methods to Create an Ankle-Foot Orthotic (AFO)

Current AFO manufacturing processes are presented through a guideline from the International Committee of the Red Cross [52]. The first step after identifying the need for an AFO is creating a cast of the patient's leg. A negative cast, which is an outer mold of an area of the body that is hollow, is made of the leg. From the negative cast a positive cast, a replica of the area in question, is made. This cast is used to shape and mold the AFO for the patient, a process that can take up to 4 weeks [53]. Depending on the patient's leg shape, size, and overall weight, different dimensions of the starting polypropylene sheet are used in the vacuum molding process. This is then trimmed based on the data collected from the cast to finish the production of the AFO [52]. The next appointment is the actual fitting of the AFO to the patient. A trained orthotist trims and adjusts the AFO using prosthetic and orthotic standards [52], [54]. This adjustment ensures that the device functions in the way it is intended, depending on the type of AFO and the needed benefit of the patient, provides full range of motion, and is comfortable for the user [53], [54].

2.2.7 Constraints for Conventional Production of Ankle-Foot Orthotics

The traditional manufacturing process of AFOs is time consuming, relies on impression casting, and requires a high level of experience and craftsmanship by a certified prosthetist and orthotist. The form of the leg is captured by wrapping a sock and casting the leg as seen in Figure 8A. Once cut into shape, the cast is filled with plaster in Figure 8B. Once the plaster has set, the cast is cut in line with the tibia seen by Figure 8C. Key surfaces are marked by embedding stables and coated over with plaster shown in Figure

8D. After the plaster sets, pre-heated polypropylene sheets are vacuum formed around the plaster in Figure 8E. Once the plastic sheets have cooled, the excess plastic is cut, ground down, and smoothed as seen in Figure 8F. The performance of traditionally manufactured plastic AFOs are dependent on the parameters of the fabrication techniques (accuracy of the cast, vacuum seal, and material removal) that can depend on manual work which decreases the consistency of the AFOs performance. This results in undesired manufacturing variability of the quality and/or performance of hand-made AFOs [55].

Figure 8. Traditional Fabrication Process for Custom Ankle Foot Orthotics [55].

3.0 Integrated Rapid Prototyping: Methodology

The objective of this project was to develop a process from conception to realization to effectively engineer a product and demonstrate its application through custom orthotic devices by providing an alternative, quantitative methodology. The process included 3D scanning the patient's leg, created a CAD model of the leg, forming the AFO model around the leg, analyzing the model, producing the AFO via additive manufacturing, and testing the performance with NDT. The IRP process for the creation of a custom AFO process is described in Figure 9, which consists of three main components: 3D digitization, 3D modeling, and AFO creation.

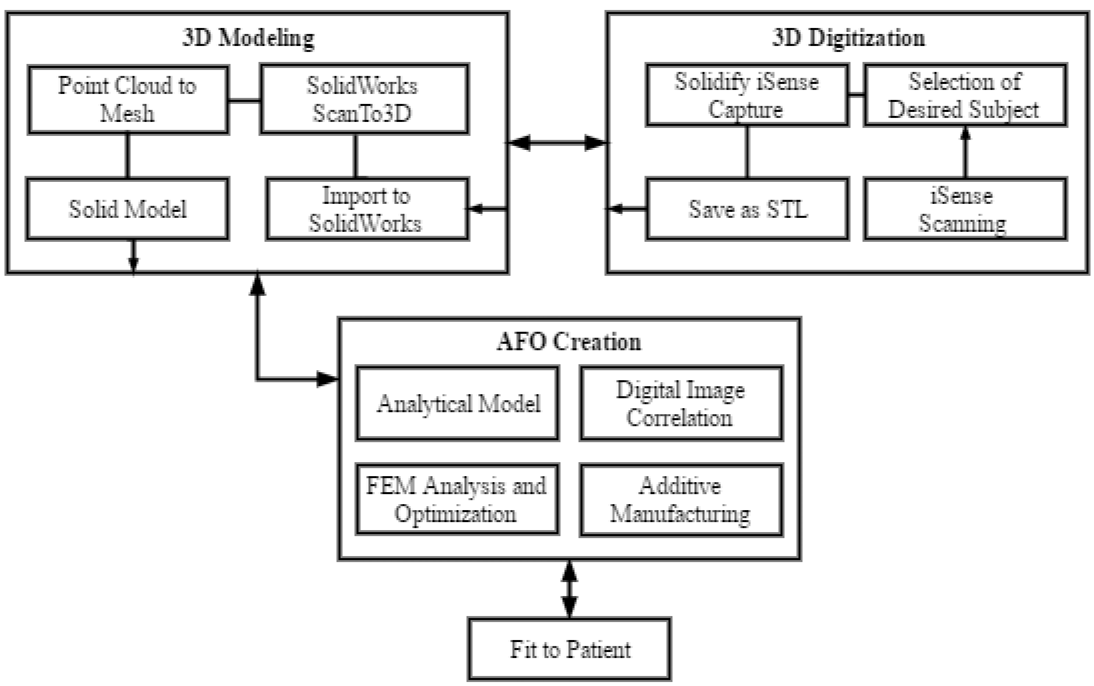

Figure 9. Subprocesses Involved in the Creation of Custom Orthotics by Integrated Rapid Prototyping.

3.1 Full Field 3D Digitization (Scanning)

To collect data of an object a full field 3D portable scanner was used. The particular scanner used was the iSense 3D scanner by 3D Systems for use on an Apple iPad Air 2 [56]. This scanner is an attachment to an Apple iPad which makes it very easy to use and maneuver around the object being scanned. To take a scan using the iSense the Sense application needs to be downloaded from the App Store on the iPad. Within this application the user can see a cubic wireframe indicating the volume in which the scan can be taken. This volume can be adjusted to fit the size of the object. Once the scanning volume is set and the object is centered, the scan is started by pressing the play button within the application, as shown in Figure 10.

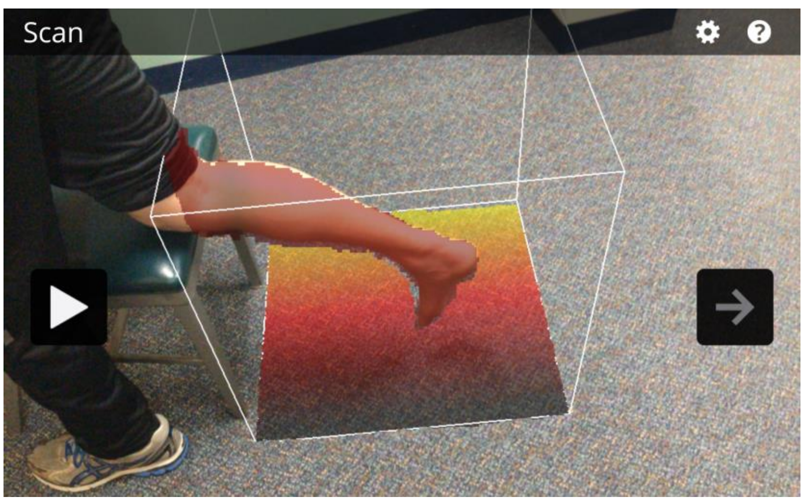

Figure 10. iSense Scanning Volume Encompassing the Leg.

Once the scan starts, data are collected through the iSense by projecting an infrared fixed randomized dot pattern onto the object of interest while the iSense camera tracks the position of the pattern onto the object. Figure 11 shows a representative image of the projected pattern on the object.

Figure 11. iSense Projected Dot Pattern on Leg. An Infrared Camera was used to Observe the Dot Pattern.

These data are relayed into the iSense application and seen as gray points being placed over the object creating a 3D version of the object in the iSense application, as seen in Figure 12. To collect all of the data for an object, the iSense needs to be moved all around the object so that every point of the object is seen by the projected dot pattern, as shown in Figure 13.

Figure 12. Data Collected During iSense Leg Scan.

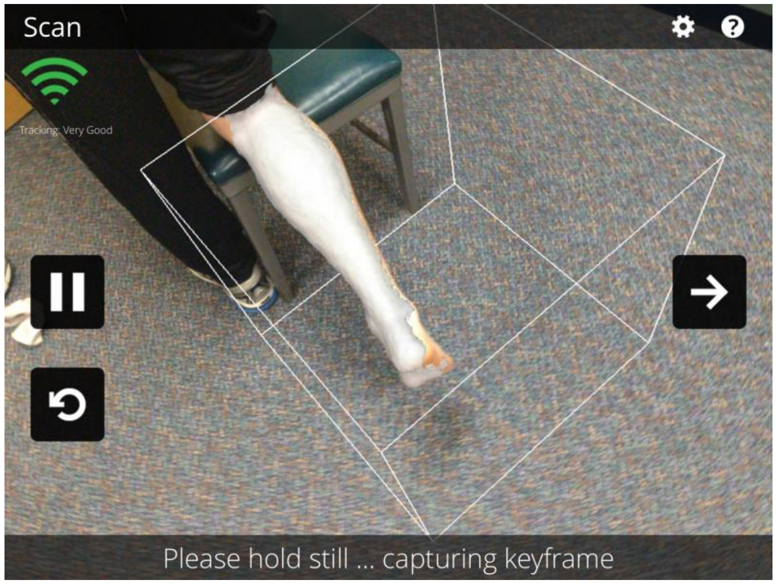

Figure 13. iSense Data Collected While Moving Around Leg.

Once all the data for an object are collected the scan is stopped and the model is generated, shown in Figure 14. The model can then be edited to remove any extra objects that may have been picked up by the scanner. This can be done in the iSense application through the erase tool or trim tool.

Figure 14. Leg Scan Data in the Edit Features of iSense.

The iSense application also has an option to solidify the part which will take it from a surface body of an object to a solid body by creating material where there are any holes in the scan, as shown in Figure 15. The solidify option will create flat faces across holes so it works well if the object being scanned has a flat face in contact with a table.

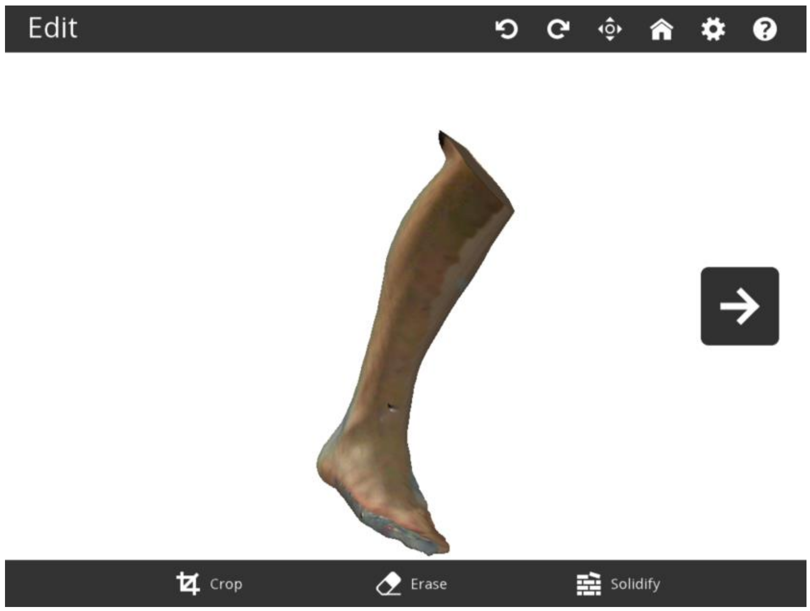

Figure 15. Leg Scan Data After iSense Solidify Function.

Once the scan model is complete, it can be saved to the iPad as a STL file, an OBJ file, or a PLY file. To retrieve the file from the iPad the user must connect the iPad to a computer that it is authorized to connect to iTunes™ with. The files from the iSense application can be found in the apps section of the iPad and in the iSense application tab. The files can then be saved to folders on the computer or a USB drive connected to the computer.

An efficient procedure for collecting scan data was developed for the iSense using the iSense application: position the object so that the smallest area is touching the ground or table, adjust scan volume to fit the object, start scan while slowly moving around the object, use iSense application editing tools to remove unwanted objects as well as solidify if needed, save scan as STL file, retrieve scan from iPad through iTunes™, and import STL file into CAD software to complete the scanning process. This procedure was used for all scans performed so that the data collection method was consistent between scans.

The final scanning procedure was used to get scan data for a Standard AFO as well as a leg scan for the creation of a Custom AFO. To scan the Standard AFO it was first painted with an acrylic paint as there were errors when the iSense tried to scan a semitransparent object such as the Standard AFO. Once the Standard AFO was painted it was placed on a table upside down to reduce contact area with the table as seen in the Figure 16. This allowed for the iSense to collect the most amount of data from the Standard AFO while only relying on the solidify function for a small part of the AFO.

Figure 16. Standard AFO in Scanning Position for Maximized Data Collection.

The resulting scan was then saved as a STL file so that it could be imported into FEA and CAD software for analysis. To get a leg scan for the Custom AFO creation the person whose leg was being scanned would kneel on a chair so that the calf and foot were hanging out in the air. This position can be seen in the Figure 17 along with the iSense capturing of the leg data.

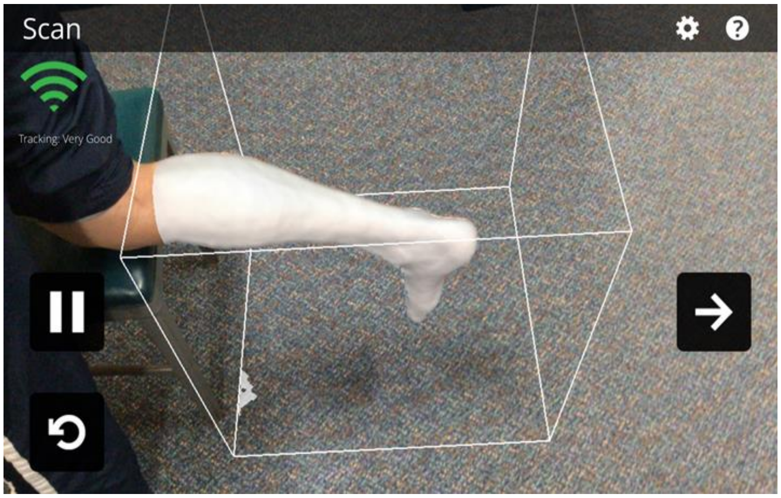

Figure 17. Scanning Position and Capture of Leg.

The person would have their foot pointing straight down so it was as if they were standing straight which would allow for the features such as the arch, blade, heel, and ball of the foot to be scanned. This scanning position also allowed the operator of the iSense to move quickly around the person's leg as to collect scan data in a short timeframe. Getting all of the scan data in a short timeframe is important because if the leg moves at all during the scan then the iSense would try to overwrite previous scan data causing some data to be lost. It is very important to not lose any data as the custom AFO would need to be design to fit the features of the leg. Once the scan was completed, the leg was saved as a STL file so that it could be imported into CAD software and the custom AFO could be created.

3.2 3D CAD Modeling Procedure for Custom AFO Generation

SolidWorks was chosen for the modeling portion of the project due to the ScanTo3D feature, as well as the surface modeling abilities of the software. ScanTo3D is an essential tool for this process, and is available as an add-on to SolidWorks' Premium and Professional software packages. It allows SolidWorks to interact directly with STL and other mesh files, as opposed to using the STL as a graphic or converting the triangulated faces into SolidWorks surfaces, which is vital to effectively working with mesh files. This add-on offers some key tools for creating the AFO, Mesh Prep Wizard and Surface Wizard. To create the customized AFO the following steps were used:

1. Adding the ScanTo3D add-on to SolidWorks
2. Importing the STL file containing the triangulated mesh of a leg
3. Use the Mesh Prep Wizard from ScanTo3D
4. Use the Surface Wizard from ScanTo3D
5. Create a 3D Sketch containing the guide points and guidelines
6. Create the outline of the AFO on the plane that lies at the center of the leg
7. Create a split line feature on the legs surfaces using the outline sketch
8. Create a Surface Knit feature using the surfaces of the leg that would directly interact with the AFO
9. Create a Thicken Feature using the Surface Knit created above

Following the list of steps, the process begins with adding ScanTo3D to the SolidWorks software package, as shown in Figure 18, and importing the mesh file of the patient's leg as shown in Figure 19.

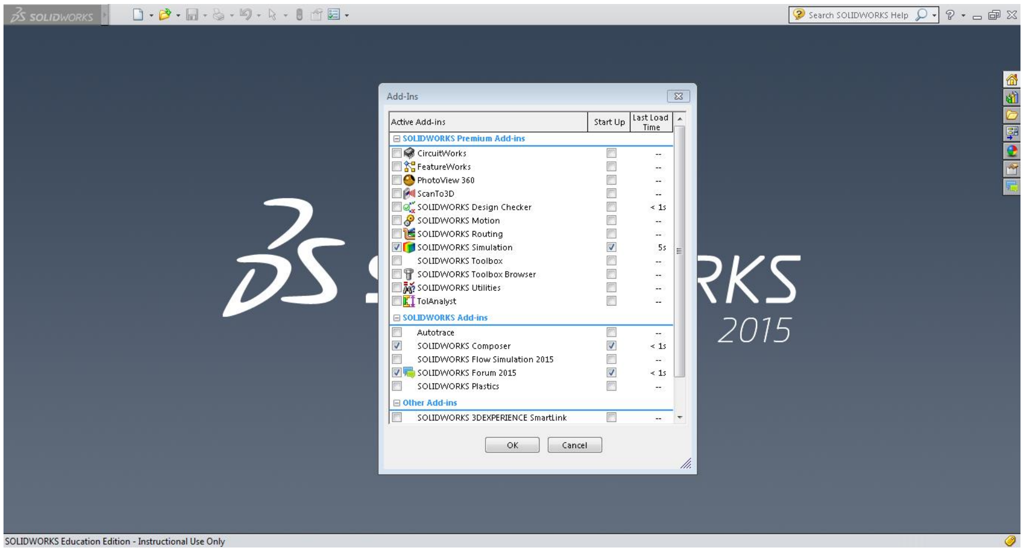

Figure 18. Add In Menu for SolidWorks ScanTo3D Feature

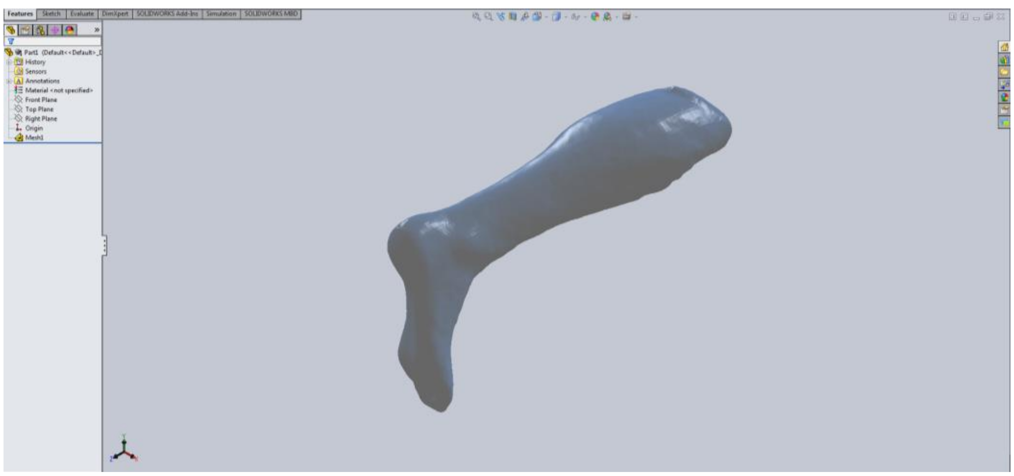

Figure 19. Leg Scan Data Imported into SolidWorks from iSense.

The next step in the modeling process involves using one of the tools from ScanTo3D, the Mesh Prep Wizard. Using this tool, the leg file was repositioned to allow for an easier modeling process. This was done using the automatic option, and then manually adjusting the angles as needed, as seen in Figure 20.

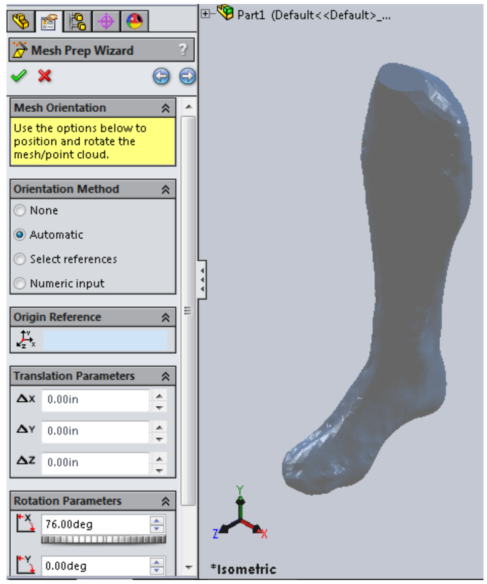

Figure 20. Rotate the Data to Desired Working Position.

The next step in the Mesh Prep Wizard was the selection and removal of outliers in the data, as seen in Figure 21. It is important to note that in this step the data that makes up the top of the leg model was partially removed to create a hole. This allowed the surface modeling strategies employed later to function properly.

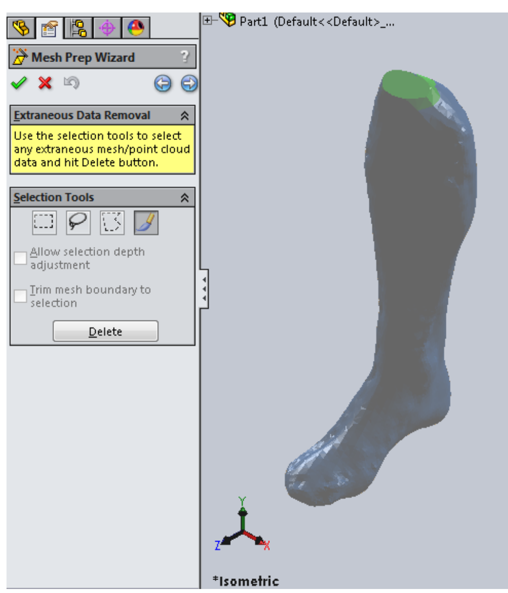

Figure 21. Extraneous Data Removal. Highlighted Section Indicates Data to be Removed.

Following this, any holes in the model of the leg were filled, besides the deliberate hole at the top of the model as seen in Figure 22. The other options in this wizard that were not used are the smoothing options and the simplification options as shown in Figure 23 and Figure 24 respectively. The simplification option removes data points from the point cloud in order to reduce the size. The iSense does not produce a large number of data points so a reduction in total number of points could lower the geometric representation of the object.

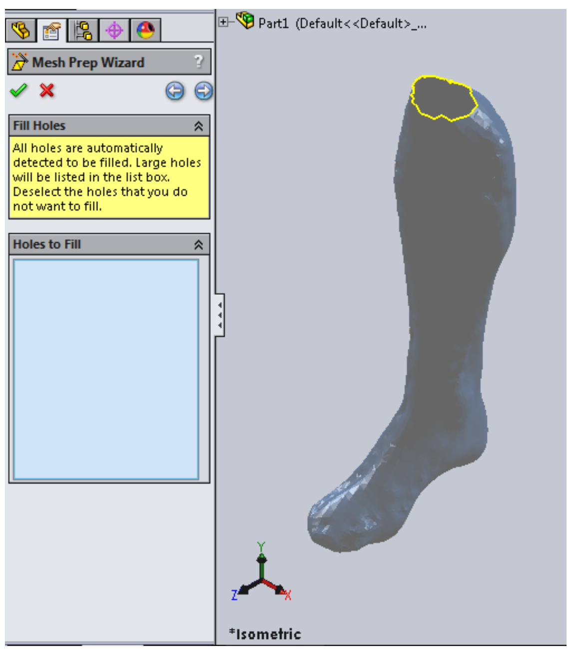

Figure 22. Automatic Hole Filling. Holes to be Filled are Highlighted on Model and Indicated in Dialogue Box.

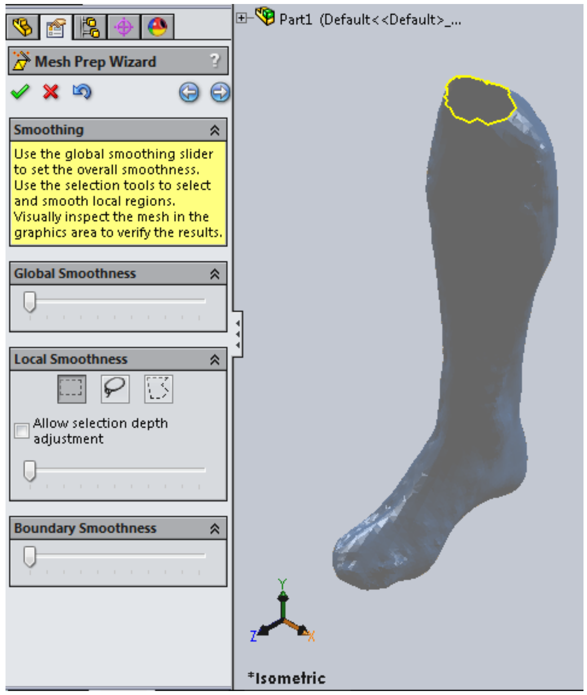

Figure 23. Data Smoothing Tool.

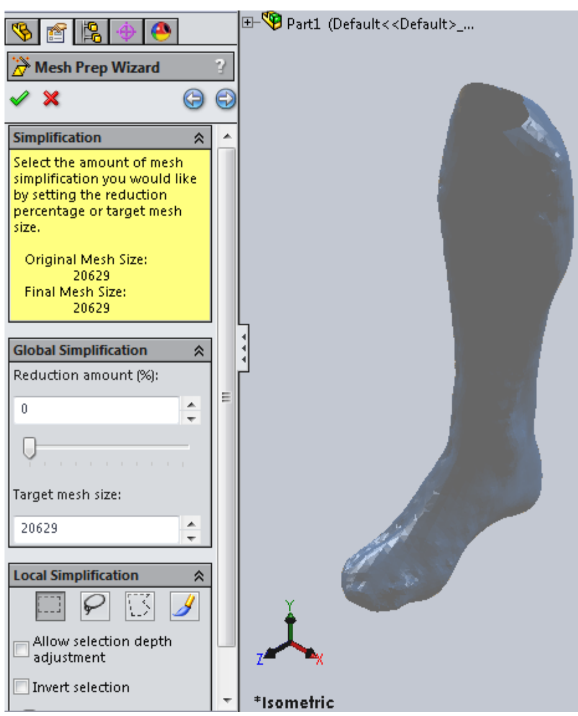

Figure 24. Data Simplification Tool. Simplifies Data by Removing Points.

The fourth step in the modeling process used the Surface Wizard tool. This tool takes the mesh data and fits SolidWorks surfaces to it using free form B-splines. The automatic option in the Surface Wizard was used employing the medium surface level detail option. It is recommended by Dassault Systèmes to use the Automatic Creation feature for anatomical and organic shapes. Once completed, any surface errors that were created were repaired by editing the feature lines of the leg model as shown in Figure 25.

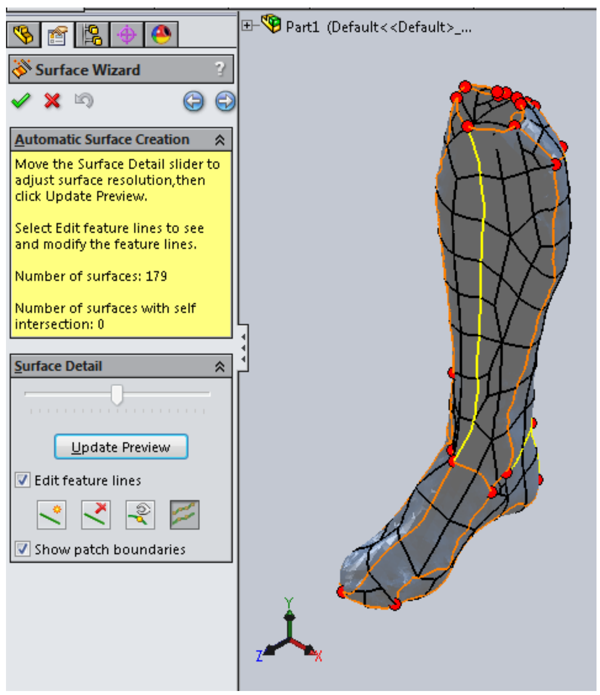

Figure 25. Automatic Surface Creation. Feature Lines are Indicated by Orange and Yellow Lines, Surface Errors are Displayed as Red Wireframe Surfaces.

The fifth step in the modeling process was the creation of the 3D sketch that contained the guide points and lines for the 2D AFO profile. Using the International Red Cross's manufacturing guidelines, guided points and lines were placed in two centimeters below the fibular head, two centimeters behind the malleoli, and under the foot before the toes and metatarsus, as seen in Figure 26. These points were used to create a similar AFO to those already created, and allowed for an accurate outline to be created.

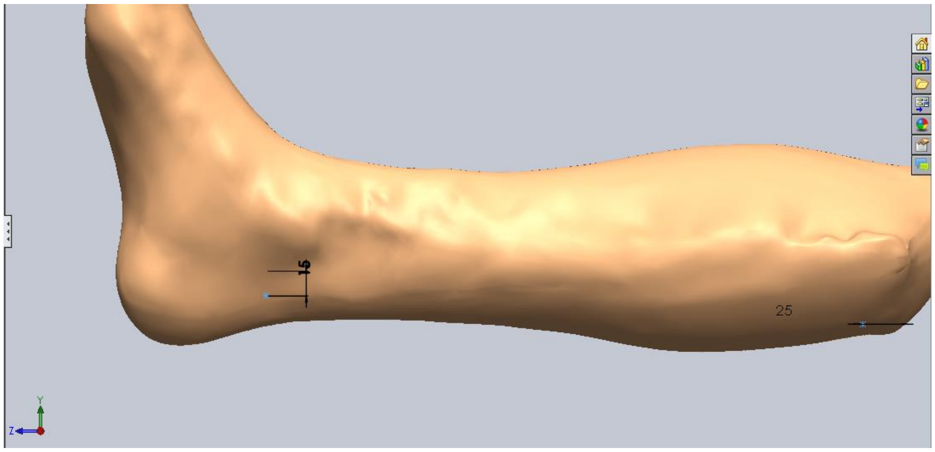

Figure 26. Guide points for Custom AFO Creation
Adapted from International Red Cross Standards.

Using these guide points, the next step was the creation of the AFO outline. This was done as a 2D sketch on the YZ plane, in line with the length of the leg and perpendicular to the sole of the foot, as shown in Figure 27. The profile starts at the guide point created below the fibular head, and follows the general profile of the standard AFO.

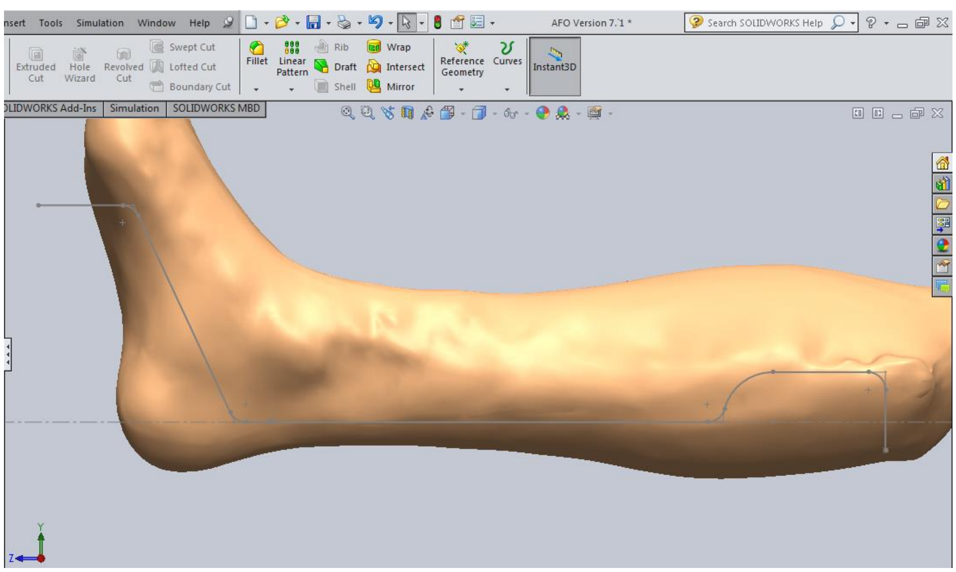

Figure 27. Custom AFO Outline Displayed on the YZ Plane of the Leg.

This profile allows the surfaces that makeup the leg to be sectioned off using the Split Line feature. The surfaces that would directly interact with the AFO are then selected and combined together using the Surface knit feature, seen in Figure 28.

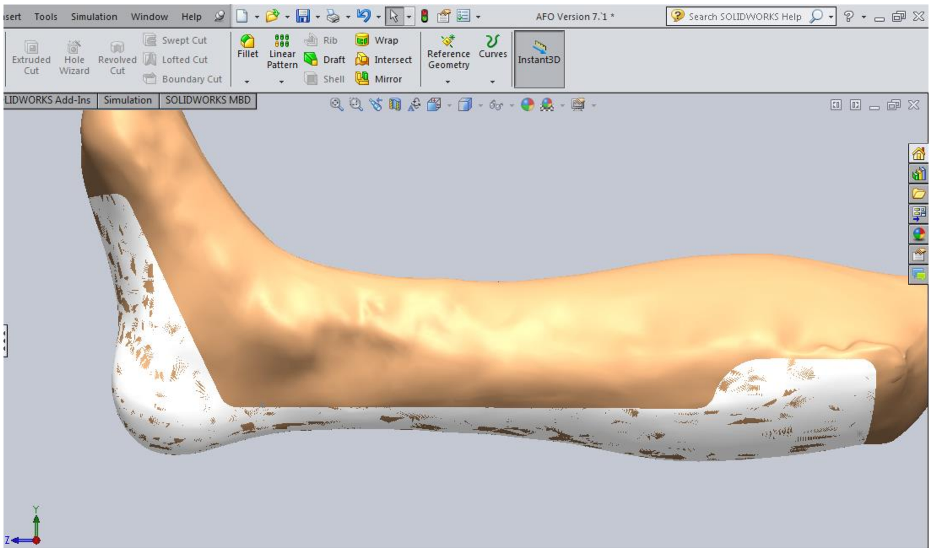

Figure 28. Internal Surface of AFO Highlighted in White Against Leg.

By creating this surface knit, the internal surface of the AFO can be made to match the geometry of the leg as imported into SolidWorks. The final step of the AFO creation process was to apply a Thicken feature to the surface knit, thus creating a 3D solid model of an AFO whose inner surface matches the outer surface of the leg accurately. The final product of this process is shown in Figure 29.

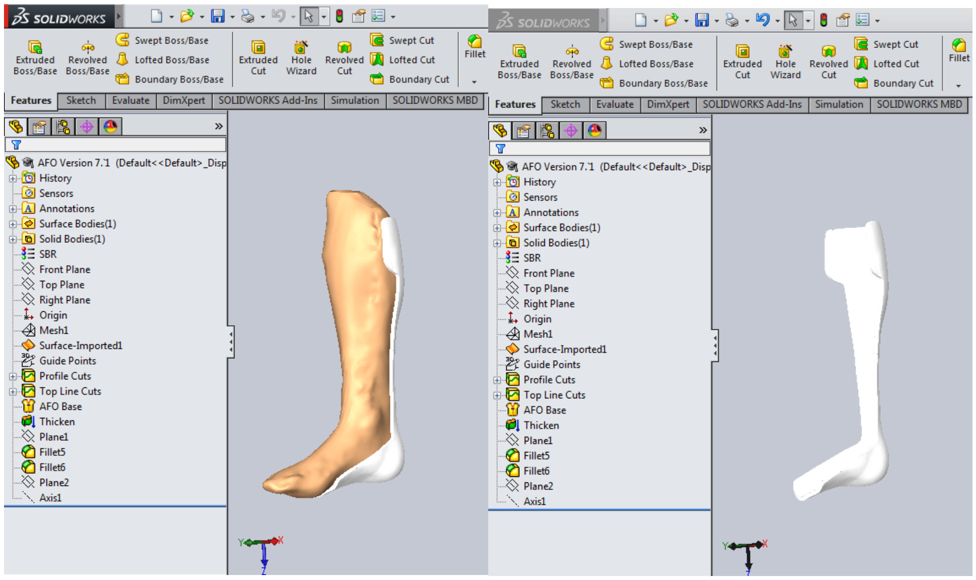

Figure 29. Final Solid Model of Custom AFO with and without Patient Leg.

3.3 AFO Creation

Once the Custom Orthotic CAD model was successfully created with SolidWorks ScanTo3D from the iSense scan, the coordinated application of modeling and analysis, additive manufacturing, and non-destructive physical testing were used to develop a suitable AFO prototype.

3.3.1 Finite Element and Analytical Models

FEM modeling was used to simulate design performance for specific situations and to optimize designs for these situations. These testing simulations involve a process for conceptualizing the physical testing for the design, creating a testing simulation with assumptions, and validating the assumptions through mathematical calculations. The FEM software that was used for this project was ANSYS because of its large variety of mechanical simulations.

3.3.1.1 Basic Setup and Assumptions

For the simulation model, the worst case scenario for the orthotic was tested. The worst case scenario was defined as the top of the brace being fixed with no rotation or translation in any direction and all of the force from the load applied to the front end of the foot plate. This situation created the furthest distance between the fixed area and force, which applied the largest moment on the model. Since the model was only responding to the force and not from the motion, the type of analysis selected in ANSYS was Static Structural, the type of analysis used for a simulation of non-kinetic mechanical parts. This analysis is the most accurate way to solve for strains and deformations in a non-dynamic condition. Initially, material properties of this model were under the assumption of being comprised of isotropic and linear elastic material. These assumptions were later validated and updated experimentally.

3.3.1.2 Finite Element Types

There were three elements types chosen based on the types of analysis and CAD models used; 4 sided surface shell, cubic, and tetrahedral. The cubic produces a cube with eight potential nodes on each corner. The degrees of freedom associated with this element type are deformations in the X, Y, and Z direction. This element type was applied to the simplified part for validation. The reason this was applied to the simplified model is because the geometry of the simple AFO was rectangular with few curved surfaces so the element matched well with the geometry. Also, this element has 8 nodes, which allows for more equations and thus a closer approximation using fewer elements which is more suitable for validating modeling parameters against the analytical models and non-destructive physical testing setup.

The 4 sided surface shell is an element especially designed for surface models. The four nodes can be applied to adapt to the curvature of the surface and then a thickness is applied normally to the surface of the element. This type of element has three degrees of freedom, deformations in the X, Y, and Z direction. This element was selected for the Standard AFO because the Standard AFO was imported to ANSYS as a surface model. The reason the Standard AFO had to be a surface model is because the iSense scanner had difficulty scanning thin walled objects, so the inside of the AFO was scanned as a surface and the measured thickness of the AFO was applied to the surface.

Tetrahedral (triangular) produces a three sided prism with four nodes. The degrees of freedom associated with this element are deformations in the X, Y, and Z direction. This element was applied to the Custom Orthotic because the geometry of the Custom AFO has many curved surfaces and the tetrahedral element is a simpler element with are few nodes per element, so there are more elements which means the elements can adapt better to more complex geometry such as curvature.

3.3.1.3 Convergence

FEM simulates how a model mechanically behaves due to the material properties, boundary conditions, and loads. However, the accuracy of the simulation is based upon elements since the solutions are acquired by evaluating how the loads are transferred within elements, how loads are transferred through nodes, and how many elements there are. The more elements that are created, the more equations that are derived and, in general, the more accurate the simulation is. However, the more elements there are, the more processing power is required to find the solution simulation and the longer it takes to solve the simulation. At a certain point, many elements could be added but the accuracy is only marginally improved. The goal is to find the right balance of accuracy and processing power by creating the optimum. The process of doing this is running many simulations by adjusting the number of elements and plotting the solution over the number of elements which is called convergence. The best solution has the lowest number of elements with an accuracy of roughly 90-95% to the largest solution. The results of the convergence processes can be found in Appendix B.

3.3.1.4 Boundary Conditions Validation Procedure

To make sure the FEM simulation was setup properly, the boundary conditions and loads need to be properly validated.

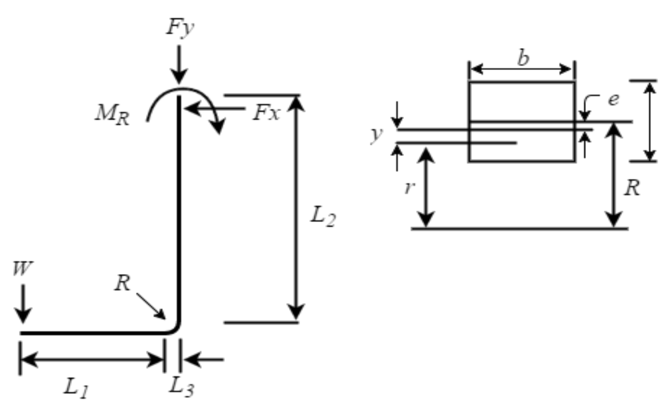

Figure 30. Analytical Model of Simple AFO (L) and Cross Section of Curved Area (R).

To accomplish this, an analytical model was created, Figure 30, as a simple representation of an AFO. In order to create the analytical model for this system, the system was broken down into three subsections: the foot plate (L_1), the backplate (L_2), and the heel (L_3). Each was assumed to be a cantilevered beam with the same cross sectional area, a rectangle with area $a \cdot b$. The material was assumed to be isotropic and linear elastic. These assumptions allowed for the use of simple cantilevered beam equations for stresses given by,

$$\sigma = \frac{M_R \cdot \frac{a}{2}}{I} \text{, and} \tag{3.1}$$

$$\sigma = \frac{M_R \cdot \frac{a}{2}}{I} + \frac{W}{a \cdot b} \text{,} \tag{3.2}$$

where M_R is the reactionary moment, a is the thickness of the cross section, I is the moment of inertia of the cross section, b is the width of the cross section, and W is the force applied. For the curved section, or the heel, normal stresses are computed with,

$$\sigma = \frac{M_R \cdot \frac{a}{2}}{(a \cdot b) \cdot e \cdot r} \text{,} \tag{3.3}$$

$$e = \frac{I}{R \cdot (a \cdot b)} \text{, and} \tag{3.4}$$

$$r = R - e - y \text{,} \tag{3.5}$$

where e is the distance from the centroidal axis to neutral axis, R is the radius of curvature, and r and y are used to locate the area of interest. Using these equations the maximum stress and its location was discovered in the system. In order to calculate strain, Hook's law,

$$\varepsilon = \frac{\sigma}{E} \text{,} \tag{3.6}$$

was used, where ε is the strain in the part, σ is the bending stress, and E is the elastic modulus. For deformations, energy equations and Castigliano's second theorem

$$U_f = \int_0^x \frac{{M_R}^2}{2 \cdot E \cdot I} dx \text{,} \tag{3.7}$$

$$U = \int_0^x \frac{W^2}{2 \cdot E \cdot (a \cdot b)} dx \,, \tag{3.8}$$

$$U_f = \int_0^y \frac{{M_R}^2}{2 \cdot E \cdot I} dy \,, \tag{3.9}$$

$$U = \int_0^y \frac{W^2}{2 \cdot E \cdot (a \cdot b)} dy \,, \tag{3.10}$$

$$U = \int_0^x \frac{M(\theta)^2}{2*A*E*e} dx + \int_0^x \frac{F*V(\theta)^2*R_n}{2*A*G} dx + \int_0^x \frac{N(\theta)^2*R_n}{2*A*E} dx - \int_0^x \frac{M(\theta)*V(\theta)}{A*E} dx \,, \tag{3.11}$$

$$M(\theta) = V * R_n * \sin\theta + n * R_n * (1 - \cos\theta) + M_0 \,, \tag{3.12}$$

$$V(\theta) = V * \cos\theta + n * \sin\theta \text{ , and} \tag{3.13}$$

$$N(\theta) = -n * \cos\theta + V * \sin\theta \,, \tag{3.14}$$

were used to model each subsection individually, and then combined in order to determine the total deformation [57].

Comparisons are made between von Mises Stress, von Mises Strain, and Total Deformation, which are computed with,

$$\sigma_e = \left[\frac{(\sigma_1 - \sigma_2)^2 + (\sigma_2 - \sigma_3)^2 + (\sigma_3 - \sigma_1)^2}{2}\right]^{1/2} \,, \tag{3.15}$$

$$\varepsilon_e = \frac{1}{2}\left[(\varepsilon_1 - \varepsilon_2)^2 + (\varepsilon_2 - \varepsilon_3)^2 + (\varepsilon_3 - \varepsilon_1)^2\right]^{1/2} \text{ , and} \tag{3.16}$$

$$\delta = \sqrt{\delta_x^2 + \delta_y^2 + \delta_z^2} \,, \tag{3.17}$$

where σ_1, σ_2, σ_3 are the principal normal stresses, ε_1, ε_2, ε_3, are the principal normal strains, and δ_x , δ_y , δ_z , are the deformations in the X, Y, and Z directions that are used to compute the total deformation δ [58]. Detailed computations are included in Appendix C.

To refine the FEM models, the simple AFO was physically tested using a DIC system where the top of the brace height was fully constrained. To match these boundary conditions in FEM, the surface areas in the front and back of the brace where the fixture plates and simplified AFO came into contact were fixed. To match the loads in DIC, equivalent weight applied to the selected area. The overall FEM setup can be seen in Figure 31. The fixed area has a blue label tagged with an “A” on the top of the brace height and the load is applied to the end of the foot plate with a red arrowed labeled “B”. Since the DIC could only view a section of the overall model, due to focusing, FEM needed to view the same section for a proper comparison. This was done by finding the exact distance along the bottom curve where the DIC measurements became blurry or out of focus. This distance was then applied to a cross sectional plane that was parallel to the front surface of the simplified AFO model to generate a new plane. After the new plane was created, a slice feature was applied to the new plane, splitting the model into two sections. The top section was selected and applied to directional deformation probes to match the DIC viewing section. The deformation probe can be seen in Figure 32.

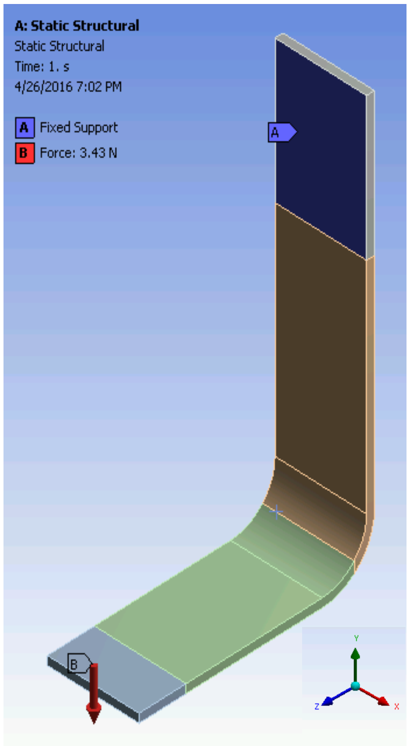

Figure 31. Boundary Conditions for Simple AFO in ANSYS.

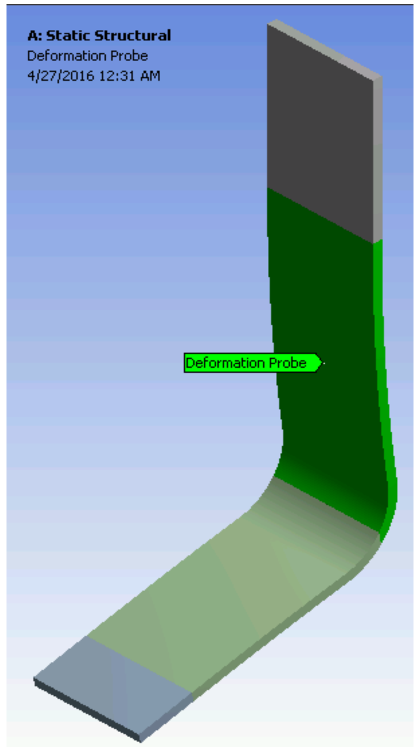

Figure 32. ANSYS Direction Deformation Probe for Data Collection.

For the standard and custom AFOs, the fixture plates did not fix the top of the brace height properly due to the curve at that section, which can be seen in Figure 33 and Figure 34, so screw holes were made for the physical testing. To match these conditions, two holes were created in the SolidWorks file for the standard and custom AFO to match the screw diameters and locations. A split line feature was then used to create a larger concentric circle around the hole to match the surface area of the screw head in contact with the AFO. For the load applied on the foot plate, a screw with a hook was drilled into the end of the foot plate where a suspended weight with a hook could be applied. A nut was then attached to the screw end to hold the screw in place. To match this load in ANSYS the same process that was used on the backplate screw holes was also applied to the footplate screw hole.

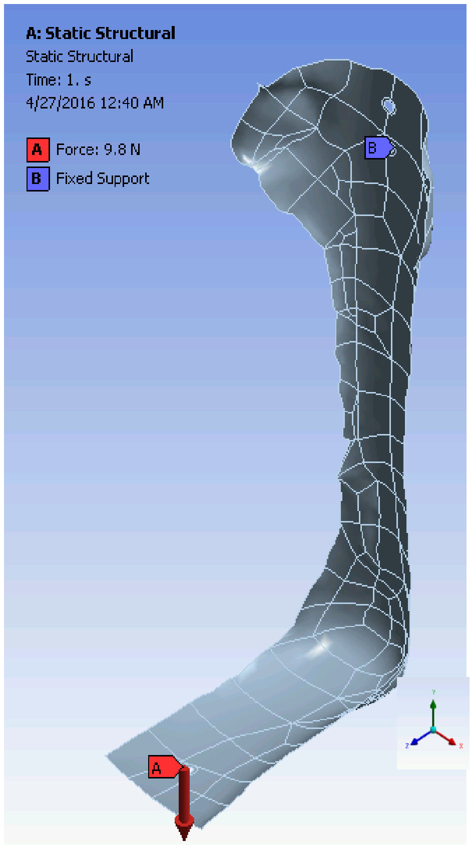

Figure 33. Boundary Conditions for Standard AFO in ANSYS.

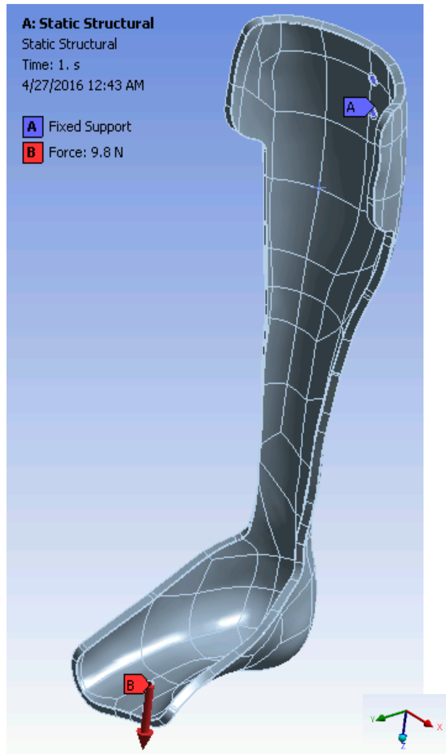

Figure 34. Boundary Conditions for Custom AFO in ANSYS.

3.3.1.5 Material Properties Validation Procedure

The custom and simplified AFOs were printed from Stratasys Direct Manufacturing with a polypropylene like material called RIGUR 450. The deformations in each direction (X, Y, and Z) were captured on both the DIC and ANSYS and were compared to validate the material properties of the part. In ANSYS, the material properties of the model were all dependent upon the Young's Modulus and Poisson's Ratio since the material the Simplified AFO and Custom AFO were additive manufactured out of a specified range for the Young's Modulus, which can be seen in Figure 35.

7	Derive from	Young's Modulus and Poisson's Ratio	
8	Young's Modulus	1700	MPa
9	Poisson's Ratio	0.3	
10	Bulk Modulus	1416.7	MPa
11	Shear Modulus	653.85	MPa

Figure 35. Material Properties Defined in ANSYS.

3.3.1.6 Buckling Analysis

Buckling analysis was a method to test the structural integrity of the model for buckling, where the model bends to the point of instability due to its response to a given load. For the buckling analysis, an already validated ANSYS model was used and the setup data for that simulation was transferred to an Eigenvalue Buckling simulation. The analysis was run to see if the AFO would buckle under the weight of the user with a safety difference of 20 pounds. Since the user weighs 180 pounds, the model needed to not buckle at 200 pounds of force. To increase the buckling load, the geometry of the Custom AFO was modified.

3.3.1.7 Geometric Validation Procedure

In order to test the accuracy of the scanning device, a simplified model, a NIST traceable gauge, and a software package, called CloudCompare [59], that directly compares point cloud files together were used. The simplified geometric representation of the AFO was scanned using the iSense. Both this STL file and an STL created from the SolidWorks model of the simple AFO were imported into CloudCompare. CloudCompare automatically created point clouds from the STL mesh files by using the vertices of the mesh surfaces. The point clouds were then moved and rotated using the tools in CloudCompare until they generally had the same location and orientation. Then, a function was used to more accurately align the two point clouds via Iterative Closest Point. This function moved one of the point clouds slightly and determined if this improved the alignment or not, and repeated this process until the change in alignment was small enough to be considered insignificant. After the alignment, a distance map was created via the Cloud to Cloud distance function and represented in a scalar field for the point cloud. Using this distance map and the raw data, the error caused by the scanner can be identified. The raw data were exported into Microsoft Excel, where a confidence interval was created to determine the upper and lower bounds of the absolute distances between points. This same process was repeated for an available NIST traceable gauge. This NIST gauge is traceable, geometrically accurate, and having well documented dimensions, allowing for a robust trustworthy calculation of error.

Since ScanTo3D was an important step in the creation process for the custom AFO, the Surface Wizard needed to be properly validated. In order to do this, the same software and process to validate the scanning device was used. Two STL files were used, the first contained an un-processed mesh, while the second contained a mesh that had been processed through the Surface Wizard and exported from SolidWorks. The two meshes were aligned using the Iterative Closest Point function. A distance map was then created to represent the error between the two meshes. The raw data from this distance map was then processed in Microsoft Excel, and a confidence interval was created to determine the upper and lower bounds of the error.

3.3.2 Additive Manufacturing

Once the Custom AFO was analyzed for buckling and deformations, the model was edited so that the values from the simulations matched the values that the Standard AFO experienced through the same simulations. When the final Custom model was created it was then sent to Stratasys Direct Manufacturing, Eden Prairie, MN, to be printed on a PolyJet 3D printer. This printer was chosen for its ability to print in a polypropylene like material. The polypropylene like material was used to match the material of the standard AFO, to which the custom was compared. Both the custom and simple AFO models were printed using the same material so that physical testing could be performed on the simple model and the material properties could be determined. Once the printed model was received it was then prepared for the non-destructive testing procedures for DIC.

3.3.3 Non-Destructive Testing with Digital Image Correlation

3.3.3.1 Experimental Planning

As a method for determining the physical testing parameters using DIC, an RSS uncertainty analysis was used with the deformation equation obtained from the analytical model to determine, which variables produce the highest amount of uncertainty. The RSS equation for uncertainty for the simplified model is,

$$\delta\delta_y = \sqrt{\begin{array}{c}\left(\frac{\partial\delta_y}{\partial L_1}\cdot\delta L_1\right)^2+\left(\frac{\partial\delta_y}{\partial L_2}\cdot\delta L_2\right)^2+\left(\frac{\partial\delta_y}{\partial L_3}\cdot\delta L_3\right)^2\\ +\left(\frac{\partial\delta_y}{\partial R}\cdot\delta R\right)^2+\left(\frac{\partial\delta_y}{\partial a}\cdot\delta a\right)^2+\left(\frac{\partial\delta_y}{\partial b}\cdot\delta b\right)^2\end{array}}. \tag{3.18}$$

By using Equation 3.18, the most sensitive variables needed to be tightly controlled to minimize the errors from the experimental setup were identified with more detailed analysis included in Appendix C.

With the determination of initial FEM boundary conditions and material properties, DIC was setup for deformation capturing in all specimens to replicate the said boundary conditions. A reference image, identical to the initial boundary conditions determined during the setup of FEM, was captured through the use of a trigger based system and compared to deformed images. The DIC system captures ranges depending on the desired area of interest and size of the specimen. Due to these aspects, the DIC setup required a particular configuration. Figure 36 represents the DIC setup for experimental mechanics. Specimen observations were carried out via two high powered CCD cameras, Photron Limited Fastcam SA-Zs, in a stereo-system setup attached on a tripod mount.

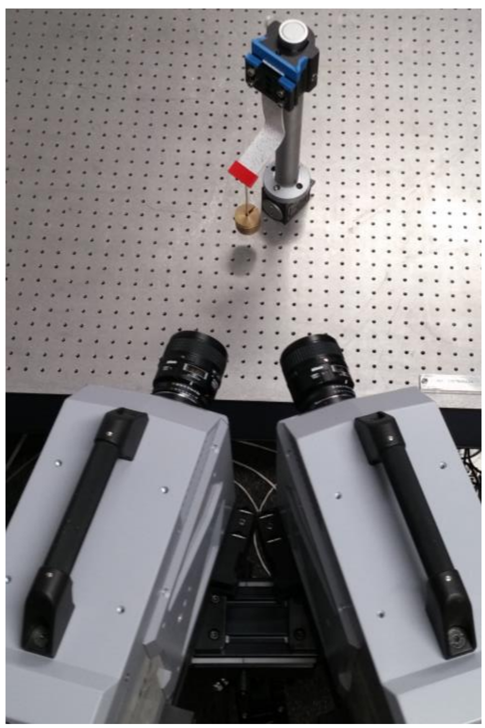

Figure 36. DIC Setup for Simplified AFO.

Each specimen was applied with a randomized speckle pattern using white matte spray paint as the base coat and black matte spray paint for the individual speckles. The speckle application was carried out in a ventilation hood to reduce buildup of hazardous fumes. Depending on the size of the desired speckle, two factors must be kept in mind: the amount of force applied to the nozzle of the spray can and the distance between the spray can and AFO. For smaller sized speckles a larger distance and moderate amount of force is required whereas the large speckle patterns require a shorter distance and minimal force, as shown in Figure 37.

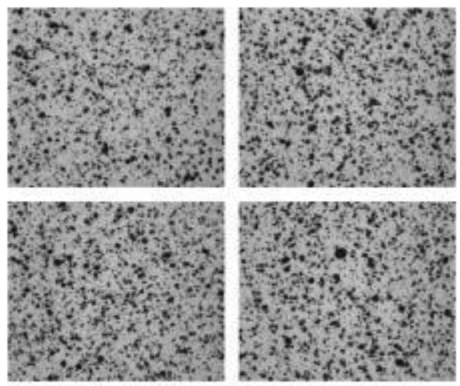

Figure 37. Sample of Speckle Patterns
Used for DIC Measurements [60].

To avoid paint accumulation on any of the AFO surfaces, spraying was completed in three sections with respect to the main sections of an AFO: the backplate, curved area, and footplate as to not alter the surface material. For the Standard and Custom AFOs, the base coat was applied over a much longer period of time in short bursts due to the high amount of curved sections. To keep a uniform speckle size it was crucial to spray in a continual motion, starting and ending away from the AFO as to not create larger than desired speckles.

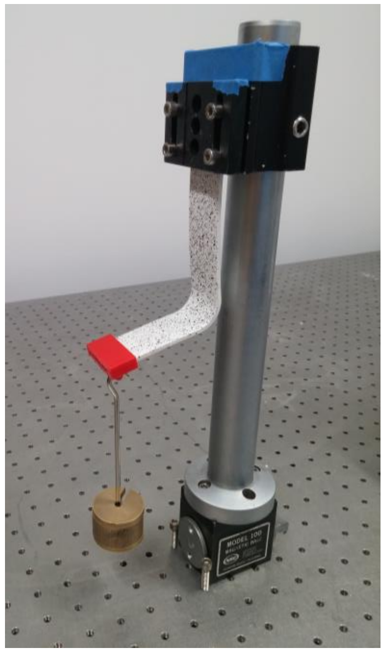

Figure 38. Simple AFO Subjected to a Static Load.

The deformed images were captured using incremental loads of 50 grams. A hook suspension platform, as shown in Figure 38, was used to add the weights in equilibrium for all of the physical testing specimens. For the simplified AFO, two optical compliant metallic fixtures were used to fix the top of the backplate. A sleeve with a hook on the bottom was printed in ABS, using an XYZ daVinci Duo 2.0, and affixed onto the end of the footplate for the hook suspension platform to be attached to. This allowed for a uniform load application across the entire foot plate of the simple AFO, as opposed to as a point load. A vibration test for the simplified AFO was carried out as a method to verify the before and after style of image capturing was accurate. For the standard and custom AFOs, the fixture plates did not work in fixing the top of the brace height due to the curved section. Instead, two screws were screwed into the center axis of the curved (calf) section, equidistant from one another, down from the top of the brace at set positions. For the applied load on the footplate a screw hole was created just before the midsection of the footplate as shown in Figure 39. The hook suspension system was then attached to an eye hook screw. An average wait time of 30 seconds was taken in account after the application of each additional weight to reduce any undesired noise from vibrations.

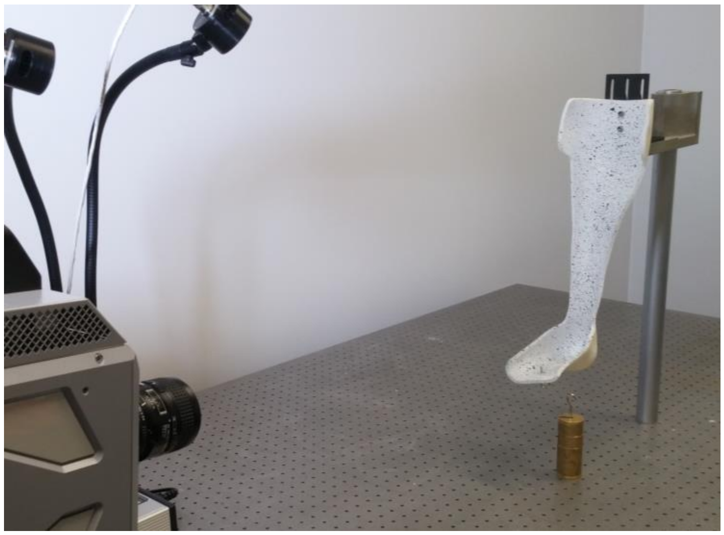

Figure 39. DIC Setup for Custom AFO.

To capture the reference images and deformed images, Figure 40, VIC Snap software from Correlated Solutions [29], was used along with the trigger based approach. Additional manufacturers with similar DIC software included GOM and Dantec Dynamics [61], [62]. Once both sets of images had been saved, calibration of the entire system was carried out using the provided calibration plates with the plate size determined by both the specimen size and speckle size. For the simplified AFO a 4mm point-to-point calibration plate was used while a 14mm plate was used for the standard and custom AFO. Both speckle images (comprised of the reference and deformed captures) and calibration images were imported into VIC-3D for analysis. VIC-3D, a shape and deformation surface measurement software by Correlated Solutions [29], allowed for the determination of an area of interest, as shown in Figure 41. The area of interest was manipulated for specific sections of the AFO and matched by the FEM as described in Section 3.3.1.

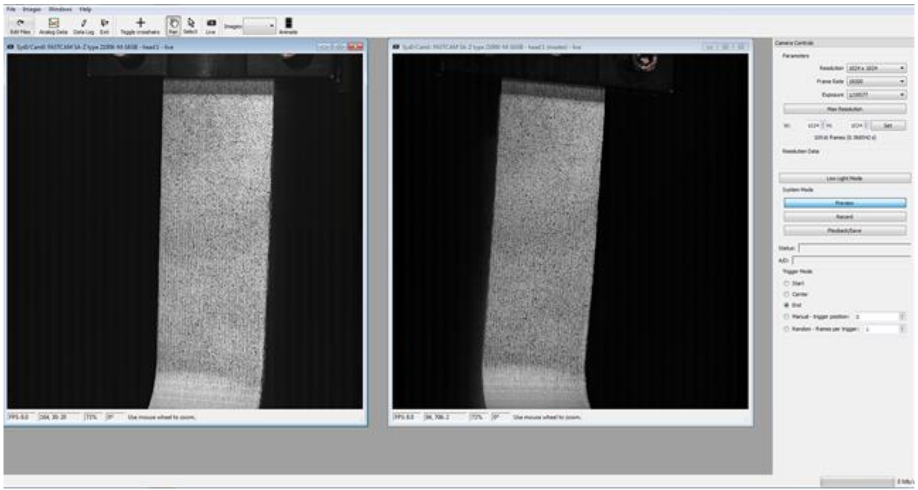

Figure 40. Stereo Images of Simplified AFO Captured with VIC Snap 8 Software.

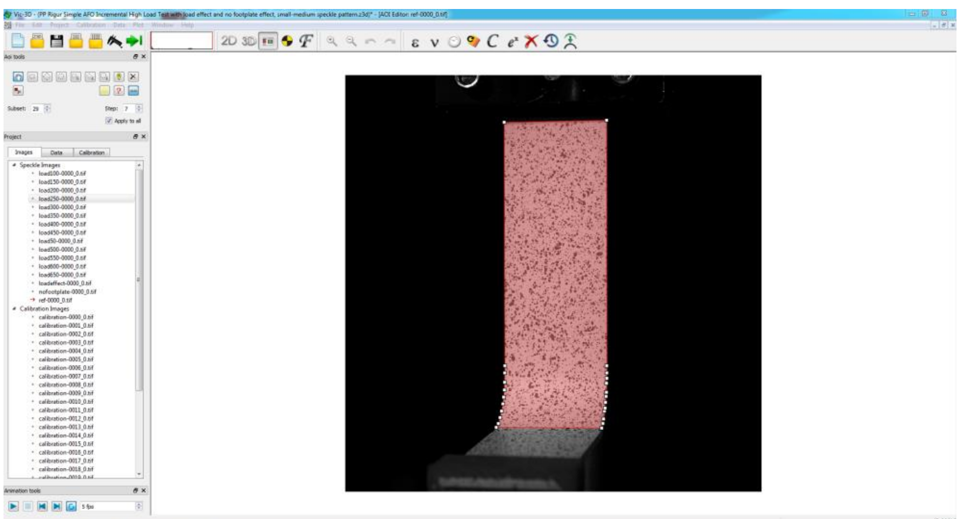

Figure 41.   Definition of Area of Interest in VIC-3D 7 Software.

4.0 Results and Analysis

The process described in the Methodology Section allowed for the creation of an AFO fit specifically to the leg of an individual. Using the iSense device, the geometry of a patient's leg is captured using the method described in Section 3.1, Full Field 3D Digitization (Scanning). This resulted in a point cloud representing the geometrical features of the patient's leg. These data were then imported into SolidWorks, where ScanTo3D is used, as described in Section 3.2, CAD Modeling Procedure for Custom AFO Generation. This results in a workable surface model of the leg. This surface model is used as the base for the remaining modeling steps further described in Section 3.2, CAD Modeling Procedure for Custom AFO Generation. The final product of this step is an initial Custom AFO. This model was then tested in FEM for its buckling load, as described in Section 3.3.6, Buckling Analysis. This allowed for the the initial Custom AFO to be optimized for performance based on the Standard AFO. This model was then fabricated using PolyJet printing technology in a Polypropylene like material. This created a physical model with the desired material properties for physical testing and fitting to the patient. Figure 42 shows the general overview of the IRP process for the development of custom orthotics.

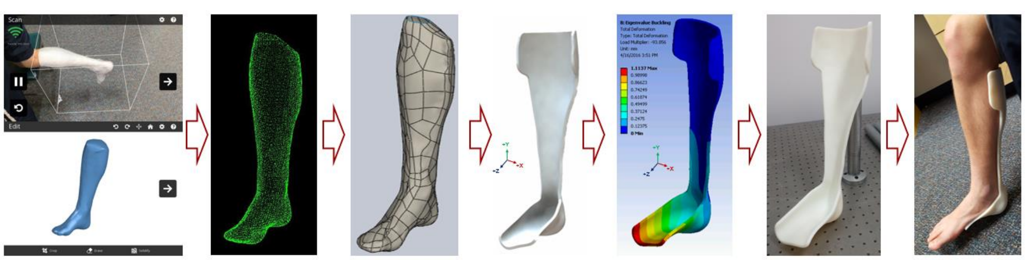

Figure 42. Integrated Rapid Prototyping for Development of Custom Orthotics. Process Follows Methodology Described in Section 3.0.

Each sub process of the IRP process was then validated individually and in terms of the overall process. In order to successfully characterize the accuracy of the scanning device and modeling procedure, a simplified AFO was created. This model consists of a straight backplate, straight footplate, and a curved heel section connecting the two straight plates. The dimensions of the simple model were known from the CAD program, and the model was manufactured in the same material, using the same process by which the Custom AFO was created. This enabled the simplified AFO model to be used to:

- Create an analytical model for comparison to and validation of FEM and determining the physical testing parameters
- Calculate the geometrical differences caused by the iSense and ScanTo3D, through point cloud comparisons
- Determine the material properties to be used in FEM, through physical testing

4.1 iSense Validation

The iSense scanner was validated using the CloudCompare software, which gave distance maps between the CAD model and iSense scan of a simplified AFO. These results enabled the characterization of the measuring accuracy of the iSense scanner. Figure 43 and Figure 44 show the absolute distances between points in μm, while Table 1 provides corresponding statistics.

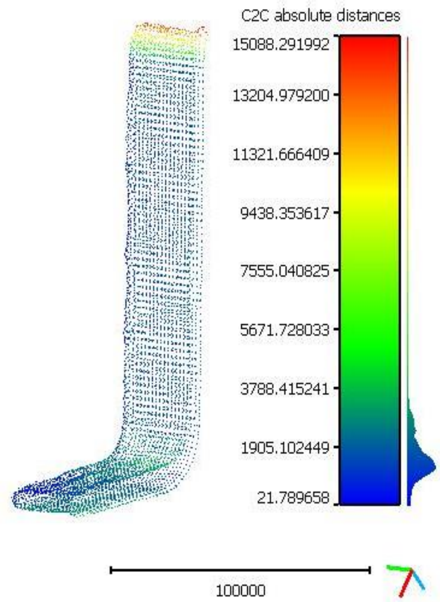

Figure 43. Absolute Distances Representing the Geometrical Differences Between CAD and iSense Measurements for Simplified AFO, μm.

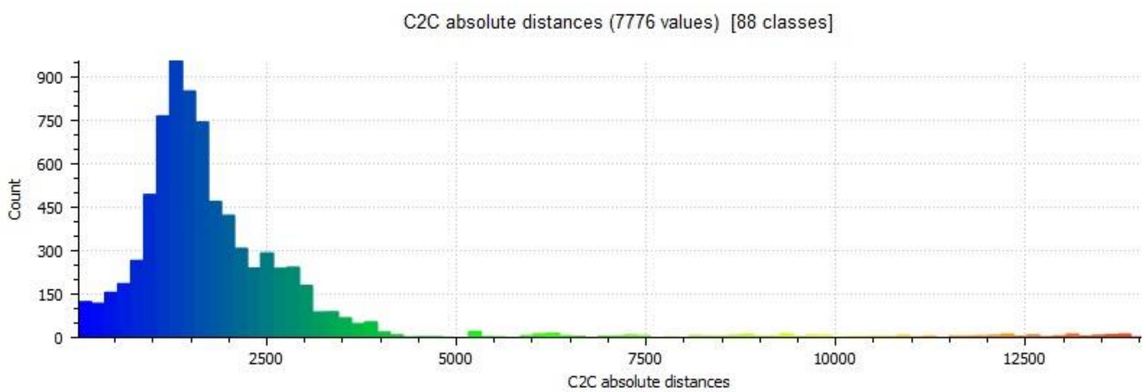

Figure 44. Histogram of Absolute Distances Obtained from Figure 42, μm.

Table 1. Summary Statistics and Confidence Interval for Simplified AFO.

Variable	Data
Mean	2021 μm
Standard Deviation	1908 μm
Z Score for 95% Confidence	5159 μm
Upper Limit	2132 μm
Lower Limit	1909 μm

From the data obtained, the error caused by the iSense scanner was determined to be between ± 2132 μm and ± 1909 with 95% confidence. However, in order to properly determine the error caused by the scanner, the error caused by the printing process must be accounted for. After measuring both the width and the thickness of the simple AFO, a 95% confidence interval was created in order to determine the approximate error caused by the printing process, the results of which are displayed in Table 2 and Table 3. From these data, the approximate error caused by the XYZ daVinci 2.0 Duo was calculated to be between 268 μm and 231 μm with 95% confidence. Therefore, the estimated error of the iSense was determined to be between ± 1864 μm and ± 1678 μm.

Table 2. Summary Statistics and Confidence Interval for Printed Part Width.

Variable	Data
Mean Width Error	250 μm
Standard Deviation for Width	111 μm
Z Score for 95% Confidence	432 μm
Upper Bound for Error using Width	268 μm
Lower Bound for Error using Width	231 μm

Table 3. Summary Statistics and Confidence Interval Printed for Part Thickness.

Variable	Data
Mean Thickness Error	256 µm
Standard Deviation for Thickness	51 µm
Z Score for 95% Confidence	340 µm
Upper Bound for Error using Thickness	263 µm
Lower Bound for Error using Thickness	250 µm

As an additional step for verification of accuracy, the same scanning procedure was applied to a NIST traceable gauge, as shown in Figure 45 and Figure 46. Figure 45 shows a distance map displaying the absolute distances as well as the actual NIST gauge utilized. Figure 46, shows the corresponding histogram of absolute distances.

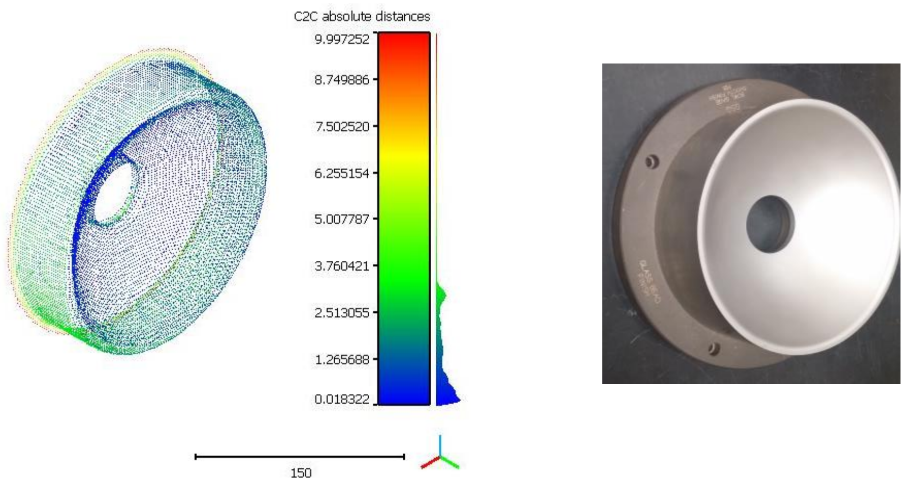

Figure 45. Absolute Distances Representing the Geometrical Differences Between CAD and iSense Measurements for NIST Gauge, mm. Actual Scanned NIST Gauge is shown.

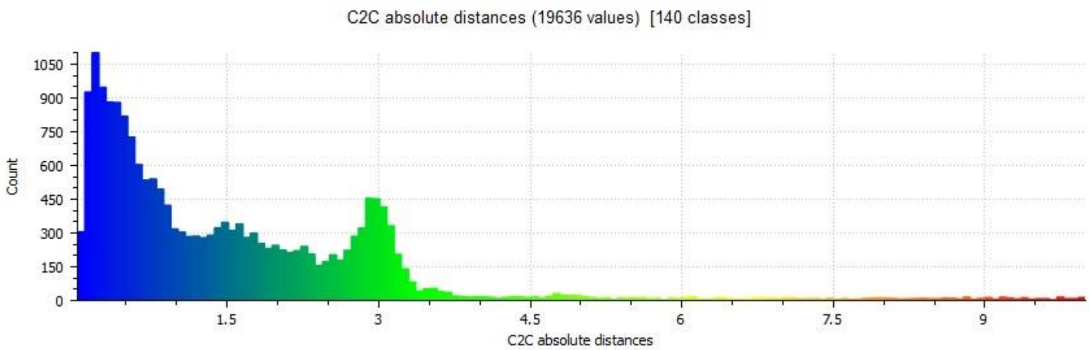

Figure 46. Absolute Distance Histogram for NIST Gauge, mm.

Table 4. Summary Statistics and Confidence Interval for NSIT Gauge.

Variable	Data
Mean	1284 µm
Standard Deviation	1001 µm
Z Score for 95% Confidence	2931 µm
Upper Bound for Error	1306 µm
Lower Bound for Error	1262 µm

The data gathered from the distance map was then used to calculate the mean and standard deviation of the sample, presented in Table 4. From these summary statistics the error was estimated to be to between ± 1306 µm and ± 1262 µm, a reduction from the previous estimate. This provides a better approximation of the error that would be experienced while scanning a patient's leg, due to the curvature of the gauge and the closer size approximation

The error in the scanning process was believed to be caused by issues including size of the object being scanned, lighting in the area where the scan is performed, and the general quality of the scanner. For this case study, the iSense device was determined to be sufficient, due to its low cost, portability, ease of use, and relatively high accuracy. While the error caused by the scanner is on the order of 1.25 mm, this error compared to a human leg is relatively small

4.2 ScanTo3D Validation

The following set of Figures displays the data gathered for the medium surface detail option. This option was used to create an accurate model while still being time efficient. The results from the low and high surface detail options can be found in Appendix D. Figure 47 displays the distance map of absolute distances. Figure 48 displays the histogram of absolute distances absolute.

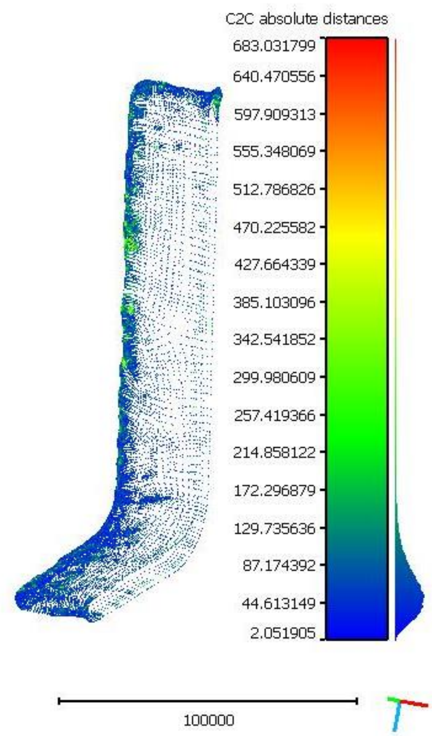

Figure 47. Absolute Distances Representing the Geometrical Differences Between iSense Data Cloud and ScanTo3D Models for Simplified AFO, μm. Distances Determined using a ScanTo3D Model Defined by Medium Surface Detail.

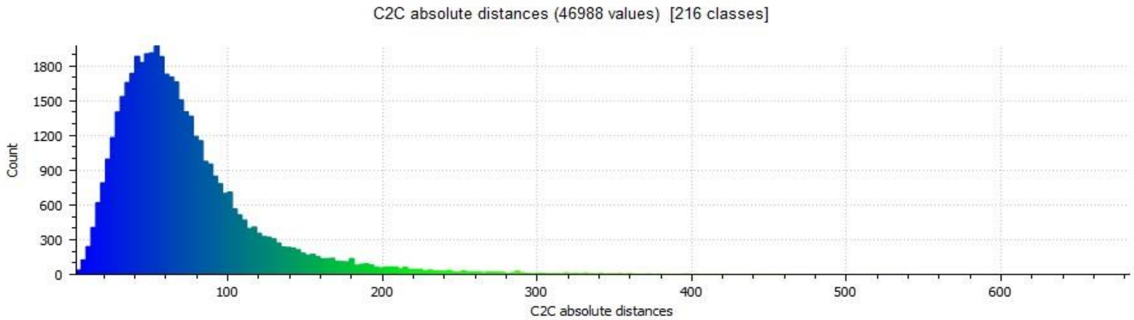

Figure 48. Histogram of Absolute Distances Obtained from Figure 46, µm.

Table 5. Summary Statistic and Confidence Interval for Medium Surface Detail.

Variable	Data
Mean	72 µm
Standard Deviation	50 µm
Z Score for 95% Confidence	155 µm
Upper Bound for Error	109 µm
Lower Bound for Error	37 µm

Using the data gathered from this test, the summary statistics shown in Table 5 were calculated. The error caused by ScanTo3D, when using the medium surface detail option, was between ± 109 µm to 37 µm which can be stated with 95% confidence. In addition, the main source of error occurs in the rounded sections of the scan, near the edge of the simplified AFO. The error caused by this setting is significantly low in comparison to both the manufacturing and the scanning processes. For this reason, using the medium level surface detail option is good balance between geometric accuracy and computational demand.

4.3 FEM and Analytical Models

Following the methods outlined in the Methodology Section, equivalent analytical and computational models were created. Table 6 shows the comparisons of the results, which shows a maximum difference between modeling and analysis of less than 2.5%. This difference indicates that the analytical and computational models can be reliably used together with physical testing by DIC.

Table 6. Comparison Results of Mathematical Model and FEM.

Variables	Mathematical Model Results	FEM Results	Percent Difference
Max Stress, MPa	4.239	4.18	1.39%
Max Strain (von Mises)	0.002	0.00178	1.40%
Max Deformations, mm	31.9	32.6	2.11%

4.4 Comparisons between Simulation and Physical Testing

4.4.1 FEM and DIC for the Simplified AFO

To verify the material properties of the Custom AFO, the directional deformations of the DIC and ANSYS results were compared. The Young's modulus and Poisson's Ratio were adjusted in the FEM model within the range provided by the manufacturer, Stratsys, until the results matched as closely as possible. The Simplified AFO results for the directional deformations in ANSYS and DIC are reported in Table 7 as well as in Figure 49 and Figure 50.

Table 7. Comparison of Directional Deformation Results for FEM and DIC.

Load, grams	DIC δ_X, mm	DIC δ_Y, mm	DIC δ_Z, mm	FEA δ_X, mm	FEA δ_Y, mm	FEA δ_Z, mm
50	0.0133	0.304	2.3	0.00848	0.356	2.39
100	0.0136	0.304	2.32	0.0127	0.534	3.59
150	0.0238	0.665	5.29	0.0169	0.711	4.78
200	0.0234	0.815	6.55	0.0211	0.890	5.98
250	0.0282	0.96	7.95	0.0254	1.07	7.17
300	0.0344	1.09	9.2	0.0296	1.25	8.37
350	0.0372	1.205	10.5	0.0339	1.42	9.57
400	0.0386	1.215	10.5	0.0381	1.60	10.8
450	0.047	1.4	12.6	0.0423	1.78	11.9
500	0.0495	1.49	13.6	0.0466	1.96	13.2
550	0.051	1.57	14.6	0.0509	2.14	14.3
600	0.0555	1.63	15.4	0.0551	2.31	15.5
650	0.0595	1.68	16.2	0.0593	2.49	16.7

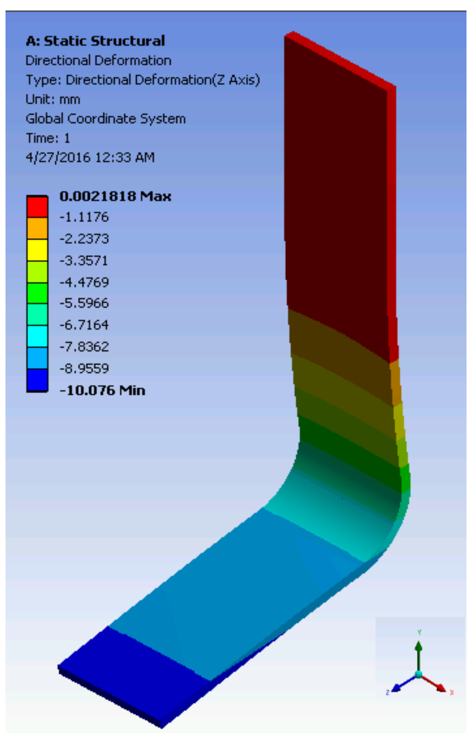

Figure 49. Representative FEM Results for Deformations in the Z Direction.

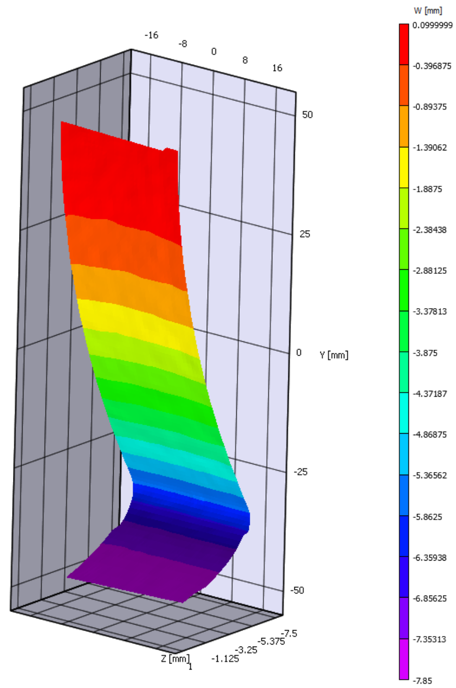

Figure 50. Representative DIC Results for Deformations in the Z Direction.

As shown in Figure 51, Figure 52, and Figure 53, the maximum computational and experimental deformations for the simplified AFO model are compared in each direction.

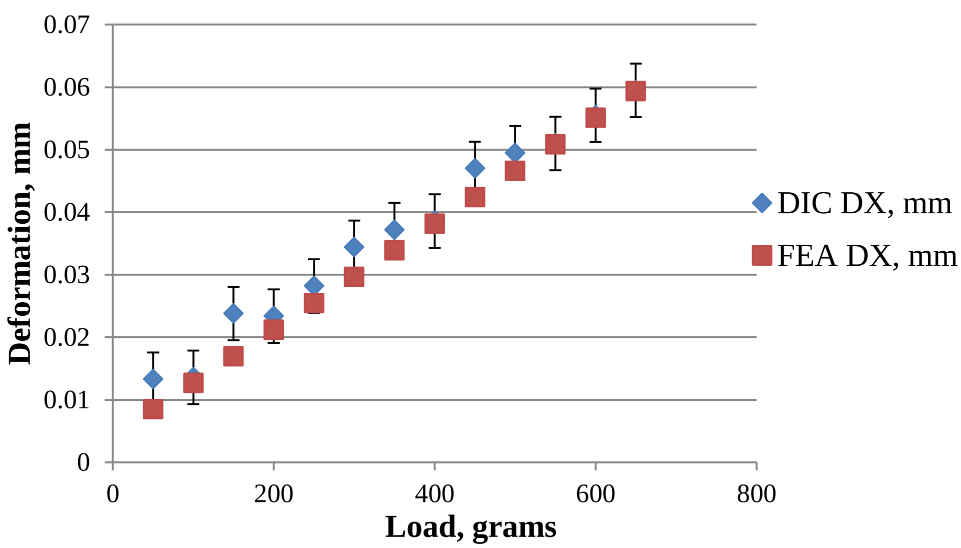

Figure 51. Deformation in X-Direction over Loads for FEM and DIC.

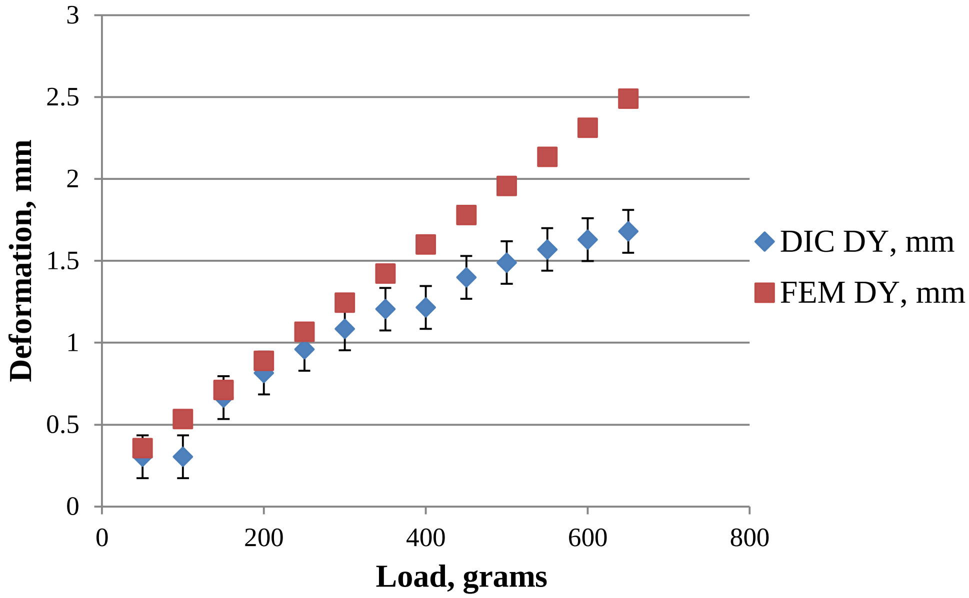

Figure 52. Deformation in Y-Direction over Loads for FEM and DIC.
Linear Elastic FEM Model Predicts Deformations Correctly for Small Loads.

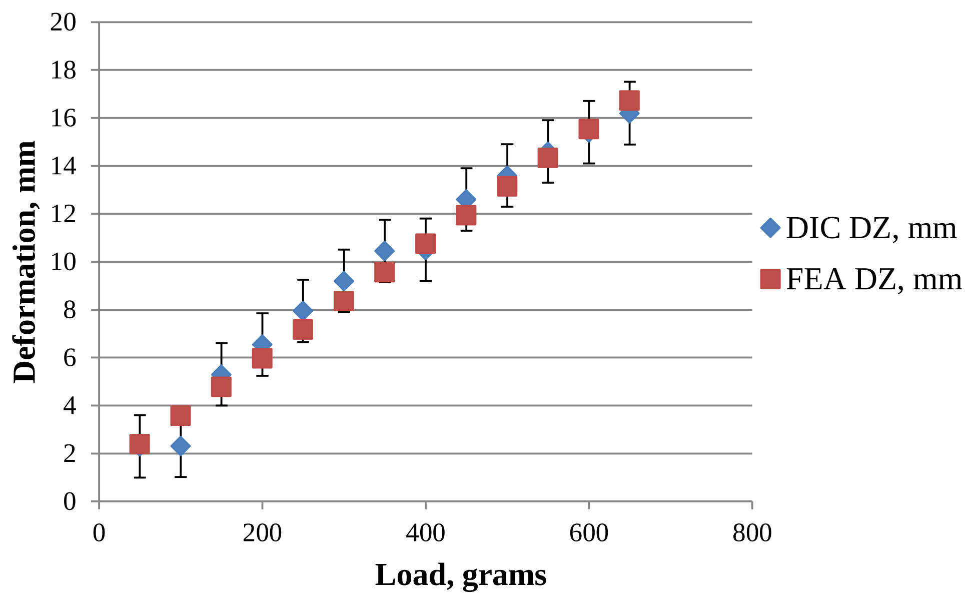

Figure 53. Deformation in Z-Direction over Loads for FEM and DIC.

For the deformations in the X direction, in the plane of the foot plate towards the cameras, and Z direction, in the plane of the foot plate perpendicular to the cameras, both the FEM and DIC measurements followed a linear profile. However, in the Y direction, or the direction in line with the backplate, the DIC results began to follow a nonlinear, logarithmic profile as shown in Figure 52. This is believed to be caused by the material of the AFO, as well as the additive manufacturing process. Due to this process, the material is not isotropic, instead there are small layers built on top of one another. This can cause the material to behave in different ways for different directions, as seen in the data. Another likely cause for this would be due to the nonlinearity of the material. By design, the device was made from a polypropylene like material. Polypropylene, being a plastic, does not follow the standard linear stress strain curve. Therefore, since this material was made to simulate polypropylene, it can be assumed that it will also follow this nonlinearity in terms of stress and strain. To this effect, the FEM model created during this project is only valid for small deformations. In those cases, the material still follows the linear profile of stress and strain and therefore, the model holds. If it is desired to model this material for higher loads, it would be necessary to determine the mathematical relationship that would properly model the changing Young's Modulus of the material. From these data, it was discovered that the material used to manufacture both the simple AFO and Custom AFO had a Young's Modulus of 1700 MPa and Poisson's Ratio of 0.3.

4.4.2 Buckling Analysis of Standard AFO

The Eigenvalues that were obtained by FEM buckling analysis were utilized together with a multiplier to determine the actual buckling load, $F_{buckling}$, with

$$F_{Buckling} = \lambda \cdot F_{initial} \quad , \tag{4.1}$$

where $F_{initial}$ is the normalized Eigenvalue and λ is the load multiplier. This procedure was applied to two different Standard AFO models. The first model was from a 3D scan of the

Standard AFO, from which it was later discovered that there was a thickness error occurring from the 3D scan. Therefore, a second model was created by only scanning the inner surface of the Standard AFO and performing FEM by using shell elements with an average thickness that was measured with a digital micrometer. The results from both analyses for the buckling load are in Table 8, while the buckling load for the FEM model using shell elements is shown in Figure 54.

Table 8. Standard AFO Buckling Loads Determined from FEM.

Standard AFO	Load Multiplier (λ)	Initial Load, N	Buckling Load, N
Thick (Full Scan using solid elements)	102.92	9.8	1008.62
Thin (Surface Scan using shell elements)	1.5583	9.8	15.27134

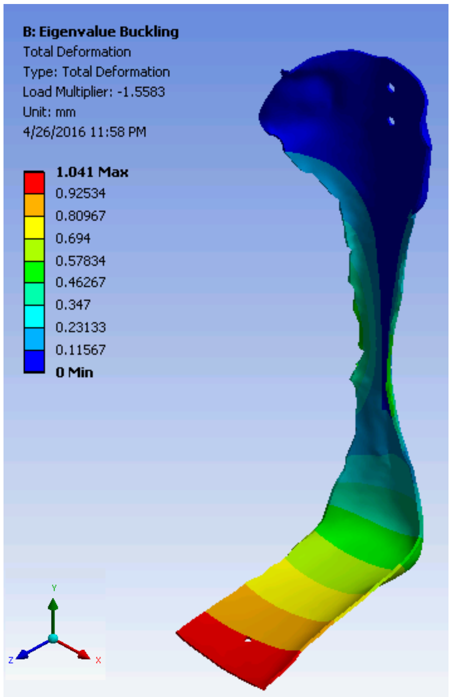

Figure 54. Buckling Mode of a Standard AFO Obtained by FEM with Shell Elements. Analysis Provides Buckling Load and Mode.

4.4.3 FEM and DIC for the Standard AFO

The DIC camera has a limited field of view, which causes only sections of interest to be viewed on the AFO. To address the limited field of view of the DIC system, only the desired sections of interest were selected in ANSYS to be viewed. This was done by selecting the surfaces within the field of view and applying directional deformation probes to view only that particular section. The Standard AFO results for the directional deformations in ANSYS and DIC are shown in Table 9 and Figure 55.

Table 9. Comparisons of Deformations between DIC and FEM for a Standard AFO.

Weight : 3.43 N			
Young's Modulus = 2,275 MPa			Poisson Ratio = 0.3
Deformation	FEM	DIC	Percent Difference
DX	0.176	0.13	35.6%
DY	0.664	0.6	10.6%
DZ	4.91	5.5	10.8%

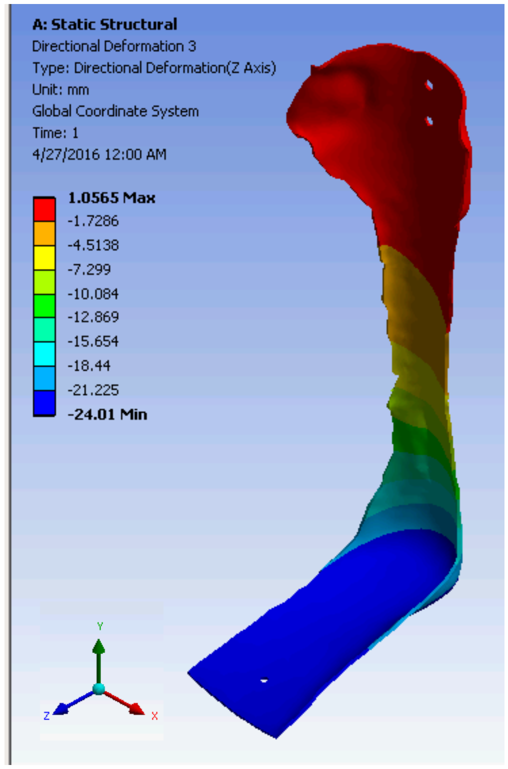

Figure 55. Deformations in the Z-Direction Obtained with FEM for a Standard AFO.

4.4.4 Buckling Analysis of Custom AFO

Similar to the Standard AFO analysis, the Eigenvalues that were obtained by FEM buckling analysis were utilized together with a multiplier to determine the actual buckling load of the Custom AFO. This load was also utilized to develop the Custom AFO with a performance similar to that of the Standard AFO. To be able to compare FEM buckling analyses results with the Standard AFO, two different buckling analyses were conducted on the Custom AFO.

The first Custom model using solid elements was compared to the Standard AFO FEM buckling analysis using solid elements. Attempting to match the custom and standard buckling loads, a very thick Custom AFO model was produced which can be seen in Table

10 and Figure 56. The second Custom model using solid elements was compared to the Standard AFO FEM buckling analysis using shell elements.

Table 10. Standard and Custom AFO Buckling Loads Determined from FEM.

AFO	Load Multiplier λ	Initial Load, N	Buckling Load, N
Standard Thick (solid elements)	102.92	9.8	1008.62
Custom Thick (solid elements)	93.86	9.8	919.79
Standard Thin (shell elements)	1.56	9.8	15.27
Custom Thin (solid elements)	1.44	9.8	14.13

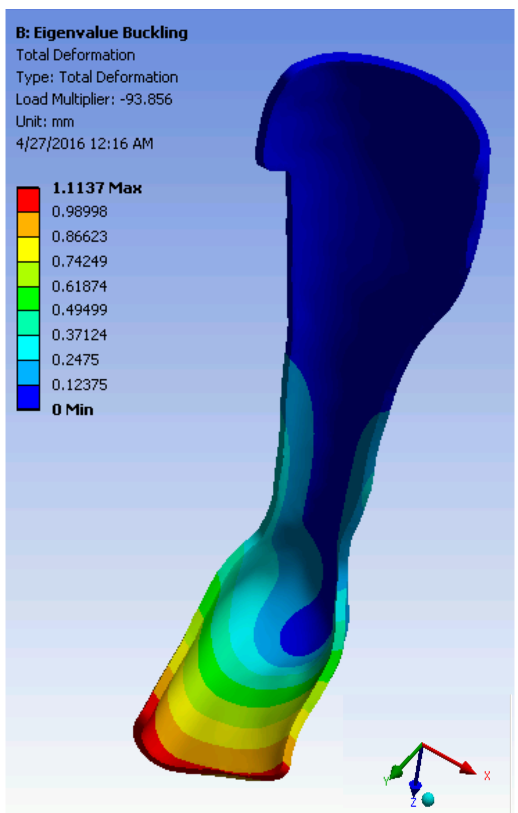

Figure 56. Buckling Analysis of Custom AFO.
Analysis Provides Buckling Load and Mode.

4.4.5 FEM and DIC for the Custom AFO

To match the view of the DIC to the results collected by FEM, the desired surfaces on the standard AFO FEM model were selected and had directional deformation probes applied. For the custom AFO, a new cross sectional plane is created that goes up half of the AFO. After the new plane was created, a slice feature was applied to the new plane, splitting the model into two sections, top and bottom. The bottom section was selected and applied to directional deformation probes to match the angled DIC viewing section. Directional deformation probes were then applied to the bottom half of the AFO so that only that section was viewed. The Custom AFO results for the directional deformations in FEM and DIC were compared and are shown in Table 11 and Figure 57.

Table 11. Comparisons of Deformations between DIC and FEM for a Custom AFO.

Weight, grams	DIC δ_Y, mm	DIC δ_Z, mm	FEA δ_Y, mm	FEA δ_Z, mm	Percent Difference δ_Y	Percent Difference δ_Z
257.5	0.59	0.925	0.524735	0.753754	11.1%	18.5%
307.5	0.6	1.11	0.626626	0.90011	4.44%	18.9%
357.5	0.89	1.34	0.728516	1.046466	18.1%	21.9%
407.5	0.895	1.34	0.830407	1.192873	7.22%	10.9%
457.5	1.1	1.39	0.9323	1.339199	15.3%	3.65%

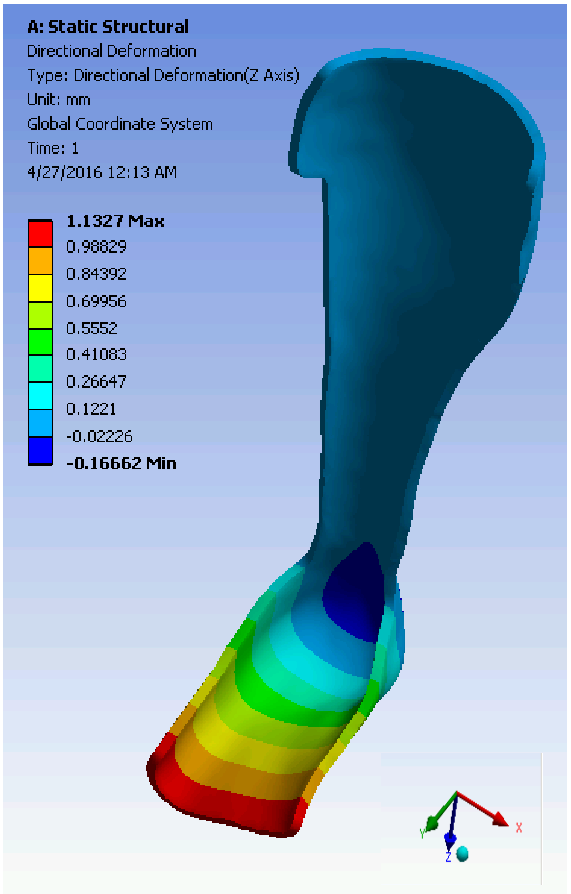

Figure 57. Deformations in the Z-Direction Obtained with FEM for Custom AFO.

5.0 Conclusions

5.1 Scanning

The iSense was found to work well at capturing the geometry of a person's leg but did not perform well when trying to scan an object with small thickness. When the iSense tried to scan thin-walled objects, such as the standard AFO model, the iSense would end up giving a scan that had excess thickness near the thin wall. Also there were some issues with the way the object being scanned was positioned so that the largest amount could be scanned and not as many holes occurred from the object touching the ground. The scan from the iSense also needed to be fairly complete as any sort of missing data would cause problems when importing to SolidWorks.

5.2 Modeling

The modeling process examined here worked well for creating a custom fit orthotic device. However, incomplete data imported from the iSense caused issues. In these areas, ScanTo3D created surfaces that intersected themselves, or did not accurately fit to the meshes. In spite of this, the use of ScanTo3D, even with the lowest setting for surface detail, produced surface models of the leg with a higher fidelity than the 3D scans.

5.3 Simulation

The comparisons between the analytical model and the FEM simulations produced errors less than 2.5%, which were suitable for the IRP process. The characterization of material properties indicated that their values are well within those specified by RIGUR 450 Young's modulus range, as reported by Stratasys Inc. The difference for the

Simplified AFO between the DIC and FEM were approximately 10% for directional deformation with the proper material properties. The comparisons between DIC and FEM for the custom AFO suggests, based on the errors determined, that additional investigations are needed.

5.4 Physical Testing

Non-destructive testing using digital image correlation was determined to be an accurate optical method for shape and deformation measurement as determined by the comparisons with the FEM modeling. For the simplified AFO, DIC gave good representations of the material properties and simulated models. However, for the standard and custom AFO, issues were experienced when capturing the entirety of the AFO as a result of the AFO sizes, camera to object distance, tilt angle of the cameras, and focal length.

6.0 Recommendations and Future Work

The overall implementation of the Integrated Rapid Prototyping process towards custom orthotic devices was demonstrated. There are, however, several approaches that could be done to optimize the entirety of the process. These approaches involve: improvement in data acquisition of 3D digitization, definition of parametric CAD models to enable fast customization, refinement of FEM and material models, process automation, and shape and topology optimization.

The iSense device, while accurate enough for this purpose, still contributes the majority of the errors to the overall process. It is suggested that ideal scanning conditions be determined and variables like speed of scan, distance to object being scanned, and relative size of scanning volume to object be tested for and optimized. In addition, the current method of capturing the full leg scan needed for modeling works well, however, for applications for those patients who may suffer from foot drop, a higher rate of acquisition for scanning and a different pose may be required. This is due to the way the leg is positioned off of the chair which a person experiencing foot drop may be unable to keep their foot straight to the degree needed for the duration of the scan. One way to improve this pose could be to use a clear glass or plastic table that the person could stand on as the iSense is unable to scan clear objects. The iSense would scan through the table and the sole of the foot would be captured as it is in contact with the ground, which could provide better comfort for the custom AFO. Finally, while the iSense device may have been acceptable for this application, it may not be for all. If higher accuracies are needed for a particular application, other scanning devices must be researched.

Modeling of the customized AFO was carried out using a single process. This process was effective in creating an orthotic that successfully matched the outer surface of the calf, however, the current procedure does not allow for certain patient specific needs to be met, like custom support for plantarflexion. The current procedure for creating the custom orthotic takes a long time and a person with CAD experience to create. Some initial research went into looking at using MATLAB for an automated process of creating an orthotic. This automated process would take the scanned object and be able to create a custom orthotic based on the scan with minimal influence from the operator.

As discussed earlier, it was determined that the material used for the manufacturing of the custom orthotic did not follow a linear elastic stress strain curve. This limited the analysis done for small deformations. In order to fully model this device, a mathematical model that represented the nonlinear geometric stress strain curve must be created for proper modeling of the material.

A future method for the creation of a custom AFO would be optimization of the shape and topology of the orthotic. An examination into process optimization could improve the overall cost of manufacturing, time for manufacturing, and performance of the custom orthotic through material reduction and addition.

References

[1] Gao, W., Zhang, Y., Ramanujan, D., Ramani, K., Chen, Y., Williams, C. B., Wang, C. C. L., Shin, Y. C., Zhang, S., and Zavattieri, P. D., 2015, "The status, challenges, and future of additive manufacturing in engineering," Computer-Aided Design, 69, pp. 65-89. http://ac.els-cdn.com/S0010448515000469/1-s2.0-S0010448515000469-main.pdf?_tid=fac195b6-098d-11e6-82c1-00000aab0f01&acdnat=1461441788_279537b70dc5d57d8f60fd1765bf234d

[2] Dúbravčík, M., and Kender, Š., 2012, "Application of Reverse Engineering Techniques in Mechanics System Services," Procedia Engineering, 48, pp. 96-104. http://www.sciencedirect.com/science/article/pii/S1877705812045547

[3] Peng, Q., and Sanchez, H., "3D Digitizing Technology in Product Reverse Design", University of Manitoba, Winnipeg, Manitoba, Canada.

[4] An Overview on 3D Printing. https://books.google.com/books?id=baKSCgAAQBAJ&pg=PA32&lpg=PA32&dq=non-contact+passive+scanning&source=bl&ots=3l9hel8aCd&sig=v_u1Zs3LDFQaKHFObAboQO6XgIY&hl=en&sa=X&ved=0ahUKEwjJ_oLNl6vMAhWLFT4KHb13AQ84FBDoAQgyMAQ#v=onepage&q=non-contact%20passive%20scanning&f=false

[5] Yu, F., Lu, Z., Luo, H., and Wang, P., 2011, Three-Dimensional Model Analysis and Processing, Springer Berlin Heidelberg. https://books.google.com/books?id=oJCe8E5BnWoC&pg=PA18&lpg=PA18&dq=silhouette+passive+non-contact&source=bl&ots=WGHdPPqFzY&sig=F8HCoS_H60DGowrvIq_YzP7YxM0&hl=en&sa=X&ved=0ahUKEwish_qSt6vMAhXMVT4KHcDsD70Q6AEINzAE#v=onepage&q=silhouette%20passive%20non-contact&f=false

[6] Zervas, M. J., 2011, *Development of a High Speed, Robust System for Full Field-of-View 3D Shape Measurements*, MS Thesis, Worcester Polytechnic Institute, Worcester, MA.

[7] Bi, Z. M., and Wang, L., 2010, "Advances in 3D data acquisition and processing for industrial applications," Robotics and Computer-Integrated Manufacturing, 26(5), pp. 403-413. http://ac.els-cdn.com/S073658451000013X/1-s2.0-S073658451000013X-main.pdf?_tid=f684138a-0b44-11e6-b23b-00000aacb35e&acdnat=1461630330_0abafcfd5f50e176c1239fd44f1d270a

[8] O'Grady, S., "3D Scanning," University of Michigan. http://um3d.dc.umich.edu/wp-content/uploads/2015/10/3D-Scanning-Novice.pdf

[9] Dassault Systems, 2016, “3D CAD Capabilities,” from http://www.solidworks.com/sw/products/3d-cad/capabilities.htm

[10] Inventor, 2016, "Mechanical design is more than parametric modeling." http://www.autodesk.com/products/inventor/overview

[11] Creo, 2016, "The Industry’s Leading 3D CAD Software," http://www.ptc.com/cad/creo

[12] AutoDesk, 2015, "To Convert a Mesh Object to a 3D Solid," https://knowledge.autodesk.com/support/autocad/learn-explore/caas/CloudHelp/cloudhelp/2016/ENU/AutoCAD-Core/files/GUID-45E37A82-3175-4F20-A5F7-316C46DBEBBB-htm.html.

[13] Geomagic, 2016, "Geomagic Design X," from http://www.geomagic.com/en/products-landing-pages/designx/.

[14] Berman, B., 2012, "3-D printing: The new industrial revolution," Business horizons, 55(2), pp. 155-162.

[15] Wong, K. V., and Hernandez, A., 2012, "A review of additive manufacturing," ISRN Mechanical Engineering, 2012.

[16] Simpson, T. W., 2015, "AM Needs MEs," Mechanical Engineering, 137(8), p. 30.

[17] Eyers, D., and Dotchev, K., 2010, "Technology review for mass customization using rapid manufacturing," Assembly Automation, 30(1), pp. 39-46.

[18] Ventola, C. L., 2014, "Medical applications for 3D printing: current and projected uses," PT, 39(10), pp. 704-711.

[19] Liu, Q., Leu, M. C., and Schmitt, S. M., 2006, "Rapid prototyping in dentistry: technology and application," The international journal of advanced manufacturing technology, 29(3-4), pp. 317-335.

[20] Zou D, H. T., Dailey M, Smith KE, Silva MJ, Sinacore DR, Mueller MJ, Hastings MK, 2014, "Experimental and computational analysis of composite ankle-foot orthosis," J Rehabil Res Dev., 51(10), pp. 1525-1536.

[21] Ramsey, J. A., 2011, "Development of a method for fabricating polypropylene non-articulated dorsiflexion assist ankle foot orthoses with predetermined stiffness," Prosthetics and Orthotics International, 35(1), pp. 54-69.

[22] ANSYS, 2016, "ANSYS Mechanical Enterprise," http://www.ansys.com/Products/Structures/ANSYS-Mechanical-Enterprise.

[23] Simulia, 2016, "Abaqus Unified FEA," http://www.3ds.com/products-services/simulia/products/abaqus/.

[24] Comsol, 2016, "Multiphysics Software Product Suite," https://www.comsol.com/products.

[25] Pan, B., Yu, L. P., and Wu, D. F., "High-Accuracy 2D Digital Image Correlation Measurements with Bilateral Telecentric Lenses: Error Analysis and Experimental Verification,"Exp. Mech.

[26] Pan, B., and Wang, Q., 2013, "Single-Camera Microscopic Stereo Digital Image Correlation Using a Diffraction Grating," Optical Society of America Publishing, Applied Optics.

[27] D. Lecompte, S. B., S. Cooreman, H. Sol, J. Vantomme, 2007, "Study and generation of optimal speckle patterns for DIC," SEM Annual Conference & Exposition on Experimental and Applied Mechanics, Society for Experimental Mechanics, Springfield, Massachusetts. http://sem-proceedings.com/07s/sem.org-2007-SEM-Ann-Conf-s73p01-Study-Generation-Optimal-Speckle-Patterns-DIC.pdf

[28] Hung, P.-C., and Voloshin, A. S., 2003, "In-plane strain measurement by digital image correlation," Journal of the Brazilian Society of Mechanical Sciences and Engineering, 25, pp. 215-221. http://www.scielo.br/pdf/jbsmse/v25n3/a01v25n3

[29] Correlated Solutions, Inc., "CSI Application Note AN-525 Speckle Pattern Fundamentals." https://melab.wikischolars.columbia.edu/file/view/AN525+-+Speckle+Pattern+Fundamentals.pdf

[30] Yoneyama, S., "Experimental Mechanics - Digital Image Correlation," G. Murasawa, ed., Encyclopedia of Life Systems. http://www.eolss.net/sample-chapters/c05/e6-194-04.pdf

[31] Thomas, D. Q., "Muscles of the Ankle and Foot," Illnois University. http://www.castonline.ilstu.edu/Thomas/181/Muscles%20of%20the%20Foot%20and%20ankle.pdf

[32] Martensen, K. M., 2011, "CT Dictionary," University of Iowa. https://wiki.uiowa.edu/display/881886/CT+Dictionary

[33] Catlin, B., 2008, "Basic Human Anatomy," Chapter 17: The Ankle and Foot, O'Rahilly, ed., Dartmouth Medical School. https://www.dartmouth.edu/~humananatomy/figures/chapter_17/17-6.html

[34] J. Perry, Gait Analysis: Normal and Pathological Function. Thorofare, NJ: SLACK, 1992.

[35] Catlin, B., 2008, "Basic Human Anatomy," Chapter 18: Posture and locomotion, O'Rahilly, ed., Dartmouth Medical School. https://www.dartmouth.edu/~humananatomy/part_3/chapter_18.html

[36] "Gait," Physiopedia. http://www.physio-pedia.com/Gait

[37] "UNIT IX - Walking & Locomotion: Integrating the Functions of the Lower Body," http://www.courses.vcu.edu/DANC291-003/unit_9.htm.

[38] Mooney, J., "Midstance," Illustrated Dictionary of Podiatry and Foot Science by Jean Mooney, S.V.

[39] P.J., N., 2009, "Gait," Mosby, St. Louis, MO. http://www.mccc.edu/~behrensb/documents/210wk5NormalGait_000.pdf

[40] Perry, J., "Atlas of Limb Prosthetics: Surgical, Prosthetic, and Rehabilitation Principles," Chapter 13 - Atlas of Limb Prosthetics: Surgical, Prosthetic, and Rehabilitation Principles. Digital Resource Foundation for the Orthotics & Prosthetics Community. http://www.oandplibrary.org/alp/chap13-01.asp

[41] Dreeben-Irimia, O., 2010, Introduction to Physical Therapy for Physical Therapist Assistants, Jones & Bartlett Learning.

[42] Whittle, M. W., 2007, Gait Analysis An Introduction, Butterworth Heinemann Elsevier. https://docs.google.com/file/d/0B_x2bySFA5k1eTg1WE9ZRGhleTA/edit

[43] Magee, D. J., 2008, Orthopedic Physical Assessment, Saunders Elsevier.

[44] 2008, "Foot Drop," University of Minnesota. http://www.tc.umn.edu/~chris143/Knee%20Replacement/

[45] Castillo, A., 2016, "AFO Foot Support," The Ocean Side. http://oceansidepost.com/2016/01/26/afo-foot-support.html

[46] Liaison, O. o. C. a. P., 2009, "NINDS Foot Drop Information Page," National Institute of Neurological Disorders and Stroke, Bethesda, MD 20892. http://www.ninds.nih.gov/disorders/foot_drop/foot_drop.htm

[47] Hoyle, Brian. "Foot Drop." Gale Encyclopedia of Neurological Disorders. 2005. Encyclopedia.com. 5 Nov. 2015<http://www.encyclopedia.com>.

[48] Park, Y., "Drop Foot and Treatments." http://www.mccc.edu/~behrensb/documents/DropFootTreatmentsYPark.pdf

[49] Creylman, V., Muraru, L., Pallari, J., Vertommen, H., and Peeraer, L., 2013, "Gait assessment during the initial fitting of customized selective laser sintering ankle foot orthoses in subjects with drop foot," Prosthetics and Orthotics International, 37(2), pp. 132-138.

[50] O. Blog, “The Evolution of the AFO | Central Brace & Limb,” Central Brace & Limb, 04-Oct-2011. [Online]. Available at: http://centralbraceandlimb.com/evolution-afo/. [Accessed: 29-Jan-2016]

[51] Brakoulias, V., "History of Orthopadics," httl://www.pioa.net/documents/Historyoforthopaedics.pdf.

[52] International Committee of the Red Cross, n.d., “Manufacturing Guidelines Ankle-Foot Orthosis” from https://www.icrc.org/eng/assets/files/other/eng-afo-2010.pdf

[53] The Royal Children’s Hospital Melbourne, n.d., “Ankle-Foot Orthoses AFOs” from http://www.rch.org.au/orthotic/info_for_parents/AnkleFoot_Orthoses_AFOs/

[54] Department of Education, Rehabilitation Services Administration, St. Petersburg College, n.d “Ankle Foot Orthosis (AFO) Process Guide” from http://oandp.health.usf.edu/Pt/afo_process/AFO%20Brochure.pdf

[55] Mavroidis, C., Ranky, R. G., Sivak, M. L., Patritti, B. L., DiPisa, J., Caddle, A., Gilhooly, K., Govoni, L., Sivak, S., Lancia, M., Drillio, R., and Bonato, P., 2011, "Patient specific ankle-foot orthoses using rapid prototyping," Journal of NeuroEngineering and Rehabilitation, 8(1), pp. 1-11. https://jneuroengrehab.biomedcentral.com/articles/10.1186/1743-0003-8-1

[56] 3D Systems, 2016, "iSense 3D Scanner." http://www.3dsystems.com/

[57] Young, W. C., Budynas, R. G., and Sadegh, A. M., 2012, Roark's Formulas for Stress and Strain, The McGraw-Hill Companies, Inc.

[58] ANSYS, 2013, "ANSYS Mechanical User's Guide," ANSYS. http://148.204.81.206/Ansys/150/ANSYS%20Mechanical%20Users%20Guide.pdf

[59] Danielgm, "CloudCompare." http://www.danielgm.net/cc/

[60] Bossuyt, S., 2013, "Optimized Patterns for Digital Image Correlation,"Proceedings of the 2012 Annual Conference on Experimental and Applied Mechanics.

[61] 2013, "DIC - Digital Image Correlation,"
http://www.dantecdynamics.com/digital-image-correlation.

[62] "ARAMIS - Optical 3D Deformation Analysis,"
http://www.gom.com/metrology-systems/digital-image-correlation.html.

Appendix A: Technical Specifications of Commercially Available Scanners

Table 12. Scanner Comparisons.

Scanner	Resolution	Accuracy	Portability (Weight)	Cost	Field of View
Sense	0.9 mm	1 mm	N/A	$399.00	200 x 200 mm
iSense	0.9 mm	1 mm	0.992 kg	$499.00	200 x 200 mm
Matter and Form MFS1V1	0.43mm	0.25mm	1.71kg (3.77 lbs)	$550.00	34.5 cm x 21 cm x 8.5cm
Digitizer	0.5 mm	2mm	2.1 kg	$800.00	20.3 x 20.3 cm
IIIDScan	N/A	0.5 mm	N/A	$1,441.49	0.5 - 3 m
Next Engine	0.127 mm	0.127 mm	N/A	$2,995.00	N/A
David SLS-2	0.060 mm	0.1 mm	N/A	$3,149.00	10 - 600 mm
Thor 3D	2 mm	0.2 mm	1.8 kg	$14,000.00	0.7 x 0.9 m
Artec EVA	0.5 mm	0.1 mm	0.85 kg	$19,800.00	214 x 148 mm536 x 371 mm
Fast Scan	0.1 mm	0.13 mm	N/A	$19,995.00	up to 75 cm
Artec Spider	0.1 mm	0.05 mm	0.85 kg	$22,600.00	90 x 70 mm180 x 140 mm
Creaform Handyscan 300	0.1 mm	0.040 mm	0.85 kg	$42,900.00	225 x 250 mm
Creaform Handyscan 700	0.050 mm	0.030 mm	0.85 kg	$56,900.00	275 x 250 mm
Geomagic Capture Mini	0.080 - 0.100 mm	0.034 mm	1.04 kg	N/A	87 x 68 mm
Geomagic Capture	0.110 - 0.180 mm	0.060 mm	1.35 kg	N/A	124 x 120 mm
Faro 3D Freestyle3D	0.2 mm	<1.5 mm	0.98 kg	N/A	450 X 530 mm

Additional Information
http://www.cubify.com
http://cubify.com/products/isensetechspecs
https://matterandform.net/scanner
http://store.makerbot.com/digitizer
http://www.4ddynamics.com/3D-scanners/iiidscan/
http://www.nextengine.com/products/scanner/features/accurate
http://www.david-3d.com/en/products/sls-2
http://www.thor3dscanner.com
http://www.artec3d.com/hardware/artec-eva/
http://polhemus.com/_assets/img/FastSCAN_COBRA_C1.pdf
http://www.artec3d.com/hardware/artec-spider/how_it_works/
http://www.creaform3d.com/en/ndt-solutions/handyscan-3d-laser-scanners/
http://www.creaform3d.com/en/ndt-solutions/handyscan-3d-laser-scanners/
http://www.geomagic.com/en/products/capture/overview
http://www.geomagic.com/en/products/capture/overview
http://www.faro.com/products/3d-documentation/handheld-3d-scanner-freestyle-3d/

Appendix B: FEM Convergence Results for Static Structural Analysis of Simple, Standard, and Custom AFOs

The goal of a convergence test is to determine the least amount of elements which yields an accurate result from the simulation. This is done by evaluating the least number of elements necessary for the overall result to have an accuracy of 95%. Fewer elements used reduce the amount of process power needed to run the simulation.

Table 13. FEM Convergence of Simplified AFO Model.

Min Size, m	Number of Elements	Total Deformation, m	Von Mises Strain	Von Mises Stress, MPa
5.00E-03	609	3.26E-02	1.81E-03	4.25
2.70E-03	3809	3.27E-02	1.78E-03	4.18
2.50E-03	4438	3.27E-02	1.78E-03	4.18
2.00E-03	7812	3.27E-02	1.78E-03	4.178
1.50E-03	13710	3.27E-02	1.99E-03	4.665
1.00E-03	57785	3.27E-02	2.49E-03	5.84
9.00E-04	72969	3.27E-02	2.60E-03	6.10

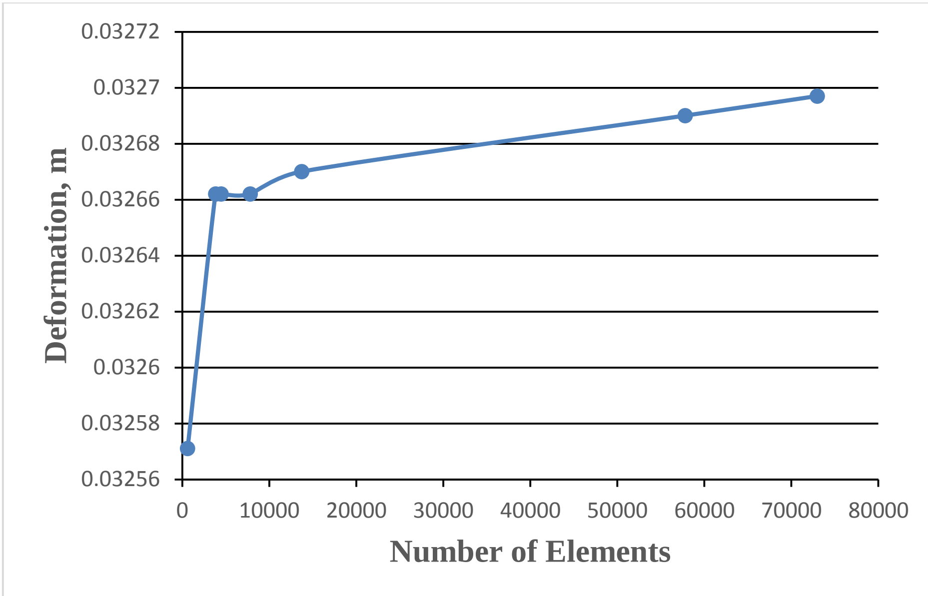

Figure 58. FEM Convergence of Simplified AFO for Total Deformations.

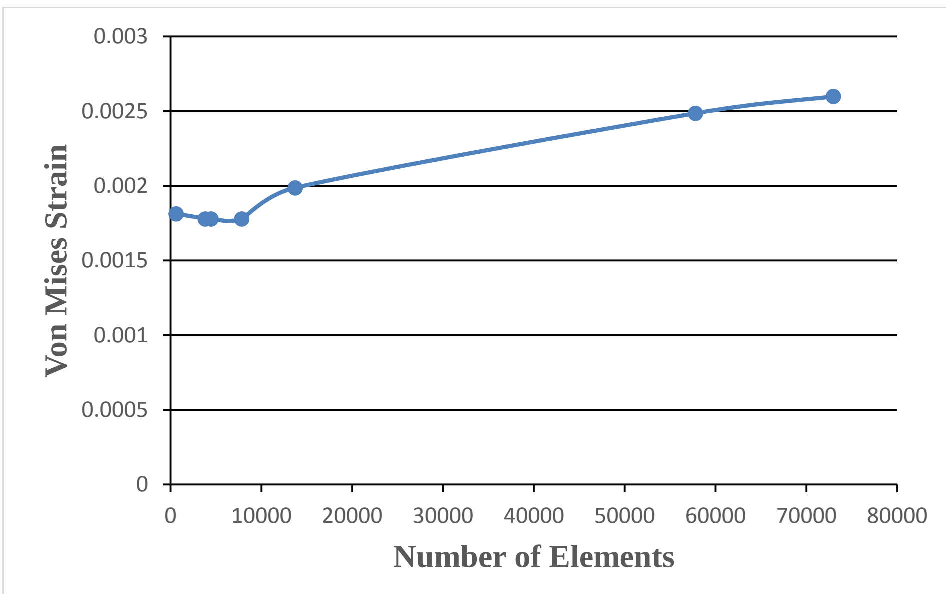

Figure 59. FEM Convergence of Simplified AFO von Mises Strain.

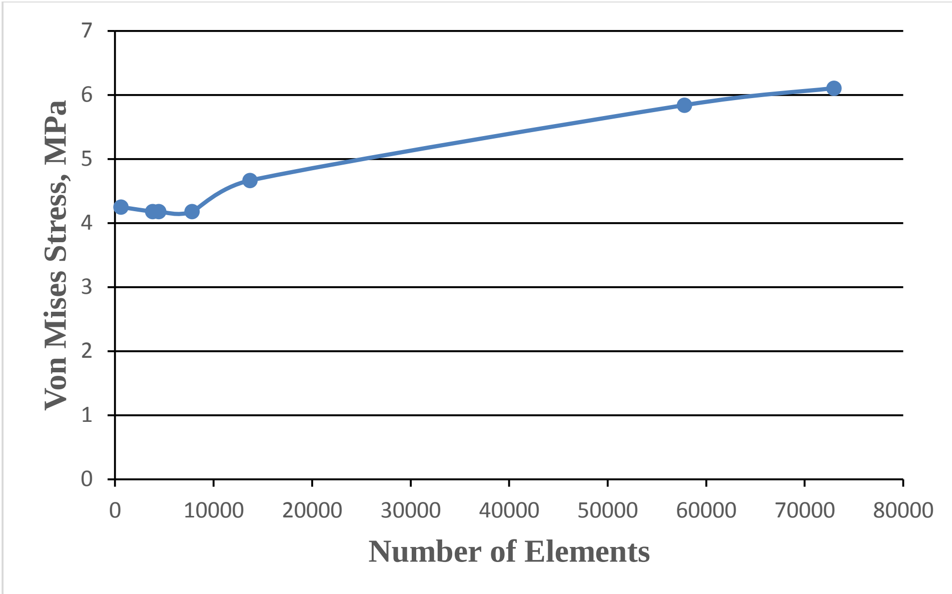

Figure 60. FEM Convergence of Simplified AFO von Mises Stress.

Table 14. FEM Convergence of Standard AFO Model.

Min size, m	Number of Elements	Total Deformation, m	Von Mises Strain	Von Mises Stress, MPa
0.01	693	0.00402	0.0008618	2.0175
0.0075	1344	0.00405	0.0008876	2.081
0.006667	1728	0.0041	0.0008802	2.0658
0.005	3622	0.00411	0.00090718	2.128
0.004	7872	0.00413	0.00093269	2.1888
0.003	16675	0.00413	0.000939	2.2041
0.0025	28706	0.00413	0.00095889	2.25
0.002	55204	0.00413	0.00095945	2.2526
0.0016	106621	0.00413	0.00096002	2.254

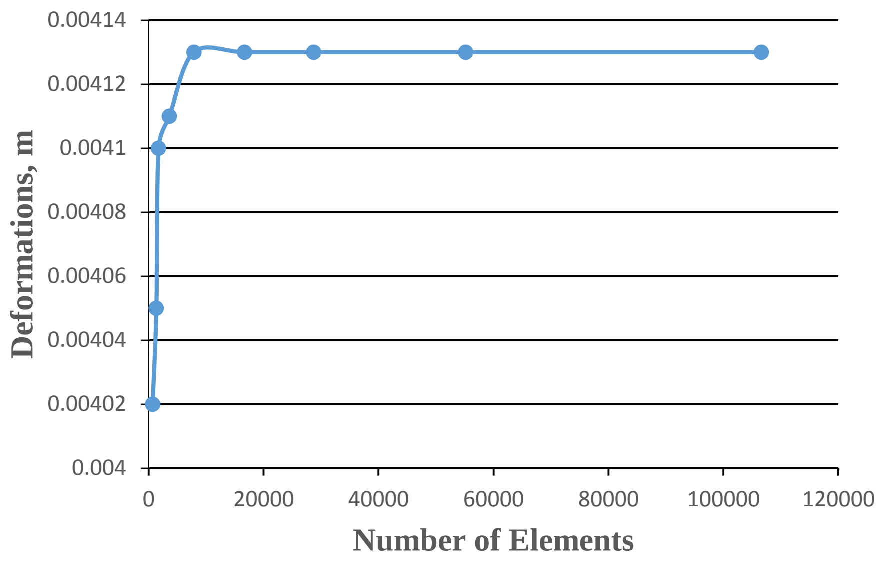

Figure 61. FEM Convergence of Standard AFO Total Deformations.

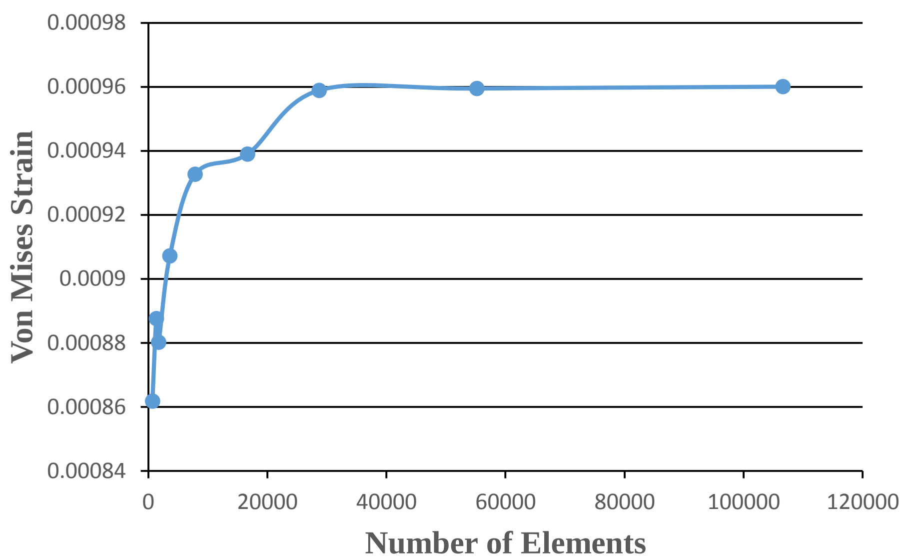

Figure 62. FEM Convergence of Standard AFO von Mises Strain.

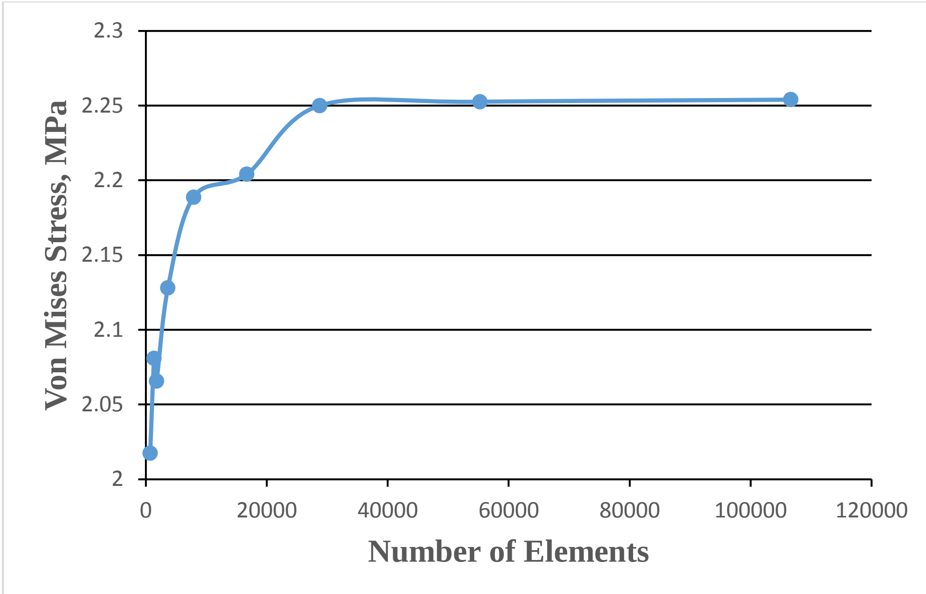

Figure 63. FEM Convergence of Standard AFO von Mises Stress.

Table 15. FEM Convergence of Custom AFO Model.

Number of Elements	Total Deformation, mm	Von Mises Strain	Von Mises Stress, MPa
10747	3.0247	0.000969	1.6282
11133	3.0736	0.001002	1.68941
14637	3.2035	0.001048	1.7585
23364	3.2541	0.001004	1.8213
33750	3.259	0.001081	1.8383
41764	3.2618	0.001140	1.84857
49355	3.2653	0.001155	1.95815
58562	3.2692	0.001169	1.9236
70737	3.2721	0.001336	2.26925
78898	3.2728	0.001368	2.28926
93550	3.2756	0.001405	2.3139
113040	3.2784	0.001536	2.6051

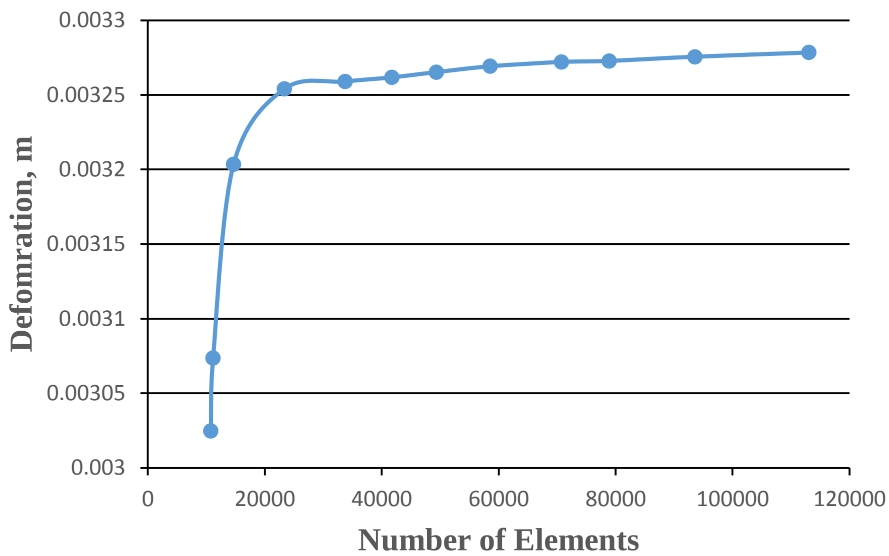

Figure 64. FEM Convergence of Custom AFO Total Deformations.

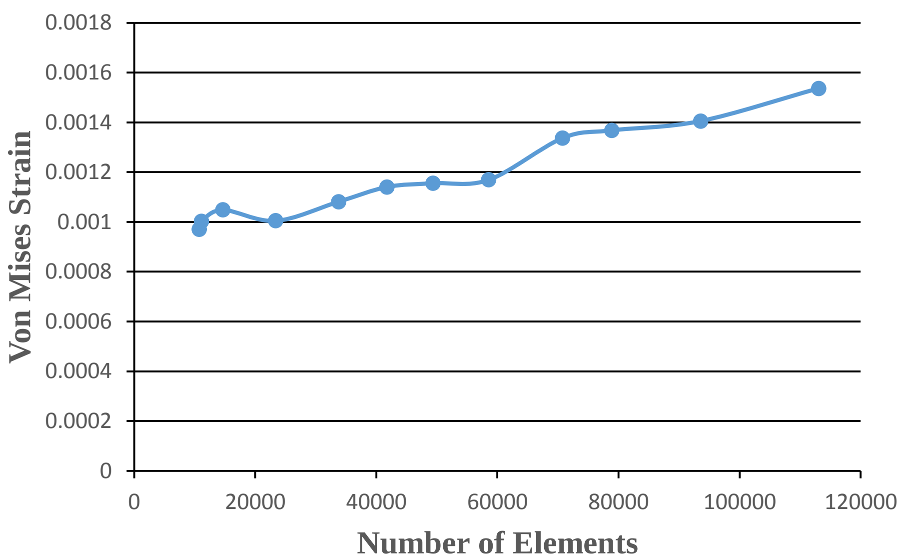

Figure 65. FEM Convergence of Custom AFO von Mises Strain.

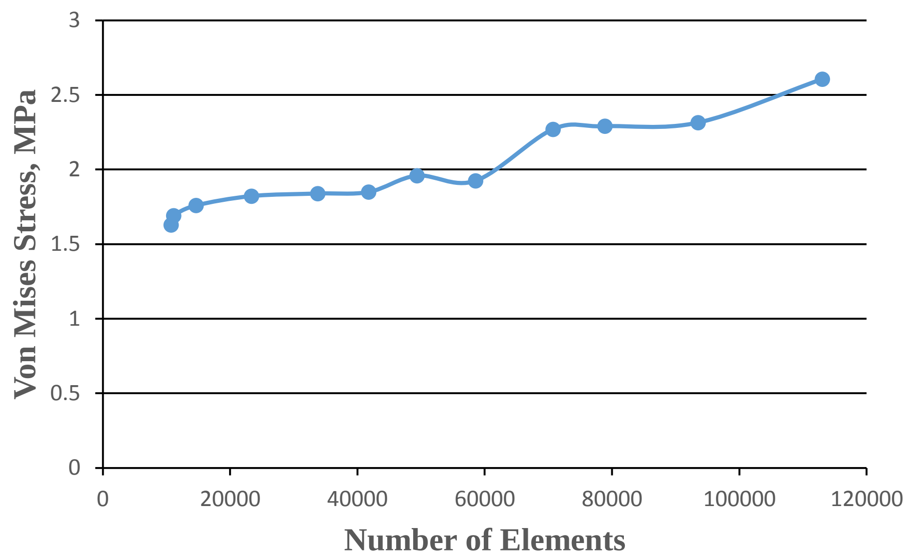

Figure 66. FEM Convergence of Custom AFO von Mises Stress.

Appendix C: Analytical Model of Simple AFO. Static Analysis and an Estimation of RSS Uncertainty

Physical Properties (all lengths are approximate):

$a := 6.05mm \qquad L_1 := 140mm$

$b := 70mm \qquad L_2 := 254mm - 32mm$

$R := 40mm \qquad L_3 := 40mm$

$A := b \cdot a \qquad F := 10N$

$$I := \frac{b \cdot a^3}{12}$$

Material Properties:

$G := 855MPa \qquad E := 2.348 \cdot GPa$

FEM Results:

$ANSYSstress := 4.18MPa$

$ANSYSstrain := 0.00178$

$ANSYSdeformation := 32.56mm$

Stress Calculations:

Foot Plate Calculations:

$x_{footplate} := 0, 0.001L_1 .. L_1$

$$\sigma_{footplate}(x) := \frac{(x \cdot F)\left(\frac{a}{2}\right)}{I} \qquad \tau_{footplate}(x) := \frac{F \cdot 3}{2 \cdot A}$$

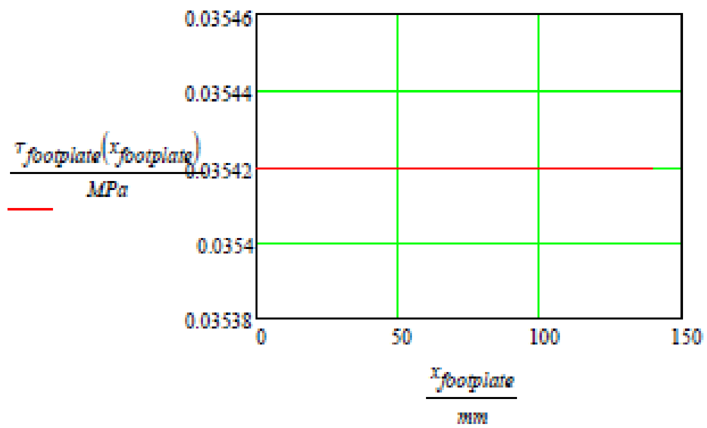

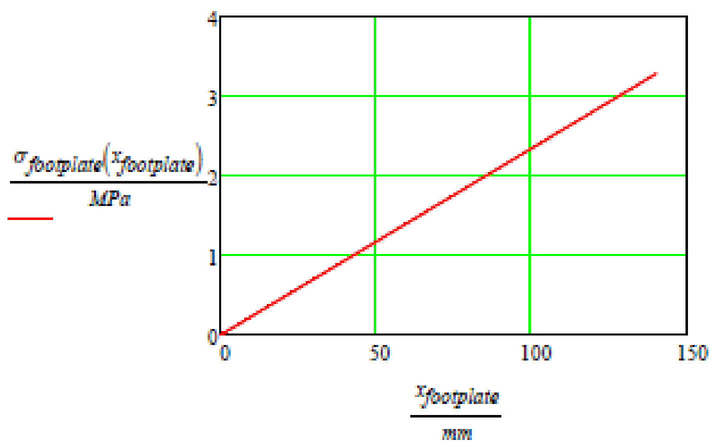

Back Plate Calculations:

$x_{backplate} := 0, 0.001L_2 .. L_2$

$\tau_{backplate}(x) := 0$

$$\sigma_{backplate}(x) := \frac{(L_1 + L_3) \cdot F\left(\frac{a}{2}\right)}{I} + \frac{F}{A}$$

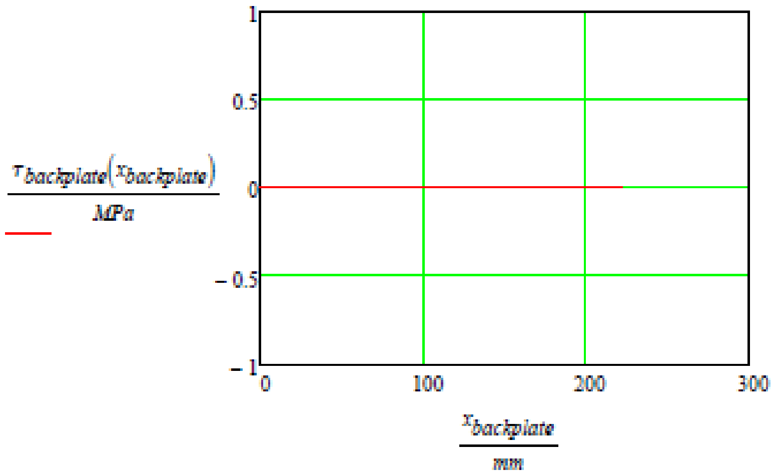

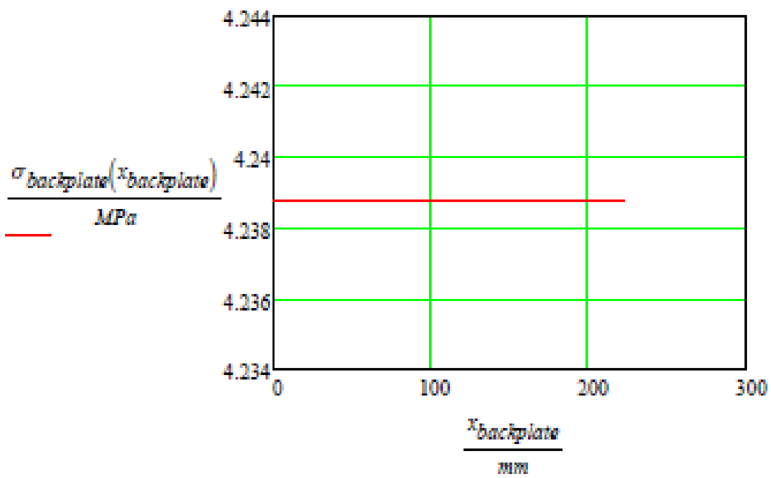

Curved Heel Section:

$x_{heel} := 0, 0.01L_3 .. L_3$

$e := \dfrac{I}{\left(R + \dfrac{a}{2}\right) \cdot A} = 0.003 \cdot in$ $\dfrac{R}{a} = 6.612$

$r := R = 40 \cdot mm$

$\sigma_{heel}(x) := \dfrac{\left[\left(F \cdot L_1\right) + (F \cdot x)\right] \cdot \left(\dfrac{a}{2}\right)}{A \cdot e \cdot r}$

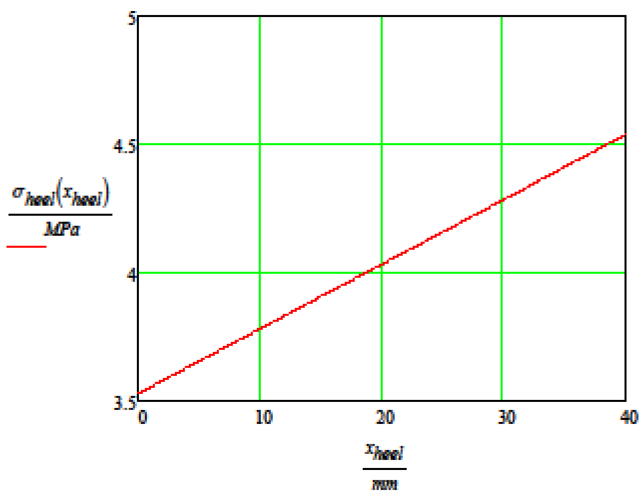

$\dfrac{R}{b} = 0.571$ Peak Shear = 2.04V/A

$\tau_{heel} := \dfrac{2.04F}{A} = 0.048 \cdot MPa$

Strain Calculations: Assuming linear elastic

Calculations of Principle Stresses:

$$\sigma_{1.backplate}(x) := \frac{\sigma_{backplate}(x)}{2} + \sqrt{\left(\frac{\sigma_{backplate}(x)}{2}\right)^2 + \tau_{backplate}(x)^2}$$

$$\sigma_{2.backplate}(x) := \frac{\sigma_{backplate}(x)}{2} - \sqrt{\left(\frac{\sigma_{backplate}(x)}{2}\right)^2 + \tau_{backplate}(x)^2}$$

$$\sigma_{1.footplate}(x) := \frac{\sigma_{footplate}(x)}{2} + \sqrt{\left(\frac{\sigma_{footplate}(x)}{2}\right)^2 + \tau_{footplate}(x)^2}$$

$$\sigma_{2.footplate}(x) := \frac{\sigma_{footplate}(x)}{2} - \sqrt{\left(\frac{\sigma_{footplate}(x)}{2}\right)^2 + \tau_{footplate}(x)^2}$$

$$\sigma_{1.heel}(x) := \frac{\sigma_{heel}(x)}{2} + \sqrt{\left(\frac{\sigma_{heel}(x)}{2}\right)^2 + \tau_{heel}^2}$$

$$\sigma_{2.heel}(x) := \frac{\sigma_{heel}(x)}{2} - \sqrt{\left(\frac{\sigma_{heel}(x)}{2}\right)^2 + \tau_{heel}^2}$$

$$\varepsilon(\sigma_1, \sigma_2) := \frac{\left(\sqrt{\sigma_1^2 + \sigma_1 \cdot \sigma_2 + \sigma_2^2}\right)}{E}$$

$\varepsilon\left(\sigma_{1.backplate}\left(x_{backplate}\right),\sigma_{2.backplate}\left(x_{backplate}\right)\right)$

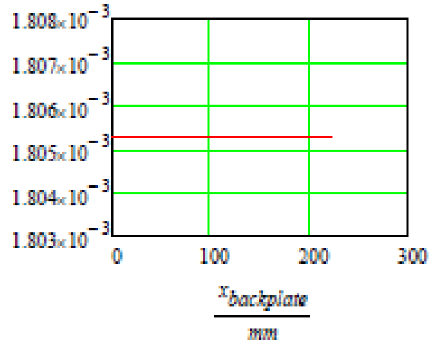

$\varepsilon\left(\sigma_{1.footplate}\left(x_{footplate}\right),\sigma_{2.footplate}\left(x_{footplate}\right)\right)$

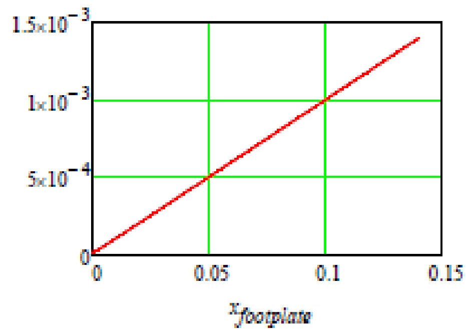

$\varepsilon\left(\sigma_{1.heel}\left(x_{heel}\right),\sigma_{2.heel}\left(x_{heel}\right)\right)$

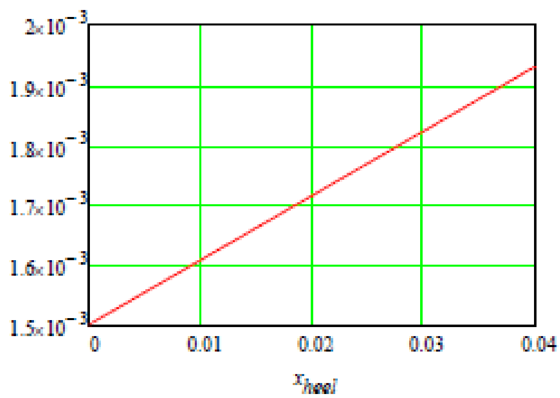

Deformation Calculations:

Derivation of Castigliano's Theorem

Vx is the shear at that angular position.

Nx is the normal force at that angular position

Mx is the moment at that angular position.

$V := F = 10N$

$R_n := R + \frac{a}{2} \qquad n := 0MPa$

$M_0 := F \cdot L_1 = 1.4 \cdot N \cdot m$

$M_x(x) := V \cdot R_n \cdot sin(x) + n \cdot R_n \cdot (1 - cos(x)) + M_0$

$V_x(x) := V \cdot cos(x) + n \cdot sin(x)$

$N_x(x) := -n \cdot cos(x) + V \cdot sin(x)$

$$U = \int \frac{M_x(x)^2}{2 \cdot A \cdot E \cdot e} dx + \int \frac{F \cdot V_x(x)^2 \cdot R_n}{2 \cdot A \cdot G} dx + \int \frac{N_x{}^2 \cdot R_n}{2 \cdot A \cdot E} dx - \int \frac{M_x \cdot N_x}{A \cdot E} dx$$

$$U = \int \frac{\left[V \cdot R_n \cdot sin(x) + n \cdot R_n \cdot (1 - cos(x)) + M_0\right]^2}{2 \cdot A \cdot E \cdot e} dx + \int \frac{F \cdot (V \cdot cos(x) + n \cdot sin(x))^2 \cdot R_n}{2 \cdot A \cdot G} dx \;...$$
$$+ \int \frac{(-n \cdot cos(x) + V \cdot sin(x))^2 \cdot R_n}{2 \cdot A \cdot E} dx \;...$$
$$+ -\left[\int \frac{\left[V \cdot R_n \cdot sin(x) + n \cdot R_n \cdot (1 - cos(x)) + M_0\right] \cdot (-n \cdot cos(x) + V \cdot sin(x))}{A \cdot E} dx\right]$$

$$U = \int \frac{\left(V \cdot R_n \cdot sin(x) + M_0\right)^2}{2 \cdot A \cdot E \cdot e} dx + \int \frac{F \cdot (V \cdot cos(x))^2 \cdot R_n}{2 \cdot A \cdot G} dx \ldots$$

Since n is zero in this case

$$+ \int \frac{(V \cdot sin(x))^2 \cdot R_n}{2 \cdot A \cdot E} dx - \int \frac{\left(V \cdot R_n \cdot sin(x) + M_0\right) \cdot (V \, sin(x))}{A \cdot E} dx$$

$$U = \int \frac{V^2 \cdot \left(R_n \cdot sin(x)\right)^2 + M_0 \cdot V \cdot R_n \cdot sin(x) + M_0^{\,2}}{2 \cdot A \cdot E \cdot e} dx + \int \frac{F \cdot (V \cdot cos(x))^2 \cdot R_n}{2 \cdot A \cdot G} dx \ldots$$

$$+ \int \frac{(V \cdot sin(x))^2 \cdot R_n}{2 \cdot A \cdot E} dx - \int \frac{V^2 \cdot R_n \cdot sin(x)^2 + M_0 \cdot V \cdot sin(x)}{A \cdot E} dx$$

$$\delta_y = \frac{\partial}{\partial V} U \qquad \delta_x = \frac{\partial}{\partial n} U \qquad \theta = \frac{\partial}{\partial M_0} U$$

$f := \frac{6}{5}$ Factor for a rectagular cross section

$$\delta_y(x) := \int_0^x \frac{2V\left(R_n \cdot sin(x)\right)^2 + M_0 \cdot R_n \cdot sin(x)}{2 \cdot A \cdot E \cdot e} dx + \int_0^x \frac{2 \cdot V f \cdot cos(x)^2 \cdot R_n}{2 \cdot A \cdot G} dx \ldots$$

$$+ \int_0^x \frac{2 \cdot V \, sin(x)^2 \cdot R_n}{2 \cdot A \cdot E} dx - \int_0^x \frac{2V \cdot R_n \cdot sin(x) \cdot sin(x) + M_0 \cdot sin(x)}{A \cdot E} dx$$

Uses Degrees

$x_{dis} := 0, 0.001deg .. 90deg$

$$deformation := \int_0^{L_1} \frac{2\cdot F\cdot L_1^{\,2} - 2\cdot F\cdot L_1\cdot x + 2\cdot F\cdot x^2}{2\cdot E\cdot I}\,dx + \int_0^{L_2} \frac{2\cdot F\cdot \left(L_1 + L_3\right)^2}{2\cdot E\cdot I}\,dx + \int_0^{L_2} \frac{2\cdot F}{2\cdot E\cdot A}\,dx \ldots$$

$$+ \int_0^{90deg} \frac{2V\left(R_n\cdot sin(x)\right)^2 + M_0\cdot R_n\cdot sin(x)}{2\cdot A\cdot E\cdot e}\,dx + \int_0^{90deg} \frac{2\cdot V f\cdot cos(x)^2\cdot R_n}{2\cdot A\cdot G}\,dx \ldots$$

$$+ \int_0^{90deg} \frac{2\cdot V sin(x)^2\cdot R_n}{2\cdot A\cdot E}\,dx - \int_0^{90deg} \frac{2V\cdot R_n\cdot sin(x)\cdot sin(x) + M_0\cdot sin(x)}{A\cdot E}\,dx$$

Percent Difference Calculations:

As the calculations for stress in the curved beam is highly sensitive to dimensions, the backplate stress and strain were used to compare to the FEM results for a better aproximation of difference in the two models.

$$\frac{\left|\sqrt{\sigma_{1.backplate}(0)^2 + \sigma_{1.backplate}(0)\cdot\sigma_{2.backplate}(0) + \sigma_{2.backplate}(0)^2} - ANSYSstress\right|}{\sigma_{backplate}(0m)}\cdot 100 = 1.387$$

$$\frac{\left|\varepsilon\left(\sigma_{1.backplate}(0),\sigma_{2.backplate}(0)\right) - ANSYSstrain\right|}{\varepsilon\left(\sigma_{1.backplate}(0),\sigma_{2.backplate}(0)\right)}\cdot 100 = 1.4$$

$$\frac{\left|deformation - ANSYSdeformation\right|}{deformation}\cdot 100 = 2.105$$

RSS Uncertanity:

$$def\left(L_{1v},L_{2v},L_{3v},a_v,b_v,R_v\right) := \int_0^{L_{1v}} \frac{2\cdot F\cdot L_{1v}^{\;2} - 2\cdot F\cdot L_{1v}\cdot x + 2\cdot F\cdot x^2}{2\cdot E\cdot \frac{b_v\cdot a_v^{\;3}}{12}}\,dx\;...$$

$$+\int_0^{L_{2v}} \frac{2\cdot F\cdot\left(L_{1v}+L_{3v}\right)^2}{2\cdot E\cdot\frac{b_v\cdot a_v^{\;3}}{12}}\,dx\;...$$

$$+\int_0^{L_{2v}} \frac{2\cdot F}{2\cdot E\cdot\left(a_v\cdot b_v\right)}\,dx\;...$$

$$+\left[\begin{array}{l}\displaystyle\int_0^{90deg} \frac{2F\left[\left(R_v+\frac{a_v}{2}\right)\cdot sin(x)\right]^2 + \left(F\cdot L_{1v}\right)\cdot\left(R_v+\frac{a_v}{2}\right)\cdot sin(x)}{2\cdot\left(a_v\cdot b_v\right)\cdot E\cdot\frac{\left(\frac{b_v\cdot a_v^{\;3}}{12}\right)}{R_v\cdot\left(a_v\cdot b_v\right)}}\,dx\;... \\ \displaystyle+\int_0^{90deg} \frac{2\cdot F\,f\cdot cos(x)^2\cdot\left(R_v+\frac{a_v}{2}\right)}{2\cdot\left(a_v\cdot b_v\right)\cdot G}\,dx\;... \\ \displaystyle+\int_0^{90deg} \frac{2\cdot F\,sin(x)^2\cdot\left(R_v+\frac{a_v}{2}\right)}{2\cdot\left(a_v\cdot b_v\right)\cdot E}\,dx\;... \\ \displaystyle+-\int_0^{90deg} \frac{2F\cdot\left(R_v+\frac{a_v}{2}\right)\cdot sin(x)\cdot sin(x) + \left(F\cdot L_{1v}\right)\cdot sin(x)}{\left(a_v\cdot b_v\right)\cdot E}\,dx\end{array}\right]$$

$$\delta d = \left[\left[\frac{\partial}{\partial L_1}(d\cdot\delta L_1)\right]^2 + \left[\frac{\partial}{\partial L_2}(d\cdot\delta L_2)\right]^2 + \left[\frac{\partial}{\partial L_3}(d\cdot\delta L_3)\right]^2 + \left[\frac{\partial}{\partial R}(d\cdot\delta R)\right]^2 + \left[\frac{\partial}{\partial a}(d\cdot\delta a)\right]^2 \ldots + \left[\frac{\partial}{\partial b}(d\cdot\delta b)\right]^2\right]^{\frac{1}{2}}$$

Variables and their respective uncertainties:

$L_3 = 40\cdot mm$ $\quad \delta L_3 := 2mm$ $\qquad R = 40\cdot mm$ $\quad \delta R := 2mm$

$L_1 = 140\cdot mm$ $\quad \delta L_1 := 2mm$ $\qquad b = 70\cdot mm$ $\quad \delta b := 3.5mm$

$L_2 = 222\cdot mm$ $\quad \delta L_2 := 1mm$ $\qquad a = 6.05\cdot mm$ $\quad \delta a := 2.5mm$

$$\delta def := \left[\left(\frac{\partial}{\partial L_1}def(L_1, L_2, L_3, a, b, R)\cdot\delta L_1\right)^2 \ldots + \left(\frac{\partial}{\partial L_2}def(L_1, L_2, L_3, a, b, R)\cdot\delta L_2\right)^2 \ldots + \left(\frac{\partial}{\partial L_3}def(L_1, L_2, L_3, a, b, R)\cdot\delta L_3\right)^2 \ldots + \left(\frac{\partial}{\partial a}def(L_1, L_2, L_3, a, b, R)\cdot\delta a\right)^2 \ldots + \left(\frac{\partial}{\partial b}def(L_1, L_2, L_3, a, b, R)\cdot\delta b\right)^2\right]^{\frac{1}{2}}$$

Percentage contributions to uncertanty.
Ranked in order of highest to lowest percent contribution.

$$\frac{\left(\frac{\partial}{\partial a}def(L_1,L_2,L_3,a,b,R)\cdot\delta a\right)^2}{\delta def^2}\cdot 100 = 99.772$$

$$\frac{\left(\frac{\partial}{\partial b}def(L_1,L_2,L_3,a,b,R)\cdot\delta b\right)^2}{\delta def^2}\cdot 100 = 0.163$$

$$\frac{\left(\frac{\partial}{\partial L_1}def(L_1,L_2,L_3,a,b,R)\cdot\delta L_1\right)^2}{\delta def^2}\cdot 100 = 0.047$$

$$\frac{\left(\frac{\partial}{\partial L_2}def(L_1,L_2,L_3,a,b,R)\cdot\delta L_2\right)^2}{\delta def^2}\cdot 100 = 0.001$$

$$\frac{\left(\frac{\partial}{\partial L_3}def(L_1,L_2,L_3,a,b,R)\cdot\delta L_3\right)^2}{\delta def^2}\cdot 100 = 0.018$$

$$\frac{\left(\frac{\partial}{\partial R}def(L_1,L_2,L_3,a,b,R)\cdot\delta R\right)^2}{\delta def^2}\cdot 100 = 0$$

The RSS uncertanty analysis indicates that the most sensitive variables are the thickness of the cantilevered beam, followed by the width of the beam, then the active lengths of each of the sections. This means that measuring the thickness of the test model is by far the most important aspect of the physical testing described in Section 3.5.1 in order to minimize the errors between the FEM results and the physical testing results casued by the experimental set up.

Appendix D: Geometric Validation at Different Surface Details Between iSense and ScanTo3D Scans

Additional research was done into the accuracy of different levels of surface detail for ScanTo3D seen in Figure 67. The next set of Figures, Figure 68, Figure 69, Figure 70, and Figure 71 show the distance map displaying the absolute distances, and histograms displaying distances in the X, Y, and Z directions respectively, for the low level surface detail option.

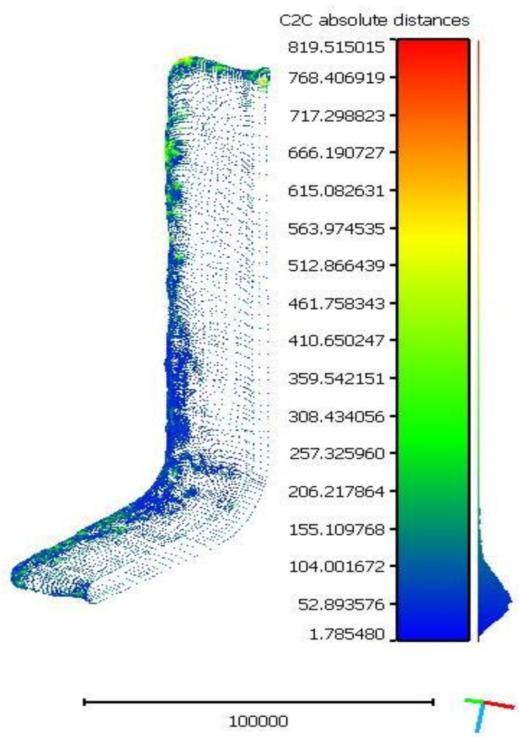

Figure 67. Absolute Distances Representing the Geometrical Differences Between iSense Data Cloud and ScanTo3D Model for Simplified AFO, μm. Distances Determined using a ScanTo3D Model Defined by Low Surface Detail.

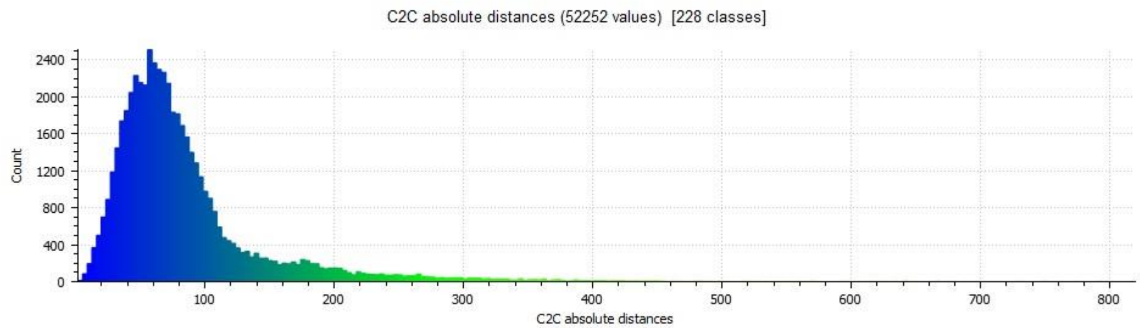

Figure 68. Histogram of Absolute Distances Obtained from Figure 66, μm.

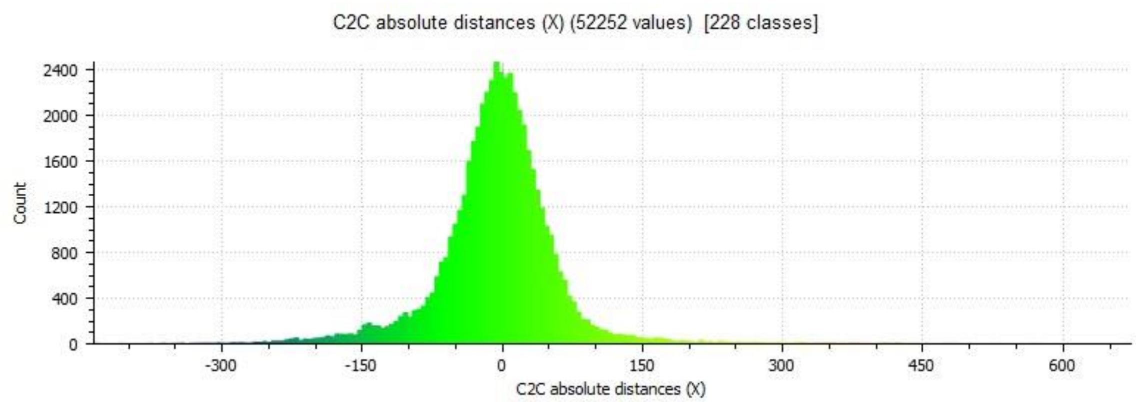

Figure 69. Histogram of X Distance for Low Surface Detail between iSense Data Cloud and ScanTo3D Model for Simplified AFO, μm.

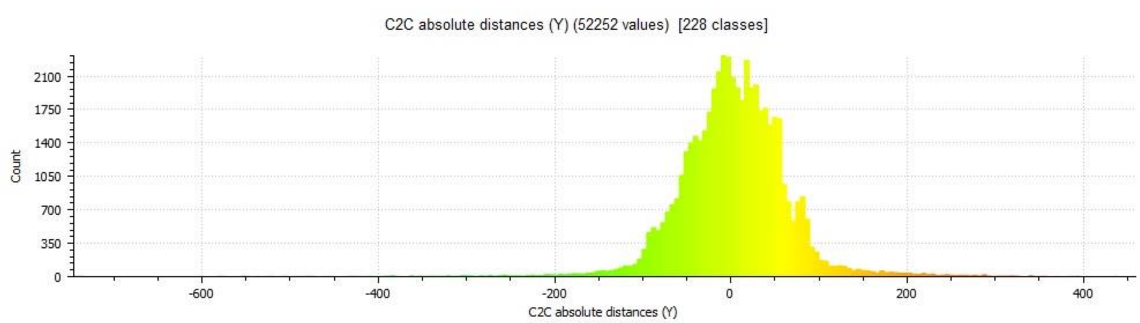

Figure 70. Histogram of Y Distance for Low Surface Detail between iSense Data Cloud and ScanTo3D Model for Simplified AFO, μm.

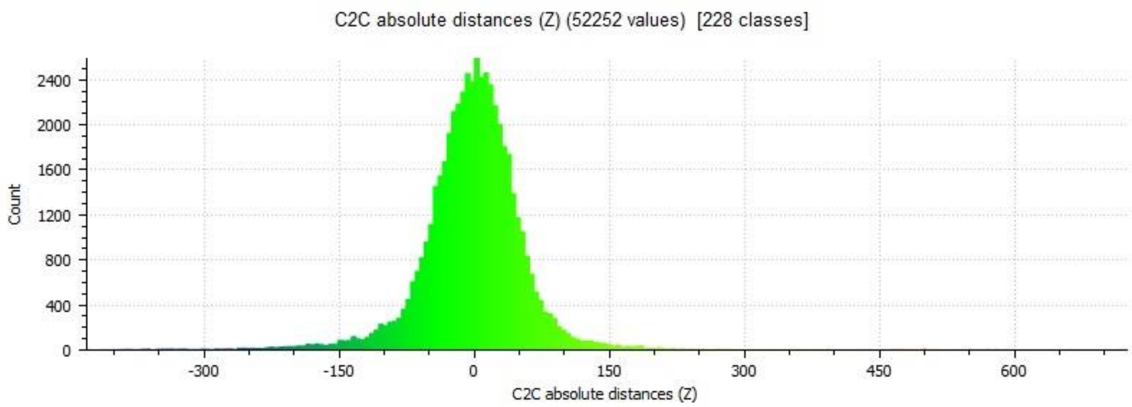

Figure 71. Histogram of Z Distance for Low Surface Detail between iSense Data Cloud and ScanTo3D Model for Simplified AFO, µm.

Table 16. Summary Statistics and Confidence Interval for Low Level Surface Detail.

Variable	Data
Mean	85 µm
Standard Deviation	64 µm
Z Score for 95% Confidence	192 µm
Upper Bound for Error	139 µm
Lower Bound for Error	31 µm

With 95% confidence it can be stated that the error caused by ScanTo3D, when using the low surface detail option, the error was between ± 139 µm to 31 µm, as exemplified in Table 16.

The following set of Figures displays the data gathered for the high surface detail option. Figure 72 displays the distance map of absolute distances. Figure 73, Figure 74, Figure 75, and Figure 76 display the histograms of the distances in the absolute distances, and the X, Y, and Z directions respectively.

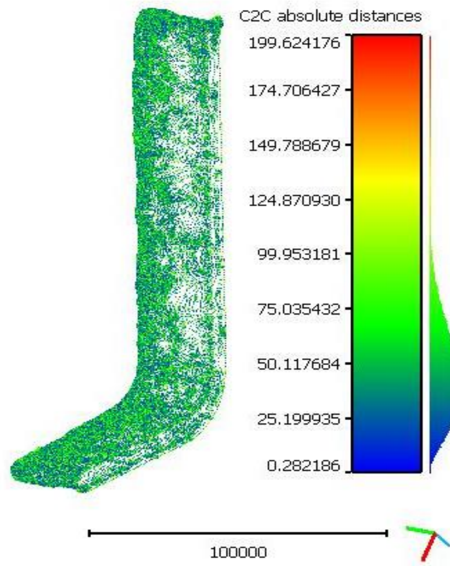

Figure 72. Absolute Distances Representing the Geometrical Differences Between iSense Data Cloud and ScanTo3D Model for Simplified AFO, µm. Distances Determined using a ScanTo3D Model Defined by High Surface Detail.

.

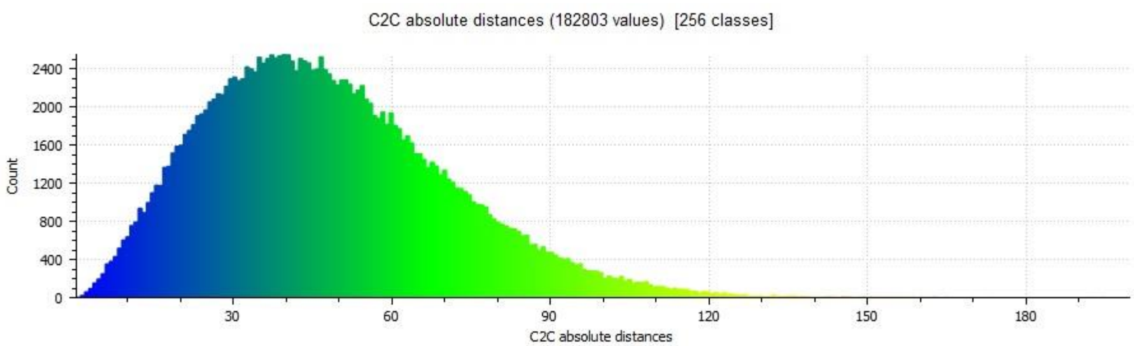

Figure 73. Histogram of Absolute Distances Obtained from Figure 71, µm.

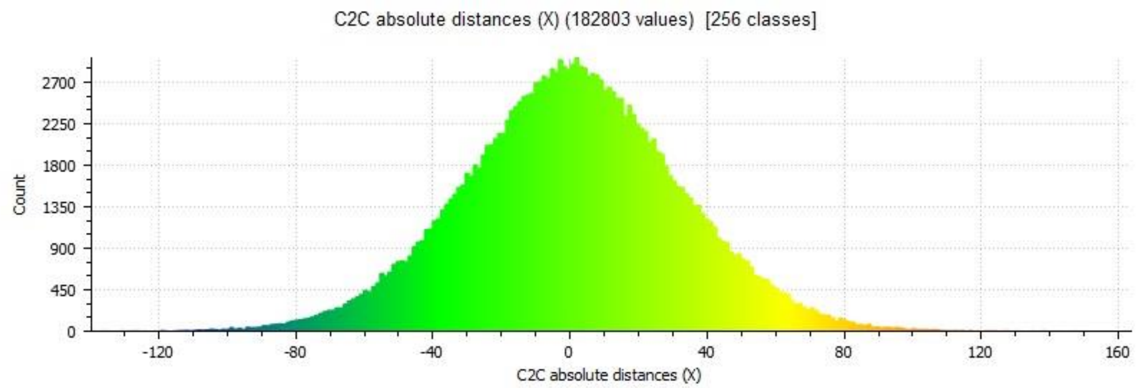

Figure 74. Histogram of X Distance for High Surface Detail between iSense Data Cloud and ScanTo3D Model for Simplified AFO, µm.

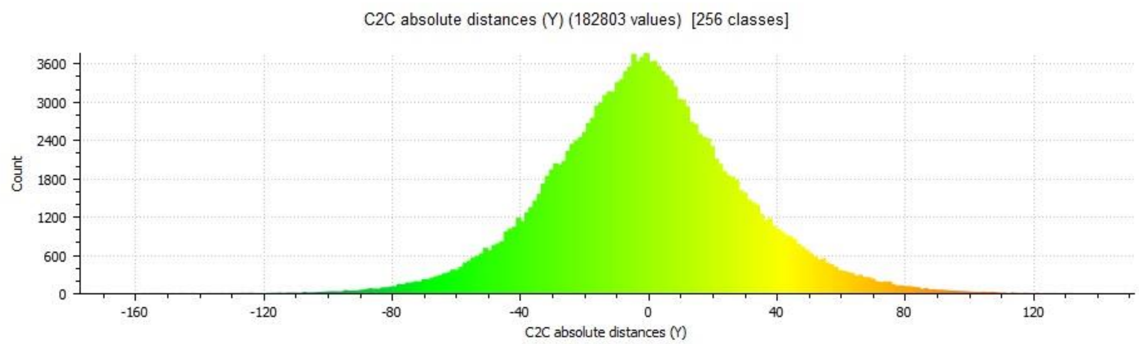

Figure 75. Histogram of Y Distance for High Surface Detail between iSense Data Cloud and ScanTo3D Model for Simplified AFO, µm.

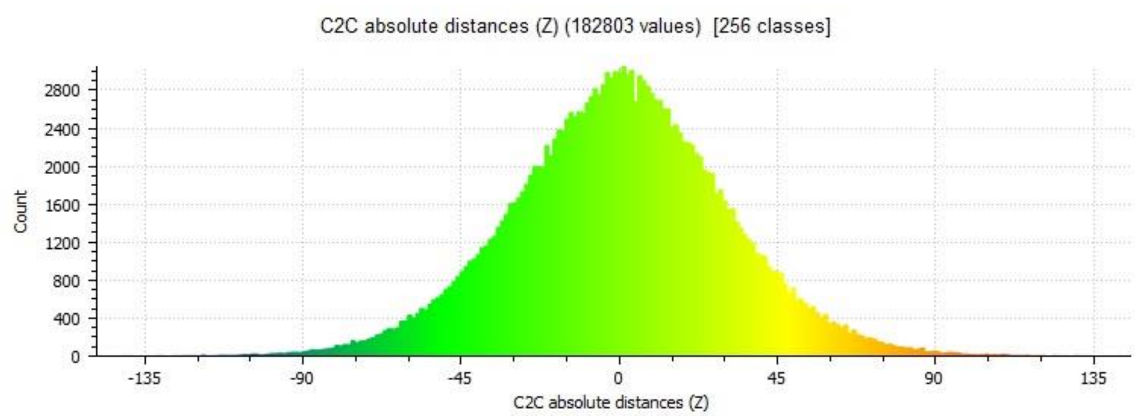

Figure 76. Histogram of Z Distance for High Surface Detail between iSense Data Cloud and ScanTo3D Model for Simplified AFO, µm.

Table 17. Summary Statistics and Confidence Interval for High Level Surface Detail.

Variable	Data
Mean	48 µm
Standard Deviation	23 µm
Z Score for 95% Confidence	85 µm
Upper Limit for Error	52 µm
Lower Limit for Error	43 µm

It can be stated from this data that the error caused by ScanTo3D when using the high level surface detail option was between ± 52 µm to ± 43 µm as seen in Table 17. Figure 77, Figure 78, and Figure 79 display the X, Y and Z histograms for the iSense validation.

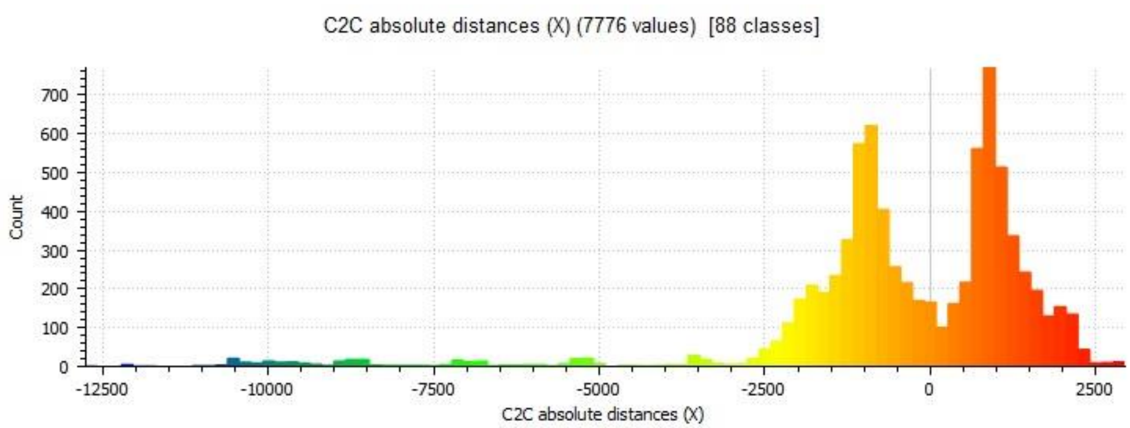

Figure 77. Histogram of X Distance between iSense Data Cloud and CAD Model of Simplified AFO, µm.

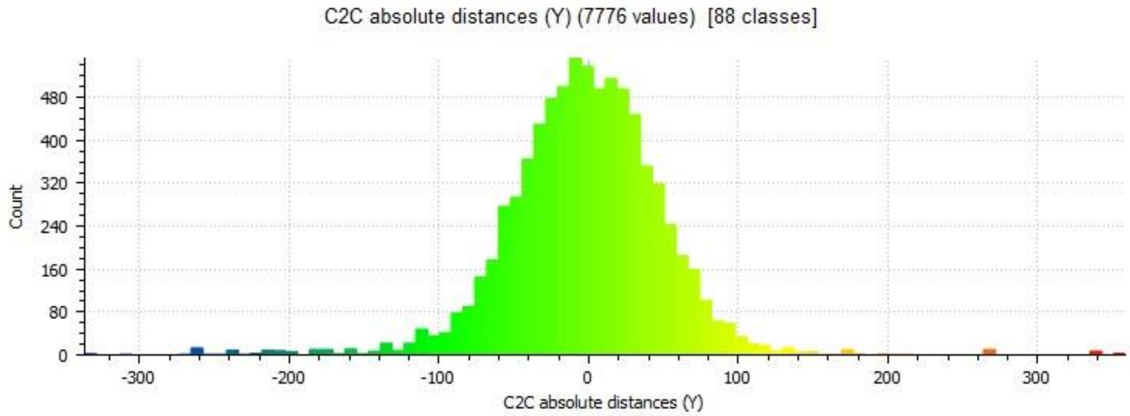

Figure 78. Histogram of Y Distance between iSense Data Cloud and CAD Model of Simplified AFO, µm.

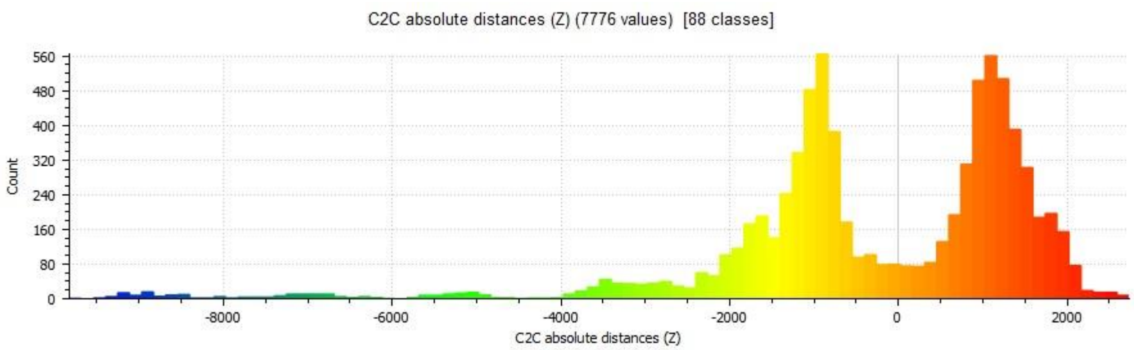

Figure 79. Histogram of Z Distance between iSense Data Cloud and CAD Model of Simplified AFO, µm.

Figure 80, Figure 81, and Figure 82 display the X, Y, and Z histograms for the NIST gauge.

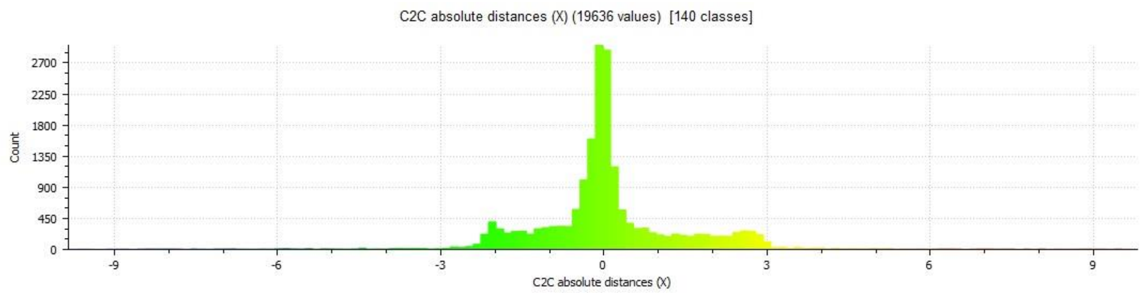

Figure 80. Histogram of X Distance between iSense Data Cloud and CAD Model of NIST Bowl, mm.

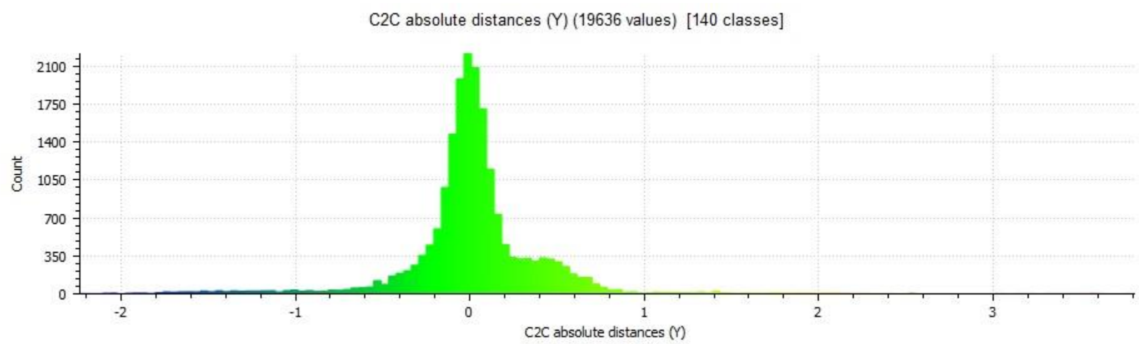

Figure 81. Histogram of Y Distance between iSense Data Cloud and CAD Model of NIST Bowl, mm.

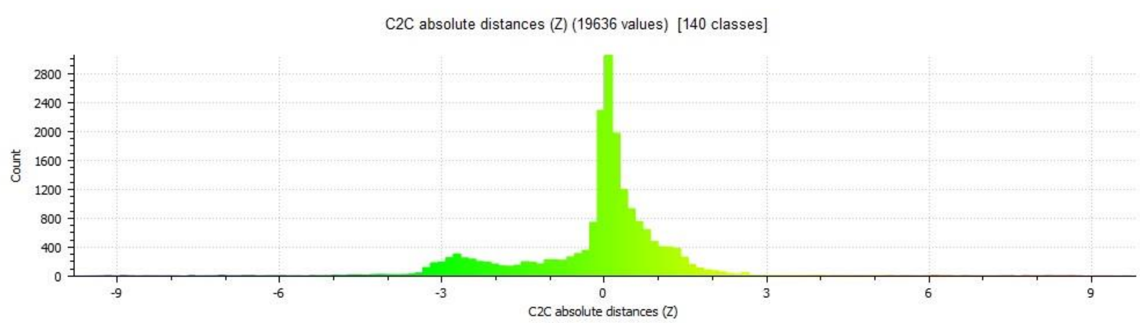

Figure 82. Histogram of Z Distance between iSense Data Cloud and CAD Model of NIST Bowl, mm.

Figure 83, Figure 84, and Figure 85 display the X, Y, and Z histograms for the Medium surface detail option.

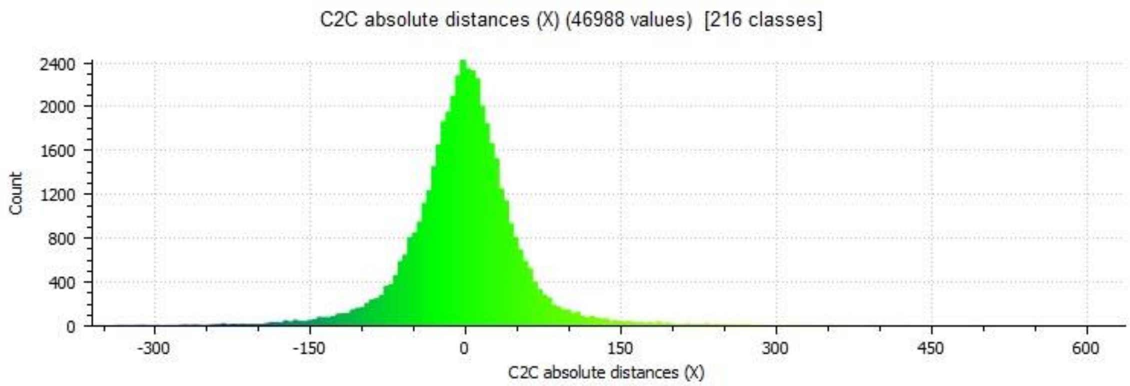

Figure 83. Histogram of X Distance for Medium Surface Detail between iSense Data Cloud and ScanTo3D Model for Simplified AFO, µm.

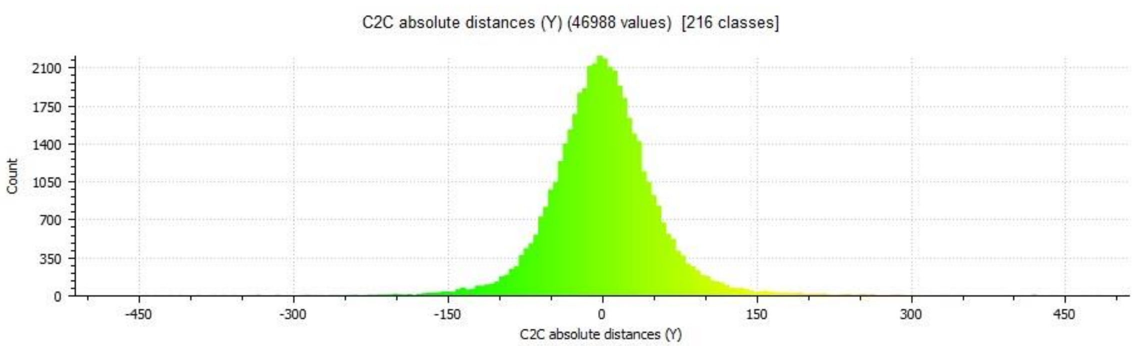

Figure 84. Histogram of Y Distance for Medium Surface Detail between iSense Data Cloud and ScanTo3D Model for Simplified AFO, µm.

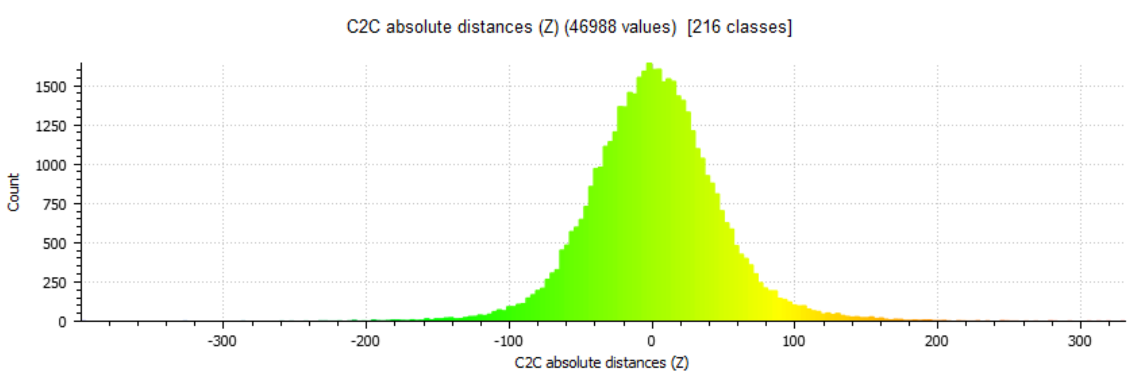

Figure 85. Histogram of Z Distance for Medium Surface Detail between iSense Data Cloud and ScanTo3D Model for Simplified AFO, µm.